Faculty 07- Mathematics and Computer Science, Physics, Geography

I. Physikalisches Institut

Justus-Liebig-Universität Gießen

Label-free detection of biomolecules using silicon nanowire ion-sensitive field-effect transistor devices

DISSERTATION

to apply for the degree of **"Doctor rerum naturalium"**

(Dr. rer. nat.)

Submitted by

Dipti Rani

born August 31, 1988

in Haryana, India

Gießen, September 2017

REPORTERS:

1. Prof. Dr. Martin Eickhoff, I. Physikalisches Institut, Justus-Liebig-Universität Gießen
2. Prof. Dr. Sven Ingebrandt, Biomedical signalling group, University of Applied Sciences Kaiserslautern, campus Zweibruecken

The following work was carried out betweeen January 2013 and July 2016 under Prof. Dr. Sven Ingebrandt at the Biomedical Signalling group of University of Applied Sciences Kaiserslautern, Campus Zweibruecken, Germany.

To my Ma, Pa and Bhai for their immense support, love and belief

Abstract

Regular monitoring of the overall health condition of patients is necessary nowadays, as over recent years there are new threats introduced such as changing environmental conditions, depleting food and energy resources, etc. leading to various deadly diseases. In particular it is important to develop point of care (POC) solutions with which it would be possible to detect diseases in early stages, without the need of regular visits to expensive clinics. Due to the advancement in nanotechnology, nanoelectronic sensors (e.g., field-effect transistor (FET) biosensors) are promising towards POC device development. The biomolecule detection with such devices is label-free and they can be used for quantitative, real-time diagnosis. Among FET biosensors, silicon nanowire FET (Si NW FET) devices are at cutting edge, because of their well-known and controllable properties, availability for mass production and good stability. After the first introduction of Si NW FET sensors in 2001, they have been reported for detection of various chemicals and biomolecules with high sensitivity and selectivity.

The aim of this thesis work was to develop a high-throughput wafer-scale fabrication for Si NW FETs and to deploy them for reliable chemical and biomolecule sensing applications. To achieve this goal, a fabrication process using a combination of nanoimprint lithography (NIL), photo lithography and wet chemical etching was developed. With this process the Si NW FET pattern consisting of micro- and nano-scale dimensions was processed on wafer-scale using a single NIL step as a relatively inexpensive and fast method. A total of 78 Si NW FET chips measuring 10 mm × 7 mm with 32 identical Si NW FETs in each, were patterned on *prime* quality 4” silicon on insulator wafers. It was possible to define and control the dimensions of the nanowires precisely, *via* designing the dimensions of the nanoimprint mould and by controlling the anisotropic wet etching time and etchant solution composition.

The fabricated chips were wire bonded on printed circuit board carriers and encapsulated for usage in ion-sensitive field-effect transistor (ISFET) configurations. The Si NW ISFETs were thoroughly characterized by different microscopy and electrical characterization methods in order to study the uniformity and reproducibility of our wafer-scale fabrication process.

The devices were also deployed for sensing of chemicals and biomolecules in ISFET configuration. Firstly, proof-of-principle experiments such as pH sensing were carried out. The sensors showed high sensitivity with an average change in threshold voltage of ΔV_{th} = 43 ± 3 mV/pH. Thereafter, the potentiometric detection of Prostate cancer biomarker (prostate specific antigen (PSA)) in pg/ml range was performed by covalent immobilization of PSA-specific aptamers as specific receptor layer on the Si NW FET surface. Furthermore, the devices were integrated with microfluidics and the PSA-aptamer binding on the Si NW FET surface was confirmed by optical assays. In the

end of the thesis work, quantitative, time-dependent detection of other biomarkers such as T cell cytokine (interleukin-4), was executed by connecting the Si NW transistors to a portable measurement system. In an overall view this thesis summarizes an upscale of the fabrication technology for Si NW ISFETs with emphasis on cost-effective, high-throughput fabrication and their usage in various chemical and biomedical applications. Details of the underlying detection mechanisms and future potential as well as limitations of this sensor platform technology are discussed.

List of used acronyms

T	Absolute temperature
AC	Alternating current
Al	Aluminium
APTES	3-aminopropyltriethoxysilane
k	Boltzmann constant
BOX	Buried oxide layer
CVD	Chemical vapour deposition
G	Conductance
λ_D	Debye length
DI	Deionized
DNA	Deoxyribonucleic acid
DRE	Digital rectal examination
DC	Direct current
I_{ds}	Drain-source current
V_{ds}	Drain-source voltage
EDL	Electrical double layer
EBL	Electron-beam lithography
EA	Ethanolamine
FET	Field-effect transistor
FITC	Fluorescein isothiocyanate
FIB	Focussed ion beam
fPSA	Free prostate specific antigen
V_{gs}	Gate-source voltage
T_g	Glass transition temperature
GPTES	Glycidyloxypropyltrimethoxysilane
Au	Gold
HRP	Horseradish peroxidase
HF	Hydrogen fluoride
IHP	Inner Helmholtz plane

IL-2	Interleukin-2
IL-4	Interleukin-4
ISFET	Ion-sensitive field-effect transistor
PI	Isoelectric point
LOC	Lab-on-a chip
LFN	Low frequency noise
MOSFET	Metal oxide semiconductor field-effect transistor
MEMS	Microelectromechanical systems
NIL	Nanoimprint lithography
1D	One dimensional
OHP	Outer Helmholtz plane
PB	Phosphate buffer
PCR	Polymerase chain reaction
POC	Point of care
PMMA	Poly methyl methacrylate
PDMS	Polydimethylsiloxane
PCB	Printed circuit board
PCa	Prostate cancer
PSA	Prostate specific antigen
RCA	Radio Corporation of America
RIE	Reactive ion etching
SNR	Signal-to-noise ratio
Si	Silicon
SiO_2	Silicon dioxide
Si NW	Silicon nanowire
SOI	Silicon on insulator
SRIM	Stopping and range of ions in matter
SS	Subthreshold slope or subthreshold swing
σ_s	Surface-charge density
Ψ_s	Surface potential
S/V	Surface-to-volume ratio

TMAH	Tetramethylammonium hydroxide
T-NIL	Thermal nanoimprint lithography
V_{th}	Threshold voltage
Ti	Titanium
g_m	Transconductance
TRUS	Trans rectal ultrasonography
2D	Two dimensional
UV-lithography	Ultra-violet lithography
UV-NIL	Ultra-violet nanoimprint lithography
ε_0	Vacuum permittivity

Contents

Chapter 1: Introduction

In today's modern world, the human population relies heavily on the technological progress in every aspect of daily life. For instance, in healthcare, the availability of modern techniques for diagnostics and treatment has increased the life expectancy to the highest level of all times.

This is expected to grow even further, due to the new discoveries in science and technology over the last two centuries. Though modern technologies usage provided a favourable living environment, it comes with new challenges, where we now face serious threats such as environmental damage, rapidly changing climate systems, extreme pollution, lessening energy and food resources, etc. The world's large and interconnected population also requires reliable healthcare technologies that provide rapid, accurate diagnosis and medical treatment for chronic and infectious diseases [1-2]. To find answers to these critical challenges, resource-efficient, technical solutions need to be developed that, while reducing the carbon footprint per head, provide us with accurate and fast information.

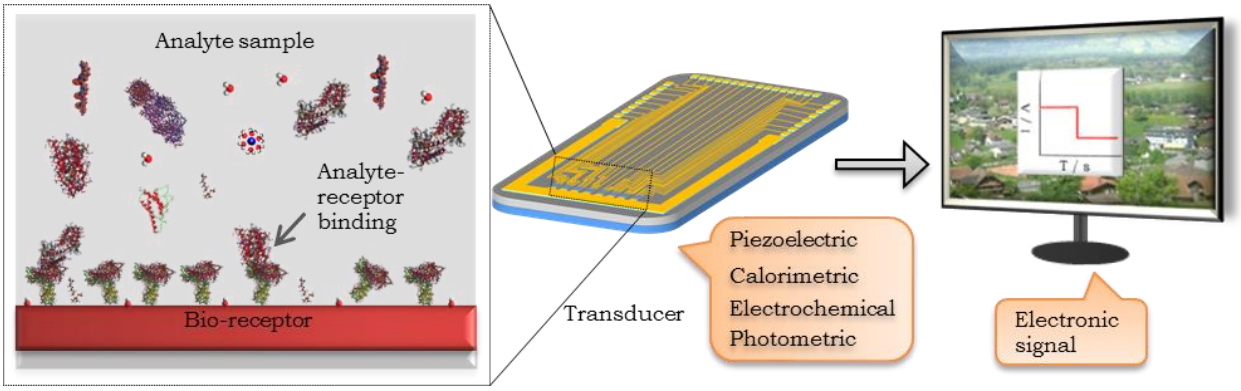

Figure 1.1 Schematic of a label-free biosensor showing the bio-receptor and the transducer: The binding event of the biological analyte (e.g., antibody) over the specific bio-receptor (e.g., aptamer) functionalized transducer surface is converted into a measurable signal that can be electrochemical, photometric, piezoelectric, calorimetric, etc.

For this, new developments in the field of nanoscale electronics at the interface of chemistry and biology have much more to offer in the coming decades. As an illustration, a label-free biosensor in figure 1.1 integrates many interdisciplinary fields such as physics, electronics, chemistry and biology where a chemical/biological event is converted into a measurable signal using a transducing element. Label-free detection methods are advantageous as they give rapid time-course information of the biomolecules binding event and thus enable rapid analyte detection [3-4].

Nanoscale electronic devices in addition to being a fundamental and integral part of modern communications technology are also important towards the development of modern technical solutions in the fields of environmental protection and healthcare [5-8].

Over the past decades, the advancement in nanofabrication techniques resulted in an evolution of nanoscale electronic devices, which were mainly based on silicon (Si) technology [4, 9-13]. The trend in the development of Si microelectronic technology towards lab-on-a chip (LOC) systems is outlined in table 1.1. The core of this evolution in nanofabrication processes and realization of ultra-high-density electronic chips with ultra-high computing performance is the great race towards miniaturization as defined by Moore's Law and is still an ongoing process. Though this trend is based on Si so far, it may continue further with the discovery of new, low-dimensional materials [6, 14-19].

Year	Technology	Company	Ref.
1950's	• Microelectromechanical systems (MEMS): first commercially available Si pressure sensor	Kulite Semiconductor Products	20
1960's	• Integrated circuit: body of semiconductor material, where all components of electronic circuit are integrated		21
	• Complementary metal–oxide–semiconductor logic circuit		
	• Bio-MEMS: shadow-evaporated palladium islands for cell attachment		22
1970's	• Si gas chromatograph		20
	• Si-based microprobes to interface neural tissues, using thin-film and integrated circuit fabrication techniques		23
1980's	• Concept of miniaturised fluidic components such as valves, pumps and channels		20
	• Microfluidic device: home pregnancy test device	Unipath Ltd	20
1990's	• Micro total analysis system for rapid genomics applications-	Novartis	20, 24
	➢ Polymerase chain reaction (PCR)		
	➢ Electrophoresis		
	➢ Deoxyribonucleic acid (DNA) analysis		
	➢ Bio/chemical warfare agent detection		
	• LOC systems-		
	➢ Oligonucleotide chip		25
	➢ Introduction of Polydimethylsiloxane (PDMS) based microfabrication		26
	➢ Continuous flow PCR chip		27

Table 1.1 Timeline of development in microelectronics towards lab-on-a chip systems

Silicon-based nanoscale devices on the other hand, serve as a robust platform for the development of new technologies in various fields such as optics, photovoltaics and sensor applications [13, 28-29]. On account of the well-known properties, easy availability and know-how of the fabrication methods of Si, researchers are able to explore it in nanoscale regime and develop robust Si-based material systems. In this field, silicon nanowires (Si NWs) are at the forefront of miniaturized nanomaterials and have been extensively used for realizing novel sensor platforms due to their high surface-to-volume (S/V) ratio and well-controlled properties achievable in state-of-the-art nanofabrication methods [6, 29-33].

The goal of this thesis was to establish and to utilize a top-down fabrication process for Si NW FETs for biosensing applications. The fabrication process was realized in the clean room facilities of the University of Applied Sciences in Zweibruecken, Germany. The thesis manuscript is divided into 4 main sections - i) “top-down” fabrication of high-density Si NW FETs; ii) basic electrical characterization of the Si NW FETs; iii) electronic and optical sensing of prostate cancer (PCa) biomarker such as the prostate specific antigens (PSA); and iv) real-time detection of T cell cytokines such as Interleukin-4 (IL-4). The short description of the different chapters in this thesis is given in the following paragraphs.

In this thesis, Si NWs were utilized in the form of nano-scale, ion-sensitive field-effect transistors (Si NW ISFETs). The operation principle of the Si NW ISFET is described in chapter 2. When an electronic sensor is deployed in liquid, the solid-liquid interface plays an important role in the resulting sensor responses. Accordingly the inherent nature of this interface and its effects on the field-effect characteristics and sensor performance is discussed. Field-effect sensor platforms primarily depend on the change in the surface-charge at the solid-liquid interface to detect analyte molecules and their performance greatly depends on the nature of the analyte molecules. Variations in the transduction mechanisms used for detection of biomolecules of different sizes and charge distributions are examined.

The origin of Si NWs and their pre-eminence against other semiconducting materials as a suitable candidate for sensor applications are discussed. Other Si NW electronic sensor platforms that have been deployed for various chemicals and biomolecules are described. In addition to this, the advancement of the Si NW sensor platforms over the recent years - for recording of cell signals and interfacing with organs is reviewed. The current limitations of Si NW electronic sensors for chemicals and biomolecules are important measures. Fundamental issues related to field-effect based electrical sensors and possible ways to overcome these limitations of Si NW FET devices are described.

For meaningful sensing applications, it is crucial to achieve highly reproducible sensor characteristics in a scalable fabrication process. Therefore, the synthesis and fabrication of Si NWs devices in terms of scalability and the related fabrication processes divided into top-down and bottom-up types are reviewed. As a result of this discussion the most reliable fabrication techniques available in our facilities for Si NW FETs as they were optimized and used in this thesis work are described.

An overview of the process developed in this thesis work is detailed in chapter 3. For the fabrication process, a new chip configuration for the desired biosensing applications was designed. The different steps optimized and deployed in the fabrication process mainly consisting of nanoimprint lithography (NIL), ultraviolet (UV) lithography and tetramethylammonium hydroxide (TMAH) wet anisotropic etching are discussed. During all fabrication steps it was important to check the correctness and robustness of each individual step. Accordingly, the structural characterization results

at different fabrication process steps are shown. When combining different lithography processes such as NIL and UV lithography consecutively eventual misalignments might occur due to the usage of different machines. Further, on transferring the nano- and micro-structures simultaneously *via* the NIL and RIE processes, there could be issues of improper transfer of the structure patterns from the masks to the wafers. The common problems that occur when combining NIL, UV lithography and subsequent etching processes and their possible control are discussed.

The as fabricated Si NW FETs needed to be encapsulated and surface functionalized in order to use them for reliable sensing applications. The description of the encapsulation procedure of the Si NW FETs to enable robust electrical measurements in liquid gate configuration is given. The Si NW FETs were also integrated with a microfluidic cell to carry out optical measurements. The procedure for the microfluidic channel fabrication using soft lithography is also described. For the reliable sensing of target analyte molecules such as PSA and cytokines, specific receptor molecules need to be immobilized over the Si NW surfaces. The details of the surface functionalization of Si NW FETs for sensing of pH, PSA and IL-4 are also given in chapter 3.

After the encapsulation procedure, Si NW FETs were characterized by basic electrical characterization methods and subsequently deployed for proof-of-principle experiments such as pH sensing. The details of the electrical characterization and pH sensing are given in chapter 4. For this, the Si NW FETs were operated in liquid gate configuration (so called Si NW ISFETs). The measurement setup for these measurements is described in short. The transistors were utilized in phosphate buffer (PB) solution using an external reference electrode for stable applications of the gate-source voltage. By this the characteristics of the Si NW ISFETs and their reproducibility on wafer-scale was analysed. Thereafter, the obtained response of the devices to changes in pH of the buffer solution was examined. The sensitivity, stability and reproducibility of the sensors to time-dependent pH measurements are then described.

In the following biosensor experiments the devices were deployed for detection of PSA, which is the most common biomarker used for prostate cancer diagnosis. The details of the PSA sensing experiments are presented in chapter 5. Other methods available for PCa detection and eminence of PSA as a biomarker are also discussed here. Our Si NW ISFET sensors were deployed for potentiometric detection of PSA using a new analyte-receptor combination on the Si NW surfaces. For PSA detection, PSA-specific DNA aptamers were immobilized covalently over the Si NW surfaces. The obtained response of the sensors to increasing PSA concentrations is shown and described. Additionally, the sensitivities of Si micro (μ) ISFETs available in our research group and the Si NW ISFETs developed in this thesis work for PSA are compared. The PSA-aptamer binding to the Si NW surfaces was also confirmed by optical means as a reference method. The devices were also integrated with a

microfluidic structure for optical detection of PSA. Optical assays such as chemiluminescence and fluorescence were done and are analysed in this chapter 5.

Then in chapter 6 the NW sensors were used for real-time detection of the T cell cytokines IL-4 and the details of these experiments are given here. The importance of different cytokines as biomarkers and alternative detection methods are discussed. The potentiometric detection of recombinant protein IL-4 was carried out by passive adsorption of IL-4 specific receptor antibodies over the Si NW surfaces. The obtained changes in the transfer characteristics of Si NW ISFETs on immobilization of IL-4 were examined and discussed here. Thereafter, quantitative, real-time detection of recombinant protein IL-4 using Si NW ISFETs was successfully done. For these real-time measurements, the Si NW ISFETs were connected to a portable, 4-channel measurement system developed in our research group and the observed changes in the device characteristics are analysed in this chapter. Further the obtained dose response curve from real-time measurements was used to evaluate unknown concentration IL-4 inside the cell culture medium sample of mouse T cells and is described in this chapter.

The thesis is concluded in chapter 7 with conclusion and outlook of the work reported in this thesis. The summary of the overall work and the merits/demerits of the developed Si NW sensor platform are described. In the end future prospects of the realized Si NW ISFETs towards other bio/chemical sensing applications are provided.

Chapter 2: Fundamentals*

In this thesis work, Si NW FETs were used in an ISFET configuration (called as Si NW ISFETs) using an external reference electrode (Ag/AgCl) suspended in the electrolyte solution over the gate oxide covering the Si NW surface. The detailed introduction about the device physics of this Si NW ISFET approach used as central element in this thesis work is given below. For reliable sensing with ISFETs, in general it is important to use a stable reference electrode. Therefore, the working principle and the advantages of conventional reference electrodes such as Ag/AgCl are described. The reactions that occur at the solid-liquid interface, when conventional ISFETs are deployed in liquid gate configuration and the underlying pH sensing mechanism are discussed. There are different transducer principles possible to detect biomolecules with ISFETs. The most common methods are potentiometric and impedimetric sensing. Both principles are described from fundamentals to applications in this section. Further, the progress of ISFET sensors in nano-scale regime i.e., Si NW ISFETs is discussed. A description of Si NW sensors for detection of wide range of chemicals and biomolecules is given. The fabrication methods deployed for the realization of the Si NW sensors in this thesis are also discussed. In the end, inherent limitations that hamper the commercialization of Si NW sensors are discussed as well.

2.1. General working principle of Si NW ISFETs

Firstly introduced by Bergveld [34], ISFETs were used for selective ion detection in an electrolyte by monitoring the drain-source current (I_{ds}) at constant pH. An ISFET is similar to a metal oxide semiconductor field-effect transistors (MOSFET), with a slight modification i.e., the metal/polysilicon gate electrode in MOSFET is replaced by an external reference electrode immersed into the electrolyte solution in contact to the gate oxide.

A schematic of a p-type Si NW ISFET developed in this thesis work is illustrated in figure 2.1. The Si NW ISFETs in our work were realized on silicon on insulator (SOI) wafers. Here, the top Si layer was structured into source and drain electrodes connected by a nanowire channel. The contact lines and NWs were separated from the bulk Si wafer *via* a buried oxide (BOX) layer. Therefore, the charge carriers in the NW channel can be modulated by either applying a potential to an external reference electrode immersed into the electrolyte solution over the gate oxide or to the back-gate electrode connected to the Si substrate. Thus, the Si NW FET can be operated by front gate (V_{gs}) or back-gate-source voltage (V_{bg}) or both at the same time. Additionally, a voltage between the drain and source electrodes (V_{ds}) is applied and the drain-source current (I_{ds}) is measured. Since in the designed ISFET configuration the top Si layer

* Part of the description given in this chapter is submitted (date: 31.08.2017) as a book chapter for publication in Springer books: D. Rani, V. Pachauri, S. Ingebrandt; Silicon nanowire field-effect biosensors.

thickness is between 60-70 nm, the Si NW transistors show partially depleted SOI device characteristics, where a floating body effect hinders the device performance [35].

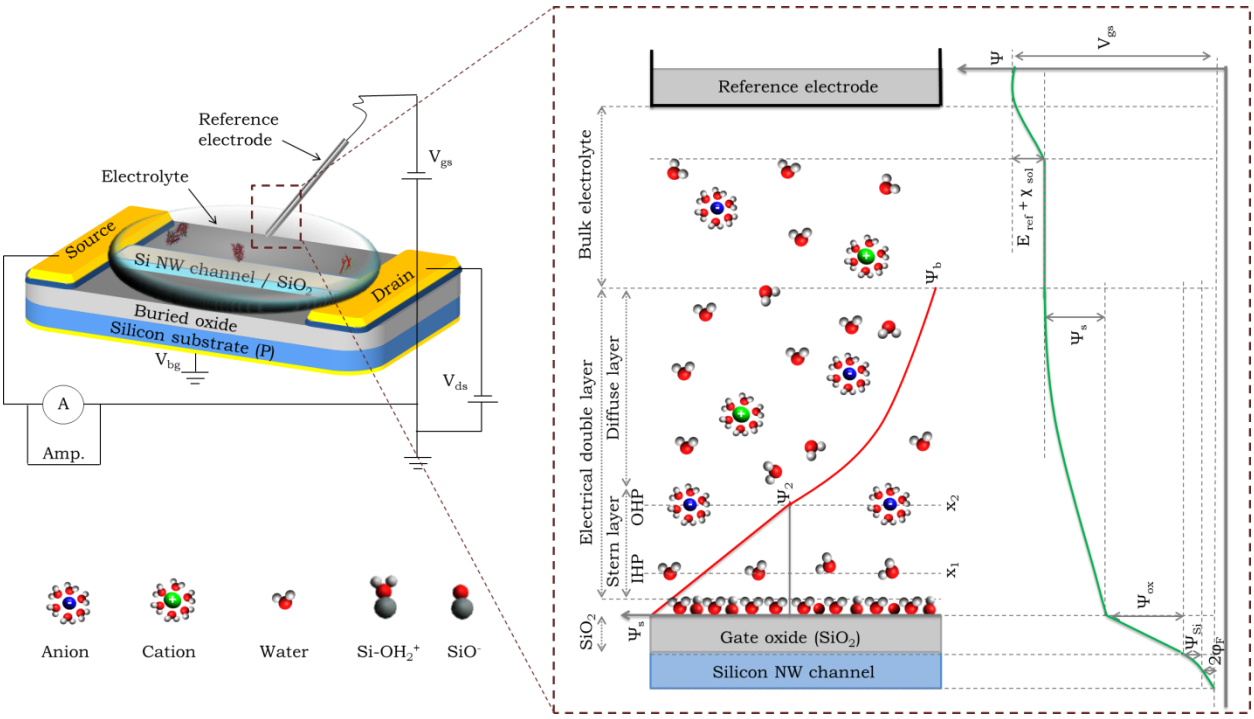

Figure 2.1 Schematic representation of a p-type Si NW ISFET configuration as used in this thesis. It consists of source and drain regions (both p^+-type) connecting the Si NW channel (p-type) covered with a gate oxide (SiO_2) and are separated from the bulk Si substrate *via* a BOX layer. A back-gate voltage (V_{bg}) is applied to the bottom Si substrate (optional), while a front-gate voltage (V_{gs}) is applied to an external reference electrode (Ag/AgCl) suspended into the electrolyte solution. Additionally, drain-source voltage (V_{ds}) is applied and the drain-source current (I_{ds}) is measured. Inset: Schematic of the Gouy-Chapman-Stern model of the electrical double layer at the gate oxide/electrolyte interface (left side) and the reference electrode/electrolyte interface (right side). Left side: According to the Gouy-Chapman-Stern model, in an acidic/basic electrolyte solution, the surface-hydroxyl groups (Si-OH) are protonated ($Si\text{-}OH_2^+$)/deprotonated (SiO^-) resulting in an accumulation of negatively charged/positively charged, solvated ions. The potential profile (red colour) as a function of distance in the EDL is showing a linear drop in potential until the end of the Helmholtz layer, followed by an exponential drop in the diffuse layer, reaching zero potential in the bulk of the electrolyte solution. Right side: Schematic showing the V_{gs} potential drop within an ISFET - at the reference electrode/electrolyte interface ($E_{ref} + \chi_{sol}$), due to EDL near the oxide/electrolyte interface (Ψ_s), within the insulator (Ψ_{ox}) and due to depletion of charge carriers within the Si (Ψ_{Si}).

When the gate oxide (e.g., SiO_2) over the Si NW surface is in contact with the electrolyte solution, an electrical double layer (EDL) is formed at the electrolyte/gate oxide interface with a potential drop over it called surface potential (Ψ_s) (shown in figure 2.1 inset). The surface potential Ψ_s depends on the reactions on the gate oxide surface and is given by the ratio of the surface-charge density (σ_s) on the gate oxide surface and the differential capacitance (C_d) of the EDL, i.e., $\Psi_s = \sigma_s/C_d$. A surface reaction or binding event on the gate oxide surface results in a change in Ψ_s that can

be monitored as change in threshold voltage (V_{th}) of the ISFET and is described in detail in the next sections.

In general this Si NW ISFET device structure is slightly different compared to a conventional ISFET sensor. In the Si NW ISFET structure, the source and drain regions are highly doped (p^+), whereas the NW region is lowly doped (p), but still of p-type. Such a device structure should in principle act as a normally-on FET device. However, the partially or fully-depleted nature of the thin Si structure acts as a normally-off device. The device operation of our p-type Si NW ISFETs is therefore similar to that of p-type planar ISFETs with difference that the used Si NW device is operated in accumulation regime instead of inversion regime. In the absence of a gate-source voltage (i.e., V_{gs} = 0 V), the majority charge carriers (i.e., holes) in the Si NW region are depleted on account of the fixed positive charges in the gate oxide [4, 35]. Thus, the Si NW ISFET is in "off state" at V_{gs} = 0 V.

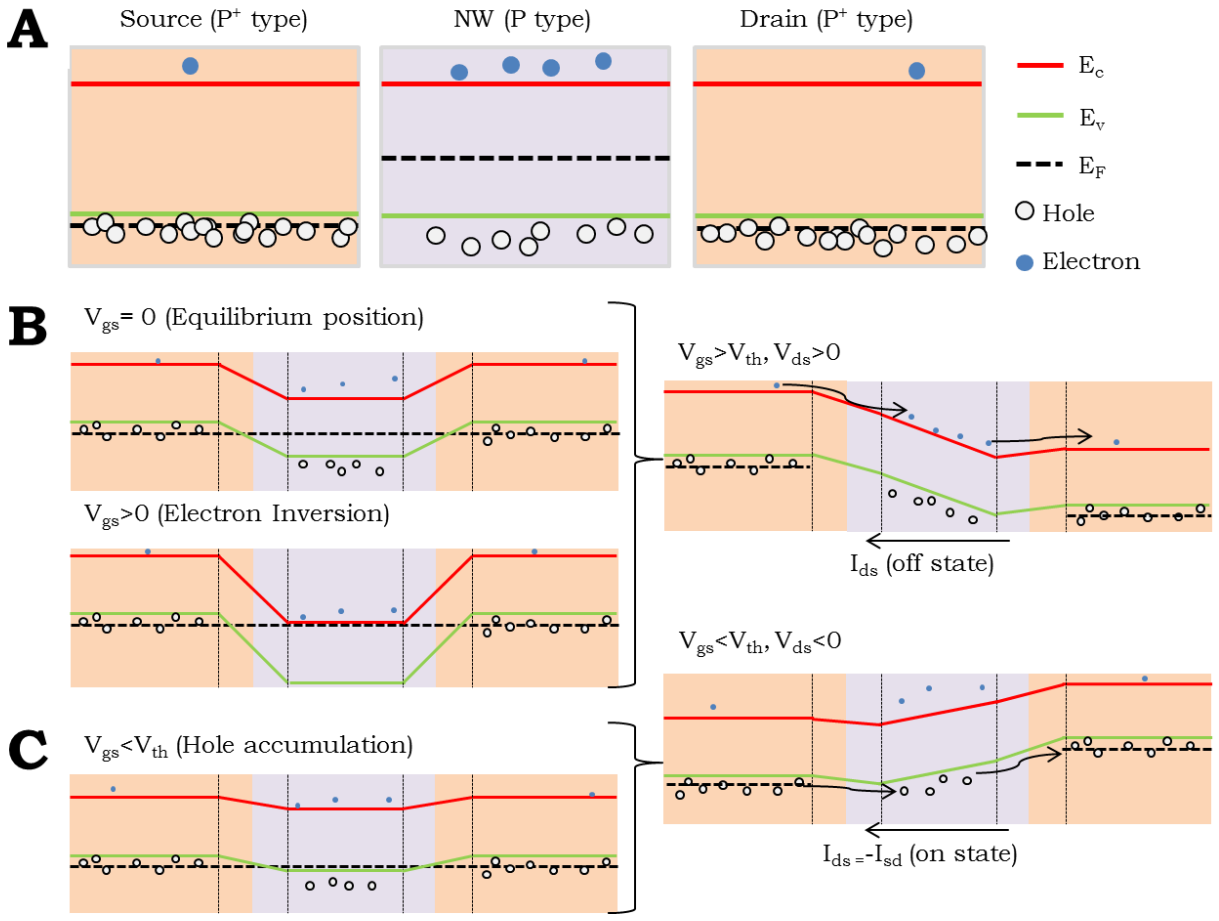

Figure 2.2 Band diagram of a p-type Si NW ISFET: (A) Energy bands of Si NW, source and drain regions are separated from each other; (B) Energy bands of Si NW, source and drain regions in equilibrium condition (V_{gs} = 0 assuming $V_{flat\ band}$ = 0) and electron inversion condition (V_{gs} > 0), "off state" condition (V_{gs} > V_{th}, V_{ds} > 0); and (C) Energy bands of Si NW, source and drain regions in hole accumulation condition (V_{gs} < V_{th}), "on state" condition (V_{gs} < V_{th}, V_{ds} < 0).

The band diagram for the Si NW ISFET is illustrated in figure 2.2. The energy band of source (p^+), drain (p^+) and Si NW (p) regions isolated from each other are shown in figure 2.2. Assuming a flat band condition ($V_{gs} = V_{flat\ band} = 0$) in figure 2.2, it can be observed that when source, NW and drain regions are in contact, in equilibrium condition, the bands in the NW region bend downwards, while in the source and drain regions they bend upwards. A depletion region is created at the interface of source-NW and NW-drain regions. When a positive gate-source voltage is applied ($V_{gs} > 0$), the bending of bands increases in the NW region, and the Fermi level (E_F) is closer to the bottom of the conduction band (E_C), leading to an inversion of charge carriers in the p-type NW region (electrons are closer to the Fermi level). Therefore, a $p^+/n/p^+$ junction between source/NW/drain is formed and on application of a drain-source voltage ($V_{ds} > 0$, $V_{gs} > 0$), the transistor is in "off state". The only flow of current is due to the minority charge carriers (electrons) from the source to drain regions as it is shown in figure 2.2 B right side. On the other hand, when a negative voltage is applied at the gate ($V_{gs} < 0$), the bands in the Si NW region shift upwards and below a certain threshold voltage called V_{th}, the Fermi level is closer to the valence band (E_V) leading to an accumulation of holes in the Si NW region (figure 2.2 C left side). Thus, a $p^+/p/p^+$ junction is formed between the source/NW/drain regions. On application of a drain-source voltage ($V_{ds} < 0$), there is a flow of majority charge carriers (holes) from the source to the drain region leading to a drain-source current and the transistor is in "on state" (figure 2.2 C right side).

Since the sensing mechanism of the long channel, p-type Si NW ISFET developed in this thesis work is very similar to that of a planar p-type ISFET, in the following subsections the discussion is restricted to a planar p-type ISFET.

2.1.1. Threshold voltage of an ISFET

In an ISFET, at the interface of the gate oxide and the electrolyte solution protonation or deprotonation of surface-hydroxyl group (Si-OH for SiO_2 as gate oxide) take place depending on the pH of the electrolyte solution. There exists an EDL up to a certain length within the electrolyte solution as it was already illustrated in figure 2.1 (inset left side). The reaction mechanism at the gate oxide/electrolyte solution interface depends on the pH of the electrolyte solution. The voltage applied at the reference electrode (V_{gs}), drops at the reference electrode/electrolyte interface, at the EDL near the gate oxide/electrolyte interface, at the gate oxide layer and at the Si layer under the gate oxide (figure 2.1 inset right side). These potential drops depend on the type of reference electrode, electrolyte-solution composition, gate oxide charges and doping level of the Si layer below the gate oxide, respectively [36]. The threshold voltage of an ISFET is given by-

$$V_{th} = E_{ref} - \Psi_s + \chi_{sol} - \frac{\Psi_{Si}}{q} - \frac{(Q_{ox} + Q_{ss})}{C_{ox}} - \frac{Q_B}{C_{ox}} + 2\Phi_F \qquad (2.1)$$

-where E_{ref} is the reference electrode potential related to vacuum which is a constant. The two parameters Ψ_s and χ_{sol} are defining the interfacial potential at the electrolyte/oxide interface, from which χ_{sol} is the surface dipole potential of the electrolyte and has a constant value as well. Ψ_s is the surface potential, resulting from the ionic distribution at the electrolyte/oxide interface. Ψ_{Si} is the Si work function and q is the elementary charge. Φ_F is the difference in Fermi level of the intrinsic Si and the actual Fermi level of the Si layer between the source and drain regions. A potential change of $2\Phi_F$ at the Si surface is required to initiate the inversion of charge carriers [35-36]. The values Q_{ox}, Q_{ss} and Q_B are the fixed charges in the oxide, at the oxide-Si interface and the depletion charges in the Si, respectively, and C_{ox} is the capacitance of the gate oxide layer [35].

For an ISFET in practical applications, a reference electrode is used to provide a stable potential E_{ref} and all other components are approximated to be constant in equation 2.1, with Ψ_s the only variable. As described earlier, Ψ_s depends on the surface reactions at the gate oxide, where the surface-charge is either due to protonation or deprotonation of surface-hydroxyl groups depending on the pH (Ψ_s = f(pH)) or due to binding of charged molecules to the surface. Thus, the ISFET is sensitive to a change in pH and to the binding of charged biomolecules at the same time, resulting in a pH sensor and a biosensor [4].

In the case of $V_{gs} > V_{th}$, the transistor is weakly inverted and a so called subthreshold drain-source current I_{ds} is flowing. This process is diffusion limited and it increases exponentially with V_{gs},

$$I_{ds} \propto e^{2.3\frac{V_{gs}-V_{th}}{SS}} \tag{2.2}$$

-where SS represents the subthreshold slope (also called subthreshold swing, $SS = (\frac{\partial V_{gs}}{\partial \log I_D})$) of the ISFET.

A small SS is desirable as it implies that the device can switch rapidly from the “off state” (where the drain-source current is very small) to the “on state” with only a small applied bias. When the transistor is operated in the subthreshold region, the current sensitivity is higher (i.e., $\Delta I_{ds}/I_{ds}$) since the drain-source current I_{ds} depends exponentially on V_{gs}.

In the case of $V_{gs} < V_{th}$ and for small V_{ds}, the I_{ds} is dominated by the drift current,

$$I_{ds} = \frac{W}{L}\mu_p C_{ox}(V_{gs} - V_{th})V_{ds} \tag{2.3}$$

-where W, L are the width and length of the semiconducting channel, μ_p is the hole mobility and C_{ox} is the gate oxide capacitance.

Thus, for small V_{ds}, the current-voltage relation is linear for a given V_{gs} and the transistors behaves as a resistor.

When V_{ds} is increased further ($|V_{ds}| > |V_{gs}-V_{th}|$), the drain-source current reaches a saturation level and becomes constant. The transistor is in the "pinch off" state at $V_{ds} = V_{gs}-V_{th}$ and a further increase in V_{ds} results in a shift of the pinch off point towards the source contact. In the saturation regime the drain-source current (ignoring the short channel effects) is given by-

$$I_{ds} = \frac{W}{L}\mu_p C_{ox}(V_{gs} - V_{th})^2 \tag{2.4}$$

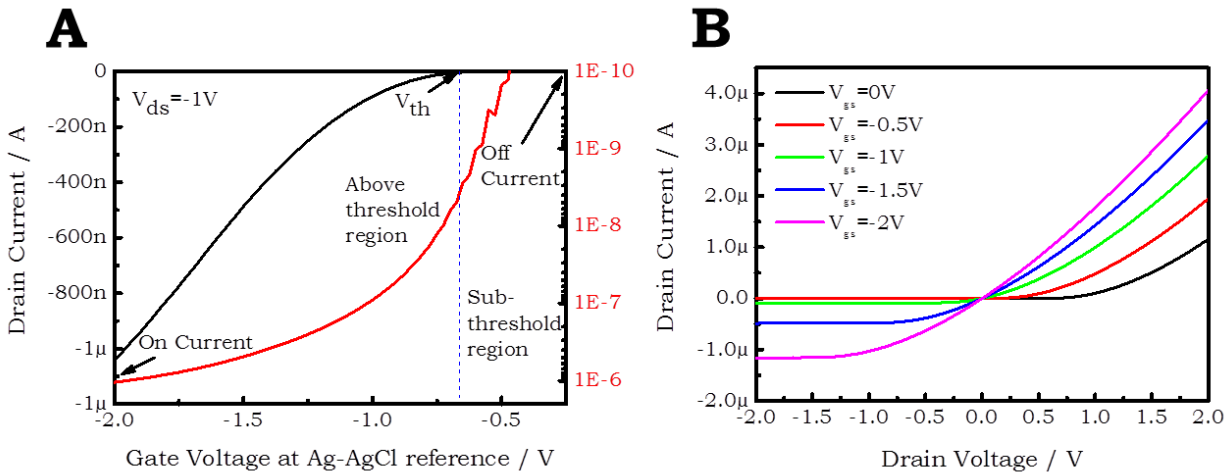

Figure 2.3 Characteristics of a p-type Si NW ISFET: (A) Transfer characteristics showing the variation of I_{ds} as a function of V_{gs} in linear scale (left side) and in log scale (right side) at V_{ds} = -1 V; and (B) Output characteristics showing I_{ds} as a function of V_{ds} at varying V_{gs} from 0 V to -2 V.

The transconductance (g_m) of an ISFET is given by the ratio of the change in drain-source current I_{ds} (as a function of gate-source voltage V_{gs}) to the change in gate-source voltage V_{gs} at constant drain-source voltage V_{ds},

$$g_m = \frac{\partial I_{ds}(V_{gs})}{\partial V_{gs}}\Bigg]_{V_{ds}=constant} \tag{2.5}$$

Thus, for a linear operation mode of the transistor, it is

$$g_m = \frac{W}{L}\mu_p C_{ox} V_{ds} \tag{2.6}$$

For the saturation mode of the transistor, it is

$$g_m = \frac{2W}{L}\mu_p C_{ox}(V_{gs} - V_{th}) \tag{2.7}$$

The transconductance reflects the sensitivity of the ISFET device as a higher g_m value results in a higher change in I_{ds} for a given change in V_{gs}.

The electrical characteristics of a p-type Si NW ISFET measured in a PB solution at pH 7.4 are shown in figure 2.3. In transfer characteristics (figure 2.3 A), I_{ds} is measured as a function of V_{gs} at a fixed V_{ds} = -1 V and is plotted in linear scale (left side) and in logarithmic scale (right side). In linear scale (black curve) no current flows below the threshold voltage (V_{th}), whereas in log scale (red curve) the current increases exponentially below V_{th}. The g_m value can be calculated from the first derivative of the transfer characteristic curve in linear scale. Typically V_{gs} at the maximum g_m value is chosen as the working point of the ISFET for a given V_{ds}. The subthreshold swing SS can be calculated from the log scale plot of I_{ds} *vs* V_{gs} and was 135 mV/decade in this exemplary case.

The output characteristics of the Si NW ISFET are shown in figure 2.3 B, where I_{ds} is measured as a function of V_{ds}, for a fixed V_{gs} varying from 0 to -2 V in steps of 0.5 V. As it can be interpreted from the graph, there is no I_{ds} for (V_{ds} < 0) below the V_{th} (V_{th} = -0.66 V) i.e., for V_{gs} = 0 V, -0.5 V. Whereas the I_{ds} increases linearly with increase in V_{ds} (low) for V_{gs} above the V_{th} i.e., for V_{gs} = -1 V, -1.5 V and -2 V. For higher V_{ds} ($|V_{ds}| > |V_{gs}-V_{th}|$), the current saturates and the I_{ds} values only depend on the applied V_{gs}.

2.1.2. Reference electrode/electrolyte junction

The threshold voltage of an ISFET depends on the change in surface potential ($\Delta\Psi_s$) caused either by surface reactions or biomolecular binding at the gate insulator, only when the potential at the reference electrode (E_{ref}) is stable. For a stable E_{ref}, the gate-source voltage is applied to a reference electrode that possesses a well-defined electrode reaction to keep the electrode potential stable. An electrochemical Ag/AgCl reference electrode typically contains an internal filling of 3M KCl that provides an electrochemically stable interface with the reference electrode *via* a well-defined redox reaction between silver metal (Ag) and its salt (AgCl) [37].

$$Ag^+ + \bar{e} \rightleftharpoons Ag(s)$$

$$AgCl(s) \rightleftharpoons Ag^+ + Cl^-$$

The overall reaction can be written as

$$AgCl(s) + \bar{e} \rightleftharpoons Ag(s) + Cl^- \quad (2.8)$$

The reference electrode solution (KCl) is separated *via* a liquid junction from the electrolyte solution, minimizing the mixing of reference electrode solution and electrolyte. The liquid junction provides an electrical connection to the electrolyte solution (*via* the redox reaction - dissolution of Ag metal or deposition of silver ions on the cathode), but the potential at the reference electrode is independent of the electrolyte solution composition.

The Ag/AgCl reference electrode/reference electrode solution (KCl) junction potential (φ_{me}) depends on-

$$\varphi_{me} = 59.2log_{10}a_{Cl^-} + const. \quad (2.9)$$

-where, a_{Cl^-} is the activity of Cl^- ions (effective concentration of Cl^- ions) and this is constant in the internal filling solution KCl of the Ag/AgCl reference electrode.

Thus, φ_{me} is constant for the Ag/AgCl reference electrode and E_{ref} is stable for a constant gate-source voltage applied. The reference electrode is usually much bigger than the transistor chip. Therefore for device integration other options of usage of inert metal electrodes (e.g., Pt, Au) as reference electrode were tried out. However, the lack of well-defined electrode reactions results in unstable φ_{me}, when the inert metal electrodes are immersed in electrolyte solutions for biological measurements. Therefore the usage of an external reference electrode is unavoidable in biological applications of ISFETs.

2.2. pH sensing mechanism of ISFETs

In an ISFET the gate oxide (e.g., SiO_2) is in direct contact with the electrolyte solution in which the external reference electrode is suspended to modulate the charge carriers in the semiconducting channel between the source and drain electrodes. The gate oxide, SiO_2 contains a high density of surface-hydroxyl groups (Si-OH) on the surface, which can be neutral or undergo protonation (positively charged) or deprotonation (negatively charged) depending on the pH of the electrolyte solution. This leads to a net surface-charge density (σ_s) that depends on the chemical equilibrium of the surface reactions and an EDL is formed on the oxide surface. The pH sensing mechanism of ISFETs depends on the surface potential (Ψ_s) at the oxide surface, which is a function of pH of the electrolyte solution, Ψ_s = f(pH) [36]. From the site-binding model, it is known that acid/base reactions take place between the gate oxide surface-hydroxyl groups (Si-OH) and the hydrogen ions (H^+) in the electrolyte solution. This can be described by two dissociation constants K_a and K_b [36, 38-39].

$$Si - OH \rightleftharpoons SiO^- + H^+, with\ K_a = \frac{[SiO^-][H^+]_s}{[Si - OH]} \quad (2.10)$$

$$Si - OH_2^+ \rightleftharpoons Si - OH + H^+, with\ K_b = \frac{[Si - OH][H^+]_s}{[Si - OH_2^+]} \quad (2.11)$$

-where $[H^+]_s$ (also called activity of H^+ ions at the surface) is the concentration of H^+ ions at the surface. The other quantities in the square brackets represent the numbers of surface sites per unit area.

The surface potential Ψ_s is governed by the charges and its strength decays away from the surface with zero potential in the bulk of the solution (as the solution is electrically neutral). Due to the protonation/deprotonation of hydroxyl groups at the

oxide surface, there is a difference in hydrogen (H^+) ion concentration near the surface and the bulk of the electrolyte solution. The surface concentration of H^+ ions can be related with the bulk H^+ ions concentration (also called the activity of H^+ ions in the bulk of the solution) by using the Boltzmann distribution-

$$[H^+]_s = [H^+]_b \exp(-\frac{q\Psi_s}{kT})$$

$$pH_s = pH_b + \frac{q\Psi_s}{2.3kT}, \text{with}$$

$$pH_s = -log_{10}[H^+]_s, \qquad pH_b = -log_{10}[H^+]_b \tag{2.12}$$

-where k represents the Boltzmann constant and T represents the absolute temperature.

The total density of surface sites (N_s) on the gate oxide is estimated as-

$$N_s = [Si-OH] + [SiO^-] + [Si-OH_2^+] \tag{2.13}$$

In general, the parameters K_a, K_b and N_s depend on the type of gate insulator.

The surface-charge density (σ_s) due to the surface-hydroxyl groups is given by the difference in number of positively charged groups and negatively charged groups per unit area-

$$\sigma_s = q([Si-OH_2^+] - [SiO^-]) = qN_s\left(\frac{[H^+]_s^2 - K_aK_b}{K_aK_b + K_b[H^+]_s + [H^+]_s^2}\right) = -q[B] \tag{2.14}$$

-where [B] represents the difference in number of negatively charged groups and positively charged groups [39].

At pH of point-of-zero-charge ($pH_{pzc} = \frac{pK_a + pK_b}{2}$) the number of positively charged groups equals the number of negatively charged groups giving a zero net charge, [B] = σ_s = 0 and $pH_{pzc} \approx 2$ for SiO_2. At a pH below pH_{pzc} the oxide surface is positively charged and at a pH higher then pH_{pzc} the oxide surface is negatively charged.

Dividing eq. 2.14 with pH_s and differentiating-

$$\frac{\delta\sigma_s}{\delta pH_s} = -q\frac{\delta[B]}{\delta pH_s} = -q\beta_{int} \tag{2.15}$$

-where β_{int} is the intrinsic buffer capacity, which gives the change in number of charged groups due to change in surface pH. It is a measure of charging capability (protonation or deprotonation) of the oxide surface with changes in pH of the solution and depends only on the intrinsic properties of the surface, i.e., N_s, K_a and K_b (thus is different for different gate insulators).

Due to the charge neutrality requirement, an equal amount of charge σ_{EDL} with opposite polarity appears on the electrolyte side of the EDL. The details of the EDL are shown in figure 2.1 inset left side. According to the simple Gouy-Chapman-Stern model the solution side of the double layer is composed of several layers - Helmholtz or Stern layer (which contain solvent molecules, sometimes specifically adsorbed analytes) and a diffuse layer (DL) [40]. Specifically adsorbed ions and molecules lie closest to the oxide surface and the locus of their electrical centres is called the inner Helmholtz plane (IHP), which lies at a distance of x_1 from the oxide surface. The σ_s is counterbalanced by solvated ions, which can approach the oxide surface only to a distance x_2. The locus of the centre of nearest solvated ions is called the outer Helmholtz plane (OHP) as illustrated in figure 2.1 inset left side. It can be observed that the concentration of the solvated counter ions decreases from the OHP to the bulk of the electrolyte forming a DL. Since the interaction between the surface-charge and the solvated counter ions is *via* electrostatic force, a thinner DL is anticipated in a higher ionic strength electrolyte due to the stronger screening effect. As the distance from the oxide surface towards the electrolyte solution is increased, the Ψ_s drop is roughly linear inside the Helmholtz layer (upto Ψ_2), while it decreases exponentially in the DL having a zero value at the imaginary boundary of the double layer (Ψ_b). The total distance from the oxide surface in the electrolyte solution, where the potential drops to $1/e$ of its value at the oxide is called Debye length (λ_D). For a given electrolyte solution, λ_D is estimated as-

$$\lambda_D = \sqrt{\frac{\epsilon_0 \epsilon_r \, kT}{2q^2 P}} \; where \; P = \frac{1}{2}\sum c_i z_i^2 \tag{2.16}$$

-where ε_0 represents the vacuum permitivity, ε_r represents the dielectric constant of the electrolyte solution, P represents the ionic strength of the electrolyte and c_i, z_i represent the concentration and valance ion of electrolyte components.

The charge density at the oxide surface (σ_s) is equal and opposite to the charge density in the electrolyte side of the double layer ($-\sigma_{EDL}$) with no counter ions in the IHP-

$$\sigma_s = -\sigma_{EDL} = \sigma_{OHP} + \sigma_{DL} \tag{2.17}$$

-where σ_{OHP} and σ_{DL} represent the charge densities in the OHP and in the diffuse layer, respectively [39].

According to the Gouy-Chapmann model, the solvated counter ions in the solution are electrostatically attracted towards the surface. However, this attraction is counteracted by the random thermal motion, which tends to equalize the concentration throughout the solution [4]. The relation between surface-charge density σ_s and surface potential Ψ_s is given by the Grahame equation-

$$\sigma_s = -\sqrt{8kT \in_0 \in_r c_i} \sinh\left(\frac{z_i q \Psi_s}{2kT}\right) \quad (2.18)$$

Alternatively, the double layer charge can be related to the double layer capacitance (C_{EDL}) (sum of the capacitance of stern layer and diffuse layer)-

$$\sigma_s \approx C_{EDL} \Psi_s \quad (2.19)$$

$$\frac{\delta \sigma_s}{\delta \Psi_s} \approx C_d \quad (2.20)$$

Combining equation 2.15 and 2.20, the dependence of Ψ_s on pH_b can be obtained as-

$$\frac{\delta \Psi_s}{\delta pH_b} = -2.3 \frac{kT}{q} \alpha, \text{where } \alpha = \frac{1}{1 + 2.3 \frac{kT C_d}{q^2 \beta_{int}}} \quad (2.21)$$

-where α is a dimensionless sensitivity parameter with a value varying between 0 and 1. For high β_{int} with low C_d values α will be close to 1. In this ideal case maximum pH sensitivity can be expected.

From equation 2.21, the upper limit of pH sensitivity of an ISFET, called the Nernst limit, can be obtained (= 59.2 mV/pH at 25 °C) with α = 1. The best gate insulator for ISFET pH sensors is Ta_2O_5 as its β_{int} value is highest known in the field, with nearly ideal pH response (= 59.2 mV/pH at 25 °C) and it is inert to changes in the ionic strength of the solution.

2.3. Biomolecule detection using ISFETs

On functionalizing the oxide surface with analyte-specific receptors, the ISFETs can be used for sensitive and selective, label-free detection of various biomolecules such as DNA, proteins, enzymes and cells etc. There are two different mechanisms for the detection of biomolecules - potentiometric and impedimetric detection. The potentiometric or direct current (DC) method is a charge-based detection method, where binding of the charged molecules at the gate oxide results in a change in Ψ_s at the oxide-electrolyte interface. In the impedimetric or alternating current (AC) method, the binding of biomolecules results in a change in input impedance of an ISFET due to the passive components of the biomolecules such as resistance and capacitance [4]. Details of the two methods are given in the following subsections.

2.3.1. Surface-charge based detection method

The detection of charged molecules can be explained by a similar model as for pH with addition of a charge screening effect. In the case of pH sensing the reactive groups (-OH) lie closer to the surface, within the Debye length, for most electrolyte concentrations used. However, for biomolecule detection specific receptors of different sizes need to be chosen and the electrolyte concentration needs to be optimized accordingly, so that the receptor-analyte binding events take place within the Debye

length. Biomolecules such as proteins consist of a sequence of amino acids and their net charge depends on the amino acid composition and the pH of the surrounding electrolyte solution. Depending on the characteristic isoelectric point (pI) of each protein, it carries a net positive charge at pH below the pI and a net negative charge above its pI. Therefore, it is assumed that the binding of the receptor-analyte proteins to the gate oxide results in a net change in charge ($\Delta\sigma_s$), thereby resulting in a net change in surface potential ($\Delta\Psi_s$). Since the Debye length is ≈ 1 nm in physiological solutions, the bound antibodies with dimensions ≈ 10 nm are lying outside the Debye length and are not seen as their charge is shielded by the counter ions of the solution. An example for this is illustrated in figure 2.4 A. The Debye length can be increased by decreasing the electrolyte concentration. However, this could result in a lower analyte binding affinity as this is hindered in low electrolyte concentrations [39].

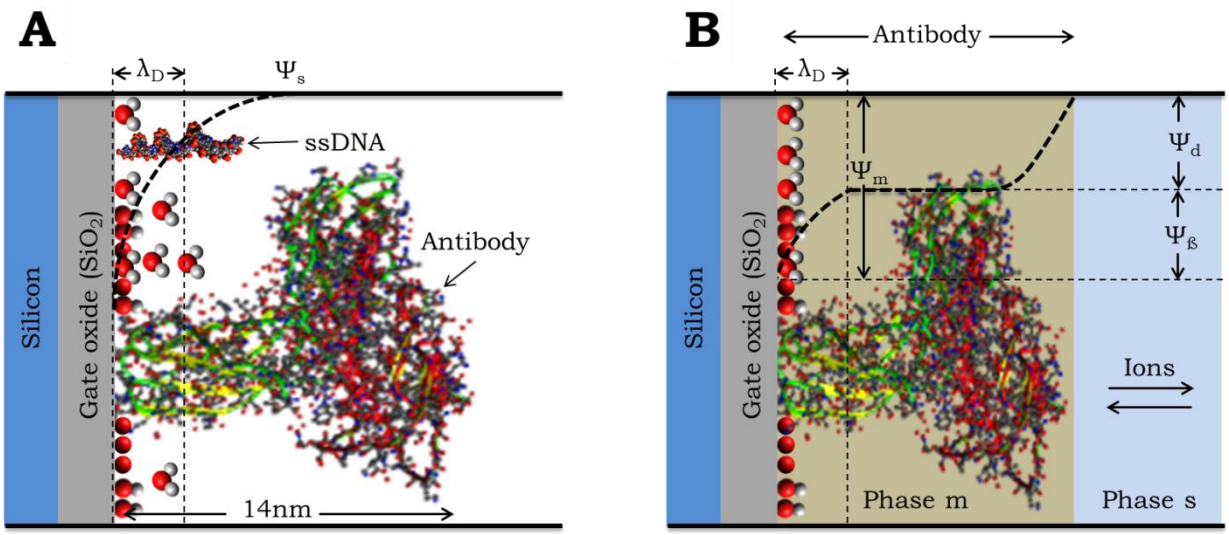

Figure 2.4 (A) Schematics of the Debye screening of charges in a buffer solution for two receptor molecules - single stranded (ss) DNA and antibody. The fraction of biomolecule charge that remains within the Debye length will alter the ISFET signal; and (B) Donnan equilibrium showing the change in ISFET signal on antibody binding as a result of change in Donnan potential ($\Delta\Psi_d$) and surface potential ($\Delta\Psi_s$).

The detection of proteins by the above-mentioned method is quite complicated as it is difficult to determine the exact charge of bound proteins on the gate oxide surface. Due to the difference in pH at the surface and the bulk of the electrolyte solution, as given by equation 2.12, it is difficult to determine the protein charge polarity, when the protein is near to the gate oxide surface [41]. Different effects have been proposed to explain the observed changes in the electronic signals upon binding of the proteins. As one component of this a notable effect called Donnan effect has been used to explain the binding of proteins. Protein receptors are considered as a membrane deposited on the gate insulator in Donnan equilibrium, with protein membrane as phase “m”, and solution as phase “s”. Due to the presence of fixed charges in the protein membrane, there will be a diffusion of ions between the two phases, giving rise to a potential drop,

the Donnan potential Ψ_d. In the equilibrium condition, the electrochemical potential of ions in phase m and s should be equal and Ψ_d is given by-

$$\Psi_d = \Psi_m - \Psi_ß = \frac{kT}{q} \ln \frac{\sqrt{4c_s^2 + c_x^2} + c_x}{2c_s}, \quad (2.22)$$

-where Ψ_m and $\Psi_ß$ give the electrical potentials in phase m and s, respectively; c_s is the concentration of salt in the electrolyte and c_x is the effective fixed charge density in the protein membrane [41].

On binding of the analyte proteins to the receptor proteins on the gate oxide, the effective fixed charge density in the protein membrane, c_x, will change leading to a change in Ψ_d. From equation 2.22 it can be seen that $\Delta\Psi_d$ will be less for higher salt concentration of the electrolyte, c_s. On account of the change in Ψ_d, there will be a change in pH in phase m, where $\Delta pH = q\Delta\Psi_d/2.3kT$. The change in pH in membrane m leads to a change in surface potential ($\Delta\Psi_s$) at the oxide, as it can be related from equation 2.21. Therefore, the change in V_{th} of an ISFET on protein binding is as a result of the change in Donnan potential ($\Delta\Psi_d$) at the protein membrane/solution interface and the change in surface potential ($\Delta\Psi_s$) at the oxide/protein membrane interface as illustrated in figure 2.4 B,

$$\Delta V_{th} = (1 - \alpha)\Delta\Psi_d \quad (2.23)$$

In the case of an ideal Nernstian behaviour (i.e., $\alpha = 1$) there is no change in V_{th} on protein binding, since the $\Delta\Psi_d$ is compensated by $\Delta\Psi_s$ (on account of the change in membrane pH). Nonetheless, for non-ideal Nernst response ($\alpha < 1$), there is a change in V_{th} on binding of protein at the gate oxide.

Moreover, in a recent report by De Vico and co-workers it has been demonstrated that the surface potential change is not only due to the binding of the analyte at the surface, but also due to net charge of the receptor-analyte complex contained within the Debye length. Thus even if the analyte protein lies outside the Debye length, on binding to the receptor protein over the gate oxide surface, the net charge of the receptor-analyte protein complex changes, resulting in a change in V_{th} [42-43].

Other biomolecules such as single-stranded DNA (ssDNA) molecules, that are commonly used as receptors for proteins or for complementary DNA strand detection, consist of a negatively charged phosphate backbone and the charge is evenly distributed throughout their cylindrical structure [44]. As a DNA molecule consists of a nucleotide sequence, where the length of a single nucleotide is about 0.34 nm, in physiological solutions also some nucleotides will lie within the Debye length as illustrated in figure 2.4 A. Therefore it is possible to detect the charge redistribution at the oxide/electrolyte interface due to ssDNA-protein binding or DNA hybridization process.

Although the potentiometric method of ISFETs was reported for sensitive detection of various biomolecules such as proteins, cells, DNA, viruses, mapping of neural circuits, etc., the use of only potentiometric readout using ISFETs remains elusive for real applications concerning the detection of large molecules, cells and larger living systems for high sensitivity and high resolution sensor recordings [1, 10, 45-49].

2.3.2. Impedimetric method of detection

The detection of biomolecules using ISFETs can also be done *via* an impedimetric method, where the bound biomolecules on the gate insulator result in a change in input impedance, leading to a change in total impedance of the ISFET. The response of an ISFET to an applied AC signal at the gate input depends on the frequency of the applied signal. The binding of biomolecules on the gate insulator results in change in frequency response of the ISFET [4]. An ISFET with a physically bound bio-membrane, e.g., a protein layer on top of the gate insulator, can be represented in a first approximation by a simplified electronic circuit as given in figure 2.5 A [50]. Here, the membrane impedance can be divided into two parts as a bulk impedance in series with a membrane/electrolyte interface impedance. The bulk membrane impedance can be described by a parallel combination of bulk resistance (R_{mem}) and bulk capacitance (C_{mem}). The impedance of the membrane/electrolyte interface is represented as double layer capacitance (C_{EDL}) in parallel with a series combination of charge transfer resistance (R_{ct}) at the interface and Warburg impedance (Z_w) i.e., due to the diffusion of ions. The ISFET impedance also includes other contributions from the Si channel and the gate oxide and includes a series combination of Si electrode resistance (R_{Si}), space charge capacitance (C_{sc}) and capacitance of the gate oxide (C_{ox}). When the ISFET is operated in the inversion regime, C_{sc} is much smaller than C_{ox} and therefore can be neglected. Also R_{Si} and R_{sol} are much smaller than the membrane resistance R_{mem}. The interfacial effects of the membrane impedance are detectable only at low frequencies (≤ 5Hz), while the charge transfer resistance is too small to be observed due to rapid exchange of ions at the interface. Therefore, at higher frequencies (≥ 5Hz), the circuit can be simplified to a series combination of C_{ox} with an element consisting of C_{mem} and R_{mem} in parallel (figure 2.5 B). The relaxation time, τ i.e., the time required for redistribution of the charges and establishment of electrical profiles in the membrane after the application of a gate-source voltage, is determined by these few circuit components.

Moreover, in some other ISFET models as illustrated in figure 2.5 D, additional components are considered. For instance, when no membrane is attached to the gate oxide, the contact line capacitance ($C_{cl} = C_s + C_d$, C_s in parallel with C_d), and the solution resistance (R_{sol}) dominate, because of the large area of the contact lines region, while the reference electrode resistance (R_{ref}) can be neglected ($R_{ref} << R_{sol}$ for low conc. electrolyte). Because of the parasitic effect of contact line capacitance (C_{cl}), and solution resistance (R_{sol}), a low-pass filter is formed with a time constant (τ_{co}) and signals above the cut-off frequency are attenuated [51]. The overall time constant of the system is then-

$$\tau_{co} = \frac{1}{f_{co}} = C_{cl}(R_{sol} + R_{ref}) \approx C_{cl}R_{sol} \quad (2.24)$$

-where f_{co} is the cut-off frequency of the signal.

This cut-off frequency can be adjusted and optimized by using specific material, thickness of the passivation layers over the source and drain contact lines and also by choosing a high band-width operational amplifier [51-53]. Additionally, the impedance response of ISFETs strongly depends on the concentration of the electrolyte solution and the position of the reference electrode with respect to the gate oxide surface, in particular when recordings in diluted buffer solutions are done [4, 51].

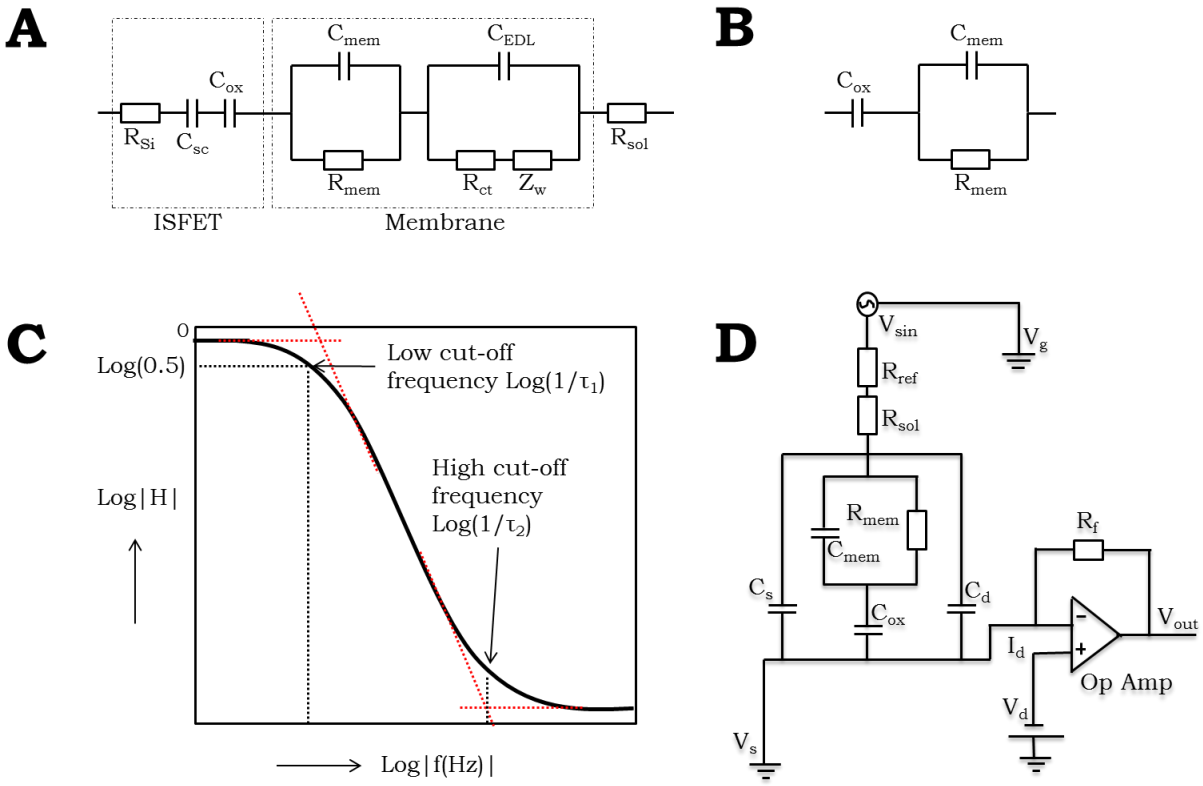

Figure 2.5 (A) Complete equivalent circuit of an ISFET with the gate oxide covered by a membrane; (B) Simplified equivalent circuit of an ISFET functionalised with a membrane; (C) Theoretical transfer function for an ISFET with a membrane on the gate oxide and an extrapolation to extract the time constants τ_1 and τ_2 [54]; and (D) The electronic readout circuit of ISFET with a membrane at the gate oxide [53].

The simplified input gate circuit, shown in figure 2.5 B, can be characterized by a transfer function (H(jω)), i.e., a mathematical relation between the input and the output signals of a frequency-dependent system. A DC voltage applied between gate and source electrodes (V_{gs}) causes a flow of current (I_{ds}) between drain and source electrodes. When this V_{gs} is superimposed with a small sinusoidal voltage δV_{gs} as AC input signals, this is generating a δI_{ds} in the channel. This results in a frequency-

dependent transconductance, $g_m = \delta I_{ds}/\delta V_{gs}$ [50, 54]. The output voltage, V_{out}, of the operational amplifier, shown in figure 2.5 D, is then related to I_{ds}, g_m, V_{gs} by

$$V_{out} = -R_f I_{ds} = -R_f g_m V_{gs} \tag{2.25}$$

-where R_f represents the feedback resistance of the operational amplifier.

When a bio-membrane, for instance a protein layer or a DNA layer, are attached to the gate oxide, the applied gate-source voltage drop takes place partially at the membrane and partially at the oxide. Thus, the applied V_{gs} is larger than the effective potential difference between the gate and source. In this case a frequency-dependent component H(jω) needs to be included as a multiplication factor of V_{gs}.

$$V_{out} = -R_f g_m H(j\omega) V_{gs}, where \tag{2.26}$$

$$H(j\omega) = \frac{1 + j\omega R_{mem} C_{mem}}{1 + j\omega R_{mem}(C_{mem} + C_{ox})} \tag{2.27}$$

The relation between the transfer function and the frequency response is plotted in figure 2.5 C and the intersections of the linear part of the curve represent the time constant of the simplified circuit [54].

$$\tau_1 = R_{mem}(C_{mem} + C_{ox}) \approx R_{mem} C_{ox} \tag{2.28}$$

$$\tau_2 = R_{mem} C_{mem} \tag{2.29}$$

-where τ_1 is extracted from the intersection of the linear segments at lower frequencies (i.e., low cut-off frequency), while τ_2 is obtained from the intersection of the linear segments at higher frequencies (i.e., high cut-off frequency). At lower frequencies, the oxide layer capacitance is higher than the membrane capacitance, therefore C_{mem} can be neglected (eq. 2.28), while at higher frequencies the membrane capacitance dominates and C_{ox} can be neglected (eq. 2.29). Here, τ_2 represents the relaxation time of the membrane. By extracting τ_1 and τ_2 from the transfer function curves and calculating C_{ox} of the gate oxide, equation 2.28 and 2.29 can be analytically solved [51].

Therefore, it is possible to complement the limitations of the potentiometric readout with an alternative transducer approach based on this impedimetric readout of ISFETs. Side parameters such as pH, temperature and ionic composition influence the potentiometric readout by resulting in a direct effect on V_{th}. On the other hand, the impedimetric readout is largely dependent on the ionic composition and it is less influenced by the surface-charge changes. It might be beneficial to overcome the limitations of the only potentiometric approach by a combination of both of the procedures [55-56].

2.4. Label-free electrical sensing using Si NWs technology

Over the last two decades, on account of the availability of new nanofabrication methods, new nano-scale ISFETs (nanoISFETs) have been developed. They are attractive as it is feasible to integrate a high-density of miniaturized sensor in a large array on a single chip with microfluidic structures for point-of-care (POC) applications [6, 47, 57-60]. Si NW FETs in the nanoISFET biosensor category, have shown advanced potential because of their commercial viability, ease in mass production, ability to tune their electrical properties and sensitivity reproducibly by controlling the dopant concentration and NW diameter [6, 30-32, 58].

The Si NW based biosensors were firstly introduced by Cui and co-workers in 2001 and are promising because of good electronic and mechanical properties and easy surface functionalization with chemical linkers [61-63]. The high-sensitivity of the Si NW FETs could be due to the high S/V ratio of Si NW, where the charge carrier density inside the NW is modulated by the surface-charges of the biomolecules bound to the Si NW surface. The commonly used, most simplified model to describe the charge sensitivity of a NW sensor is given as follows:

The conductance, G_0 of a cylindrical NW is given by-

$$G_0 = \frac{q\mu N_D \pi d^2}{4L_{NW}} \tag{2.30}$$

-where d is the diameter, L_{NW} is the length and N_D is the uniform doping density of the NW and μ is the mobility of charge carriers in the NW.

On binding of the biomolecules, there is change in the surface-charge density, $\Delta\sigma_s$ (charge per square centimetre), resulting in depletion or accumulation of an equal amount of charges inside the NW, $\Delta Q = \pi d \Delta\sigma_s$ (per unit length). Thus the sensitivity, S, of the NW sensor is given by [38]-

$$S = \frac{G - G_0}{G_0} = \frac{\Delta G}{G_0} = \frac{4\Delta\sigma_s}{qdN_D} \tag{2.31}$$

From equation 2.31, it can be seen that the sensitivity of a NW sensor is inversely proportional to its diameter. A lower doping level is thereby indicating a higher sensitivity of NW FETs (with finite d) compared to planar FETs of comparable area (with d approaching infinity). In general, a low NW doping is beneficial for biosensing, as the sensitivity is expected to increase with decreasing dopant concentration as the charge carrier Debye length in the Si NW increases with minimized charge screening [10, 64-65]. Although equation 2.31 is often used to design and interpret experiments, it has strong limitations for a general description of devices used in a liquid environment as a biosensor. The equation only discusses a scaling effect of the Si sensor without including the influence of the fluidic environment on the performance of NW ISFETs. In addition it doesn't account for the effect of electrostatic Debye screening of

biomolecules due to other ions in the solution. Furthermore, it doesn't differentiate between accumulation- and depletion-mode of NW operation [66].

Different types of Si NW based biosensors were reported so far for the detection of various biomolecules such as enzymes, nucleic acids, proteins, cells, viruses, metal ions and the mapping of neural circuits [6, 10, 45, 47]. Here, single crystalline Si NWs are preferred in comparison to polysilicon NWs, as they have higher conductivity and thus larger transconductance in response to a given field [58, 67]. Considering that the sensitivity of NW biosensors is inversely related to NW width (equation 2.31), low dimensional NWs can exhibit ultrahigh sensitivity, while long length of NWs enables multi-copy detection (thus enhanced signal) [9, 64-65, 67]. Additionally, thinner wires may offer reduced detection times due to the improvement in analyte diffusion kinetics, as the Si NW needs less molecules to generate a markable change [4, 58].

Application	Examples	Ref.
Cell signal detection	• Kinked Si NW FET for recording of intracellular signals from cardiomyocytes.	16, 68-72
	• Si NW transistor arrays for sensitive detection, stimulation and inhibition of neuronal signal propagation.	48, 73
Protein detection	• Si NW FETs for multiplexed, label-free immunodetection of three cancer biomarkers (carcinoembryonic antigen, PSA and alphafetoprotein).	74-79
	• Si NW devices for detection of cytokines such as – tumor necrosis-factor-alpha (TNF-α) and interleukin-6.	43, 80-81
DNA detection	• Local electrical potential detection of DNA using nanowire-nanopore sensors.	82-83
Organ detection/ interface	• Electrical recording and optical registration of flexible Si NW devices to heart surfaces.	84
Virus detection	• Electrical and optical measurements using fluorescently labelled influenza A.	85
pH sensor/chemical	• Electronic devices and sensors based on Si nanomembranes and nanoribbons for sensing pH and skin mounted monitors of electrophysiology.	5, 32, 86-87

Table 2.1 Examples of Si NW FET-based sensors for chemicals and biomolecules reported in the literature

On the other hand, it becomes important to know the signal-to-noise ratio (SNR) of the sensor when smallest changes in current need to be measured to analyze the detection limit of the sensor. The SNR is defined by, $SNR\,\alpha\frac{\Delta Q}{\sqrt{A}}$, where ΔQ is the total change in charge bound to the device surface and A is the device surface area. From this equation, if ΔQ (e.g., binding of a wide concentration range of analyte) is comparable to A, then the SNR is higher for devices with larger surface area. Conversely, if ΔQ is constant (e.g., single molecule binding), the SNR is higher for devices with smaller area. In conventional biomolecule detection methods, the analyte concentration should be determined. Since the probability of analyte binding increases linearly with the surface area available, nanoribbons/nanoplates are preferred to ascertain the analyte concentration. However, when single molecule detection is to be

studied, single molecule binding on a small nanowire is preferred, where the gate length is known as the prevailing factor (the smaller the gate length the higher the sensitivity) [58, 88]. Thus, the detection limit of the sensor depends on device noise and also on the system characteristics such as the rate of analyte diffusion to the surface and the affinity of the analyte-receptor interaction. These factors determine the lowest concentration of analyte that can be extracted from the device response. Moreover, multiple NW FETs are preferred over single NW FETs in order to increase the overall SNR, while device multiplexing (multiple FETs of the same type) is important to collect statistically meaningful information on each analyte. In addition receptor multiplexing is useful for simultaneous detection of multiple analytes [32, 89-93]. A list of further examples of Si NW based sensors for chemicals and biomolecules is given in Table 2.1. From these examples it is apparent that Si NW based sensors have taken the centre-stage for real-time detection of a wide range of chemicals and biomolecules [9, 29, 67, 94].

2.4.1. Fabrication methods for Si NW devices

The fabrication of Si NW FETs can be done by both "bottom-up" and "top-down" approaches and the recent attempts in these nanofabrication methods were concisely summarized [95]. The bottom-up approach for Si NWs fabrication starts from individual atoms aggregating into molecules and then they are assembled further to form nanostructures [6, 96]. The bottom-up approaches used for the growth of Si NWs include methods such as vapour-liquid-solid or solid-liquid-solid, chemical vapour deposition (CVD), etc. These bottom-up processes require high operating temperature, specialized equipment and particular operation conditions to produce high-quality Si NWs with diameters down to few nano-meters [97-100]. Nevertheless, controlled growth of Si NWs by bottom-up approaches remains impracticable for deployments on large scale and high-throughput fabrication. These bottom-up methods are most attractive for fundamental studies, as they provide the opportunity to control the growth mechanism by controlling several parameters during the growth process. For instance, it is feasible to do *in situ* doping of Si NWs by using precursor gas mixtures in order to tune the electrical properties of the Si NWs [61]. As-grown Si NWs require a substrate transfer process by means of physical, chemical or mechanical methods of Si NWs transfer from the growth substrate onto an arbitrary substrate, in order to be deployed as a transistor device. For instance, the transfer processes may be the Langmuir-Blodgett technique, blown–bubble, microfluidic flow, contact printing alignment (e.g., PDMS transfer), or dielectrophoresis techniques [6, 28]. In spite of that, intrinsic limitations of these bottom-up processes are including device integration challenges and low reproducibility that render these methods less favourable for mass production of commercial sensing devices. Those issues intrinsic to "bottom-up" approaches can be mitigated to some extent by combining them with classical "top-down" approaches, where device-to-device reproducibility can be achieved using conventional lithography and well-controlled wafer etching methods [13, 67, 101-105].

In contrast to this, in a "top-down" approach planar substrates such as SOI wafers are micro-/nano-patterned using state-of-the-art industry-scale fabrication methods

such as UV and deep-ultraviolet lithography, electron-beam lithography (EBL), focussed ion beam (FIB) etching, atomic force microscope (AFM) nanolithography, nanostencil lithography, etc. [4, 96, 101, 106]. These methods are generally combined with dry etching methods such as reactive ion etching (RIE) or wet etching methods such as wet anisotropic etching using TMAH to realize nanometre feature sizes. Nano-patterning techniques such as EBL and FIB are less favourable for industry applications, since they are very expensive and time-consuming, but very useful for the basic research community due to their flexibility of operation. More recently, NIL for the nano-patterning of planar substrates has gained impetus, since this process is cost-effective, easy to operate, highly reproducible at wafer-scale and much faster in comparison to other techniques. Thermal- or UV-assisted NIL provides a very nascent "top-down" approach for the fabrication of Si NW FETs [32, 107-108]. A thermal nanoimprint method in combination with anisotropic wet-etching was demonstrated to produce high-quality Si NW FETs on wafer-scale with identical surface and electrical sensing characteristics in liquids, deployed as chemical sensors [4, 32].

The Si NW FET devices reported in this thesis were fabricated using a high-throughput, "top-down" process involving a combination of NIL, wet chemical etching and ion implantation. The general principles of the most important processes involved in the fabrication process for the realization of highly reproducible Si NW sensors on wafer-scale are described in the following subsections. The modification and adaptation of these methods towards fabrication of the devices used in this thesis are detailed in chapter 3.

Nanoimprint lithography

NIL is a process in which the negative image of a stamp/mould is transferred using a temperature or light-sensitive resist spin-coated on a substrate and thus the process is called thermal (T-NIL) or ultraviolet (UV-NIL), respectively [107]. T-NIL was firstly introduced in 1995 by Chou and co-workers. They realized sub-25 nm structures thereby overcoming the limitations of the conventional lithography methods [109-110]. Using T-NIL, it is feasible to process nanostructures in a parallel, high-throughput and low fabrication cost process. Though T-NIL has proven to be very successful in replicating periodic nanostructures, it has several limitations in simultaneous production of combined micro- and nano-structures, which is a necessity in our current fabrication process. Therefore some other variants of NIL such as UV-NIL, soft UV-NIL and combined nanoimprint and photolithography process were introduced [111]. Combined nanoimprint and photolithography exploit the advantages of both methods, while compensating each other's limitations. Thus it is easily possible to pattern the nano- and micro-structures, respectively.

In this thesis work, T-NIL was employed to transfer the nanowire structures onto SOI substrates using an EBL-patterned SiO_2/Si hard stamp. The steps involved in the T-NIL process are outlined in figure 2.6. The SiO_2/Si stamp is aligned with a polymer resist coated substrate and then heated above the glass transition temperature (T_g) of the polymer (figure 2.6 A (i),(ii) and B).

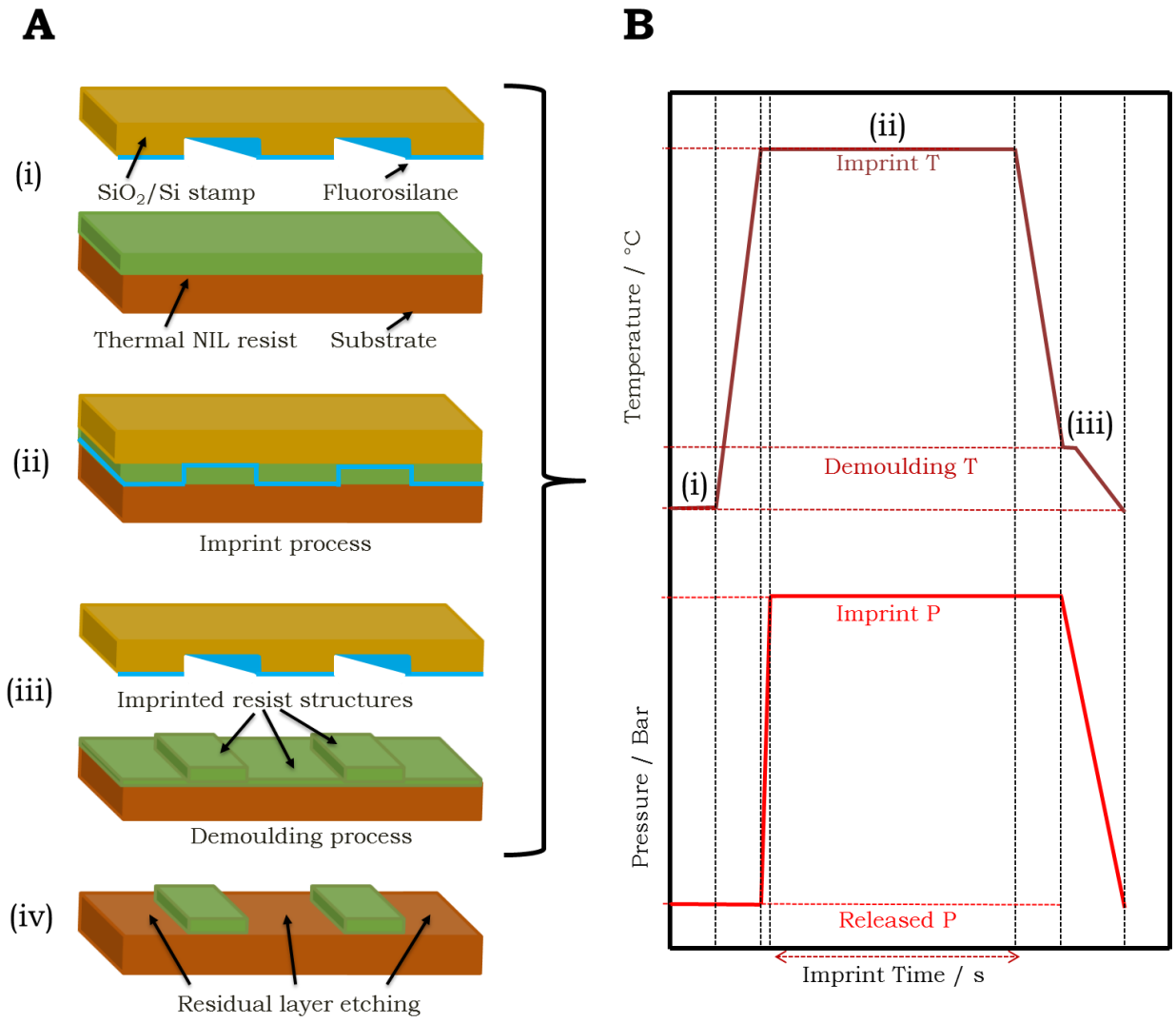

Figure 2.6 Schematic representation of the different steps involved in a T-NIL process: (A) (i) NIL stamp coated with an anti-sticking layer of fluorosilane and thermal resist coated substrate; (ii) Thermal imprint process in which the resist coated substrate is aligned with the stamp and the temperature is increased followed by applying pressure for a certain time; (iii) Demoulding process in which the stamp is separated from the wafer; (iv) Etching of the residual layer of the resist using RIE process; and (B) Temperature and pressure profile of the different steps (i), (ii) and (iii) in the T-NIL process.

In a T-NIL process, a special temperature-sensitive polymer resist is used. Above its T_g, it is in a liquid flow state and can therefore be deformed irreversibly by the structures of the stamp. The imprint process is then carried out by pressing the resist-coated substrate (heated above the T_g) against the stamp with an optimized pressure as it is illustrated in figure 2.6 A (ii) and B. The imprint process is carried out for a certain duration depending on the resist viscosity and its thickness. The duration also depends on the structure pattern and depth of the stamp. Therefore, the T-NIL process needs an initial optimization for different substrates/stamps. To prevent any adhesion problem between the resist and the stamp, the stamp is coated with an anti-sticking

layer such as fluorosilane (Trichloro(1H,1H,2H,2H-perfluorooctyl) silane) prior to the NIL process [111]. After the imprint process, the temperature is decreased below the T_g resulting in hardening of the polymer resist. The pressure is released at a certain temperature called demoulding temperature (figure 2.6 A (iii) and B) and thereafter, the wafer is carefully separated from the stamp. Following the demoulding process, the wafer has a negative pattern of the stamp and is covered with different resist thicknesses, with higher thicknesses at the trench areas of the stamp (figure 2.6 A (iii)). Subsequently the residual resist layer is etched by a RIE process to transfer the imprinted pattern further to the underlying substrate as it is illustrated in figure 2.6 A (iv).

In a nanoimprint process, protrusion features on the stamp deform the polymer physically and displace it. Imprint stamp complexity arising from inhomogeneous distribution of the nano- and micro- structures also called “imprint proximity effect” might lead to an incomplete pattern transfer leading to NIL defects or even failures. Nanoimprint relies on displacement of the polymer layer by the structures in the stamp. At a particular pressure and viscosity of the polymer, the rate of displacement is different for the micro- and nano-structures leading to such NIL defects. For example, dense array of structures will displace more polymer than an isolated structure. Depending on the distance of this isolated structure from the array, the polymer might not be fully displaced within a particular time frame leading to imprint defects. Similarly, the polymer thickness and filling time requirements are different for small and big cavities. Since the viscosity decreases with an increase in temperature, it is faster to imprint big cavities at high temperature. This proximity effect leads to structural defects and variations in the residual layer thicknesses over the substrate, corresponding to different size structures on the stamp. The main requirement for a good imprint process is a uniform distribution of the structures on the stamp. Additionally, the polymer resist should have properties such as low T_g to imprint at low temperature, low viscosity for easy flow into the mould cavities and low shrinkage after the imprint process. Furthermore, the resist should have high resistance to RIE in order to serve as a mask for the subsequent structure transfer *via* RIE.

After the imprint process the residual layer is removed using a RIE process typically under an oxygen plasma. This process is very unselective as it etches both the residual layer and the resist structures. The difference in thickness of the resist structures and the residual layer should be enough and the etching process needs to be optimized in order to not completely etch away the resist structures. If the residual layer thickness has large variations, it might lead to inhomogeneous etching in different regions over the substrate and some parts of the structures might be over-etched leading to defects in the finally transferred pattern.

Anisotropic etching of silicon

Generally dry etching processes such as RIE, degrade the transistor device performance on account of the surface damage caused by ions. Therefore wet-etching processes using TMAH are preferred to define the transistor structures. In this thesis

work, anisotropic wet-etching using TMAH was used to slowly degrade the bulk Si layer in order to define the source and drain contact lines and the NWs for the Si NW FETs in a single step [112-113]. The etching rate of different crystal planes in Si with alkaline solutions such as TMAH was found to be associated with their activation energies. The crystal surfaces with higher activation energies showed slower etching, while with lower activation energies showed faster etching [114]. This plane-dependent etching behaviour can be explained from an electrochemical model, according to which energy levels of back-bond surface states depend on the crystal orientation. Consequently, two Si back-bonds must be broken to etch the <100> and <110> surfaces, while three are broken for the <111> surface [114-115]. Thus, the activation energy of the Arrhenius relationship ($R \sim R_o e^{-E/kT}$) follows the trend of $E_{(110)} < E_{(100)} < E_{(111)}$. This can be correlated with the etching rates of the different planes of Si in alkaline solutions such as TMAH and KOH.

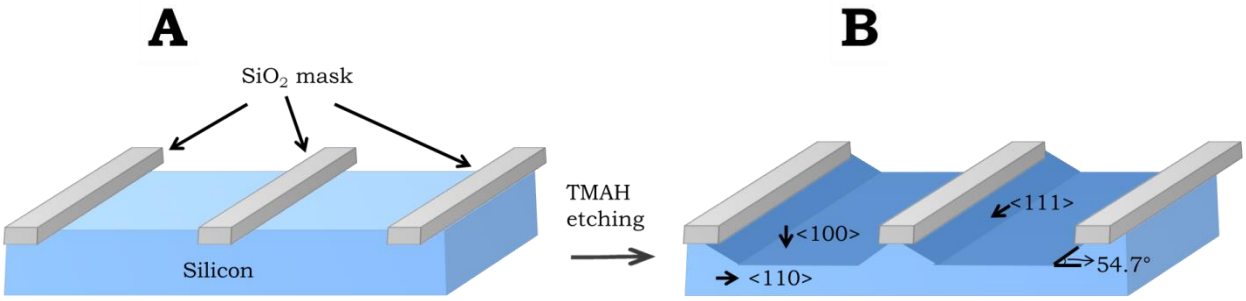

Figure 2.7 Schematic representation for anisotropic etching of Si with a SiO_2 hard mask: (A) A patterned SiO_2/Si wafer before TMAH etching; and (B) A SiO_2/Si wafer after TMAH etching.

The TMAH solution etches the Si anisotropically with Si <111> plane etched about 100 times slower than all the other planes. For a Si wafer having a <100> plane orientation, a thin layer of dry thermal SiO_2 or CVD silicon nitride is used as a hard mask to anistropically etch the underlying Si. By the use of TMAH etching of a SOI wafer structured with a SiO_2 hard mask, Si NWs with a trapezoidal cross-section can be obtained [32, 116]. Figure 2.7 shows the schematic of the profile of a Si wafer before (A) and after (B) the TMAH etching process, where a thin layer of SiO_2 acts as a hard mask. It can be seen that the etching rate of Si is high in the <100> plane. When using a SOI wafer owing to the presence of an etch stop of the buried oxide layer, a very short etching time is required.

With this method smooth, extremely low noise, trapezoidal shaped Si NW structures with Si <111> sidewalls at an angle of 54.7° with the <100> top and bottom surfaces can be obtained [90, 117]. The width of a Si NW in lateral direction is linearly proportional to the etching time with the lateral etching rate of 2-3 nm/minute. Additionally, the etching can be controlled by adjusting the etching temperature and using additives such as isopropanol resulting in a very low (~ 0.5 nm $second^{-1}$) etching rate near the room temperature (35 °C) [112, 118].

Ion implantation

The intrinsic conductivity of the Si device layer of commercial SOI wafers is very low, with a resistivity in the order of 8-12 Ω.cm. Therefore, in order to enhance the performance of the Si NW FETs developed in this thesis, the serial resistance of the contact lines was reduced by doping them with boron. The Si NWs were left undoped to retain their carrier mobility high [10, 64-65].

In order to carry out the doping process, ion implantation was chosen as it has several advantages in comparison to diffusion processes. Ion implantation in contrast to a diffusion process allows a precise control of the ion distribution and dose of the dopants in the device layer with a high reproducibility and can be realized at low processing temperatures. Ion implantation is a process in which the energetic ions penetrate the surface of the wafer and then undergo a series of collisions with the atoms in the target. The penetration depth of the dopants depends on the kinetic energy of the ions, which can be controlled very accurately. Here the absolute concentration of the dopants can be adjusted by varying the implantation dose. Thus, the ion implantation doping process is controlled by the ion implantation energy, dose and thickness of the SiO_2/resist passivation layer on the NW region.

Additional care must be taken while implanting ions in order to prevent the ion channelling effect. When the incident ions align with the major crystallographic direction, they are channelled between the rows in the crystal leading to significantly larger projection ranges into the crystalline target. Consequently, the ion channelling effect is very critical in particular for low-energy implants and heavy ions. The ion channelling effect can be prevented by creating a blocking amorphous layer in the device surface or by mis-orientation of the wafer and also by creating a damaged layer in the device surface. In most of the implant machines the wafers are tilted by 7° and twisted by 22° to prevent this ion channelling effect.

Nonetheless, one major disadvantage of the ion implantation process is the damage of the crystal structure as the implanted dopants reside on the interstitial sites. This impairs the electrical properties of the semiconductor. So, in order to repair the crystal damage and to activate the dopants, a thermal activation step is necessary after the ion implantation step.

2.4.2. Limitations of the Si NW FET sensors

From theoretical simulations it is well known that the sensitivity of an ISFET sensor depends on a number of factors such as sensor geometry, coated materials, gate oxide thickness, doping density of the sensor, analyte and fluidic environment characteristics [119]. Despite of the popularity of Si NW ISFETs biosensors there are certain issues - such as low frequency noise (LFN) and current stress, reproducibility, multiplexing, working in physiological solutions, low cost and portability, etc. that need to be resolved in order to commercialize these sensors [46]. Some of these shortcomings are discussed in detail in the following subsections.

Downscaling of Si NW FETs

As the dimensions of Si NW FETs are decreased, issues such as the increase of LFN and current stress come into play leading to false positive readings. Increase in LFN is on account of the decrease in the number of charge carriers, thereby leading to an increase in surface contributions to the total electrical noise [46, 120]. In addition, the current stress is related to the signal drift without any change on the sensing membrane [46]. The above two issues are related to the potential, which is applied at the gate. At low gate-source voltage or below the threshold voltage the voltage fluctuation of the device increases, but the stress can be repressed [46, 62]. LFN is a major limiting factor and therefore various approaches such as quality of the device surfaces, using frequency domain detection and optimizing the operating regime of the devices were tried out [120]. The working regime and strength of the gating effect caused by molecules at the surface of the NW FET sensors are decided by the relative magnitude between the carrier screening length inside the nanowire (λ_{Si}) and the nanowire radius (R). When the concentration of charge carriers in the NW is high, the carrier screening length is much smaller than the NW radius ($\lambda_{Si} << R$) and the NW FET works in the linear regime. Thus, the conductance (G) varies linearly with the gate-source voltage. On the other hand, when the charge carrier concentration is low, the carrier screening length is much larger than the NW radius (where $\lambda_{Si} >> R$) and the NW FET works in the depletion (subthreshold) regime. In this case, G varies exponentially with the gate-source voltage. In the linear regime, the field-effect of the positive/negative charges at the surface, induces a bending of the bands and the depletion/enhancement of the carriers inside the NW within a region of depth ~ λ_{Si}. Whereas, in the subthreshold (depletion) regime, the screening length of the carriers in the NWs is long ($\lambda_{Si} >> R$) and whole of the NW is gated by the field-effect of the surface-charges. Thus, the high S/V ratio of the NW can be fully utilized [10, 64, 121-124].

The Debye screening length of carriers inside the Si NW is given as-

$$\lambda_{Si} = \sqrt{\left(\frac{\epsilon_{Si}\epsilon_0 \, kT}{pe^2}\right)} \tag{2.32}$$

-where p is the concentration of holes (majority charge carriers) within Si (number of ions $/m^3$), ε_{Si} is the dielectric constant of Si, ε_0 is the vacuum permittivity.

Thus, the subthreshold regime of operation is favourable as the drain-source current varies exponentially with the change in the gate-source voltage. However, in this case the SNR ratio is generally lower than in the linear regime. On the other hand in the linear regime, the conductance response of the Si NW varies linearly with the gate-source voltage, yet there is a screening of the charge carriers inside the NW [10].

Solid-Liquid interface and different readout methods

Despite the fact that NW sensors are appealing, they have several fundamental limitations that make them incapable of sensing molecules in complex, physiological

solutions such as whole blood, plasma, serum, saliva and urine [75, 125]. Non-specific binding of analytes readily degrades the minute active surface of such devices minimizing the probability of capture of the analyte of interest and leading to false-positive results [63, 75, 125]. In order to avoid this non-specific adsorption, various blocking agents such as bovine serum albumin, ethylene glycol and OH terminated, self-assembled monolayers were used to block the surfaces of sensing devices.

Further, the sensing with Si NW ISFETs is limited by the charge screening effects similar to the ISFET devices as discussed in the previous section (Debye length, λ_D) [76]. Thus, low concentration buffers are required for label-free testing of analytes based on their charge [76, 125]. There are several other methods reported to overcome this charge screening effect, for instance by using smaller receptor molecules such as aptamers, glycans, fragmented antibodies, etc. [57, 89, 126-127]. In other approaches the surface chemistry is tuned by lowering the antibody surface coverage or a biomolecule permeable membrane is used, so that the analyte-receptor binding can take place within the Debye length in physiological solutions [128-130]. Other artificially synthesized polymers such as peptide nucleotide acids of neutral charge are promising as receptors on the Si NW surfaces in order to carry out sensitive and specific detection of DNA/RNA [131]. Though these studies have shown potential to achieve biomolecule detection in physiological solutions, still there are limitations on preparation of specific receptors for a large number of biomolecules.

Other than the charge based sensing, impedance methods have also been developed in order to study the change in impedance on binding of biological analytes. This impedance method has been reported for a wide range of applications ranging from whole human body measurements to those conducted at the level of DNA [51-52, 132]. Even so, nanoscale advantages lie in the charge-based sensing methods only where the biomolecule charges on binding cause a change in the electrostatic potential at the outer surface of the gate dielectric [133].

Gate material and sensor configuration

For stable sensor operation, the surface of fabricated Si NWs is normally coated with a thin layer of gate oxide (e.g., 8-10 nm of SiO_2), which should be chemically inert to react with any analyte [82, 98]. However, SiO_2 as a traditional top-gate material has many drawbacks such as low pH buffer capacity, susceptibility to leakage current due to ion incorporation in the presence of fluids, in comparison to other high-k dielectric materials such as aluminium oxide, hafnium oxide and tantalum oxide [10, 58]. By these effects and also by minute etching of the SiO_2 surface in salt solutions this surface is causing a severe long term drift of the Si NW devices. Other gate materials with high-k value mainly deposited by atomic layer deposition allow a reduction in leakage current while offering a high gate oxide capacitance. Using these materials a greater physical thickness of the gate dielectric layer can be fabricated without compromising the sensitivity to the surface-charges.

In a conventional Si NW FET fabricated from an SOI substrate the Si NWs are still attached to the substrate. Therefore the transport of analytes to the Si NW surface is

limited resulting in a decrease of sensitivity and an increase in detection time. This limitation can be overcome by suspending the Si NWs, which increases the sensing area and thus also increases the sensitivity and decreases the response time [134]. However, with this the mechanical robustness of the sensors is also decreased.

Additionally, passivation of the sensor chip surface and in particular of the contact lines is required to minimize the leakage current and to realize an isolation from the external environment. Several methods based on the usage of SiO_2 grown by different CVD procedures and SU-8 resist, are reported in the literature for passivation of the sensor surface [65, 135-136].

Surface modification

Several surface modification methods to achieve a covalent linkage of receptors at the surface of SiO_2 were reported. In these methods, silanization using different silane types such as 3-aminopropyltriethoxysilane (APTES), Glycidyloxypropyltrimethoxysilane (GPTES) are the most preferable methods [98]. This usually results in receptor immobilization over the entire chip surface unless precise immobilization techniques such as microspotting are deployed. Immobilization of the receptors on the entire chip results in binding of a large quantity of analyte in the surrounding surface of Si NWs and hence results in a decrease in detection sensitivity of the Si NWs devices. Recently Li and co-workers, reported a method to overcome this limitation by silanization of the Si NWs during a bottom-up growth process and thereby confining the binding of biomolecules only on the NW surface [137]. Moreover, other methods of surface functionalization such as electric-field alignment or localized nanoscale joule heating can enhance the nanowire sensing capability [131, 138].

Chapter 3 Realization of a Si NW FET sensor platform

Silicon ISFETs are presenting a very important platform technology for the development of electronic bioassays in recent years as discussed in the last chapter. The use of Si ISFETs for biosensor applications, however, face critical challenges in terms of sensitivity and reproducibility of the sensor characteristics required for the development of next-generation assays. A majority of novel bioassays require sensitivities down to a few molecules in serum or concentrated buffer as well as specificity towards a wider biomarker panel in order to correctly diagnose a disease. For such requirements, Si NW ISFETs have shown to demonstrate high sensitivities and are maybe a suitable option to realize sensor platforms with all the required sensor characteristics. What is also critically important is to fabricate such sensor platforms at wafer-scale with high-density of sensing-sites on the individual sensor chips with identical sensing properties. Towards this end, and as discussed briefly in the previous chapter, NIL was deployed as a powerful tool to fabricate the Si NW FETs developed in this thesis. In this chapter the complete process for the fabrication of our Si NW FETs by using NIL and anisotropic wet-etching is described. Further, the details of the surface functionalization and microfluidic integration of the Si NW sensor platform in order to deploy them for bio/chemical sensing assays are also given.

3.1. Top-down fabrication of Si NW FETs

The Si NW FETs used in this thesis work were fabricated using a combination of "top-down" methods such as NIL, UV lithography and dry and wet-etching processes. In this section a short introduction of the Si NW chip configuration and the NIL mould design is given. The complete fabrication process flow for the Si NW FETs on 4" SOI wafers is also described. Thereafter, results of the structural characterization of the NW FETs at different fabrication steps are described. Furthermore, in the last section problems that arise on combination of NIL, UV lithography and etching processes are discussed.

3.1.1. Prefabrication

The designed chip configuration of the Si NW FETs and the mould fabrication process are described in the following subsections.

Si NW FETs chip and NIL mould design

The layout of the Si NW FETs based sensor platform of 7 mm × 10 mm dimensions is illustrated in figure 3.1 inset. The Si NW FET chip layout was designed using a graphics program (Clewin version 3.1.11 developed by WieWeb software) before the fabrication. The snapshot of the arrangement of Si NW FETs chips on a 4" mask in the Clewin program is illustrated in figure 3.1. A total of 78 Si NW FET chips were arranged on a 4" mask. The transistors with 3 different NW dimensions (width by

length), which include 400 nm by 15 µm, 200 nm by 8 µm and 150 nm by 32 µm were positioned on the mask.

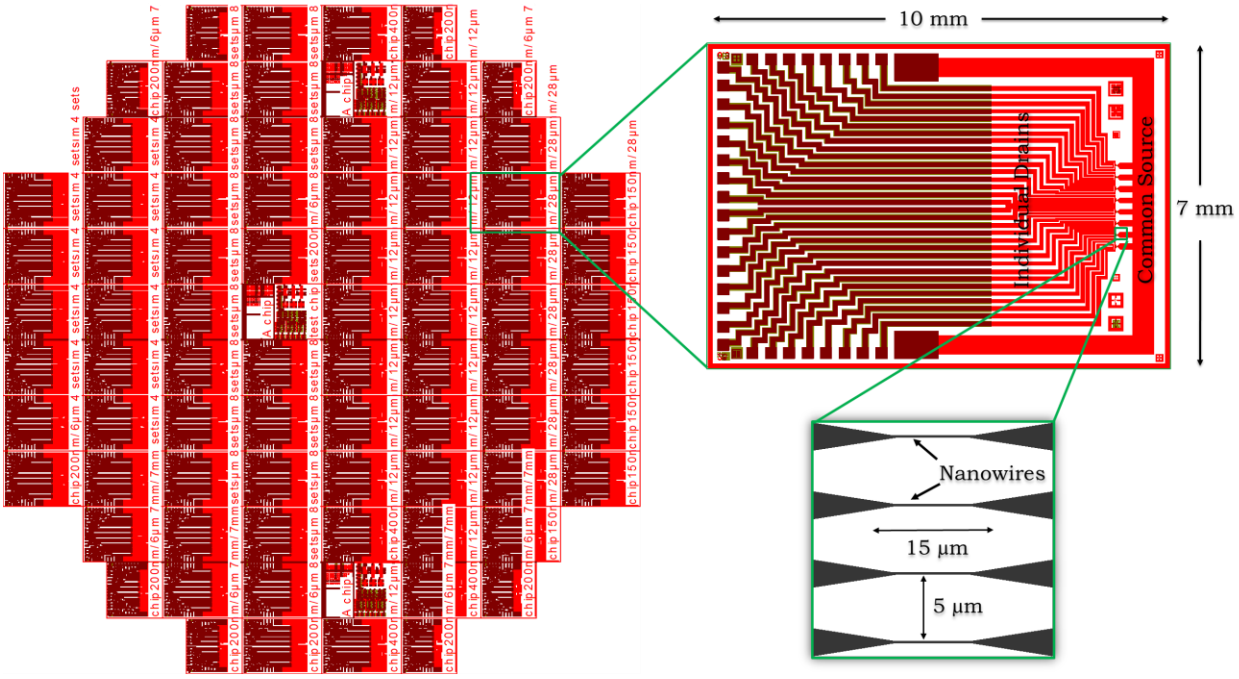

Figure 3.1 Layout of the Si NW FETs chips on a 4" mask in the Clewin program with a single Si NW FET chip (with dimensions 7 mm × 10 mm) shown in the inset.

A single Si NW FET chip consisted of 32 Si NWs arranged in 8 sets of 4 NWs (illustrated in figure 3.1 inset) with a common source and separated drain contacts. The 4 NWs in one set are separated by 5 microns in distance, as it is shown in figure 3.1 (inset right bottom). In order to allow site-specific immobilization of different receptors on different NW sets on a chip (without any overlap between the neighbouring sets), the NWs sets were separated by a distance of 250 microns. The reliability of the readout could then be improved by obtaining statistically meaningful output signal, where an averaged sensor signal from the 4 NWs (i.e., one set) on one position can be obtained. To deploy the chips in a dip-chip configuration as well as for an easy assembly of a fluidic channel, all the NWs were connected to a common source electrode in a special configuration, where the NW region (i.e., sensing region) was positioned closer to the edge of the chip. Further to allow multiplexing, the NWs were connected to individual drain electrodes to read out all the channels simultaneously. In addition to this, sensor characteristics of all the 32 NW channels were made identical as all the drain contact lines were designed to have the same values of the total capacitance (i.e., surface area in contact with the solution) and inline resistance. With our common source configuration, the drain contact lines are intricately designed to render an equal surface area. For doping concentration of the order of 10^{20} /cm^3 of boron ions, the resistivity of the p-type Si was of the order of 10^{-5} Ω.m [35].

Sheet resistance (R_s) = resistivity / thickness.

Thus, the sheet resistance for our 70 nm thick Si can be estimated with, $R_s = 10^{-5}$ Ω.m / 70×10^{-9} m = 143 Ω.

The sheet resistance was measured in Ohms per square; therefore the number of squares for the common source and the individual drain contacts on the sensor chip were calculated. The total number of unit squares for the source contact was 11 and thus, the sheet resistance of the source contact was, $R_S = 11\times143 \approx 1.6$ kΩ. Additionally for each drain contact line, the total number of unit squares = 50 and the sheet resistance of the drain contacts was then, $R_S = 50\times143 = 7.15$ kΩ.

For the capacitance estimation, the capacitance is generally given by the parallel plate capacitor model where-

$$C = \epsilon_o \epsilon_r \frac{A}{d} \tag{3.1}$$

-where $\varepsilon_0 = 8.8541\times10^{-12}$ Fm^{-1}, ε_r (i.e., SiO_2 dielectric constant) = 3.9, A (i.e., unit square area of the dielectric material) = 3×10^5 μm^2 for drain and 5×10^6 μm^2 for source and d (i.e., thickness of dielectric material (SiO_2) used as passivation layer) = 8 nm. Thus from equation 3.1, the capacitance for the drain and source contact lines is on the order of 1.3 nF (drain) and 22 nF (source), respectively.

NIL mould fabrication

After the design of the Si NW FET chip was finalized, the mould for NIL process was fabricated. A 6" SiO_2/Si wafer was patterned using EBL at the Institute of Microelectronics, Stuttgart, Germany*. The different steps in the mould production are illustrated in figure 3.2. The SiO_2/Si wafer was coated with Poly methyl methacrylate (PMMA) resist (i) and was structured by EBL (ii). After the resist development process, the pattern structure, which consists of trenches, was transferred into the resist (iii). In the next step, the exposed underlying SiO_2 was etched using a RIE process to have the trenches pattern in the SiO_2 layer. Finally, the resist leftovers on the SiO_2 structures were removed to have a smooth and contamination free SiO_2/Si mould (iv).

In figure 3.3 A, the layout of the structures of one Si NW FET chip on the SiO_2/Si mould is illustrated. The darker blue regions represent the etched areas of SiO_2 (trenches in the mould), while the lighter grey regions represent SiO_2 (protrusions in the mould). After the imprint process, a negative pattern was transferred to the substrate. Therefore, the etched areas in the mould are imprinted as features that protrude out on the substrate such as NWs and contact lines (NIL details given in section 2.4.1 of chapter 2).

* The 6" SiO_2/Si mould was fabricated using EBL and RIE at the clean room facilities of the Institute of Microelectronics, Stuttgart, Germany. They used the so-called variable shape beam EBL tool. The profile of the structure pattern was kept between 80-90° and the pattern depth tolerance was (tolerances across the wafer - SiO_2 thickness variation) ≈ ± 20 nm.

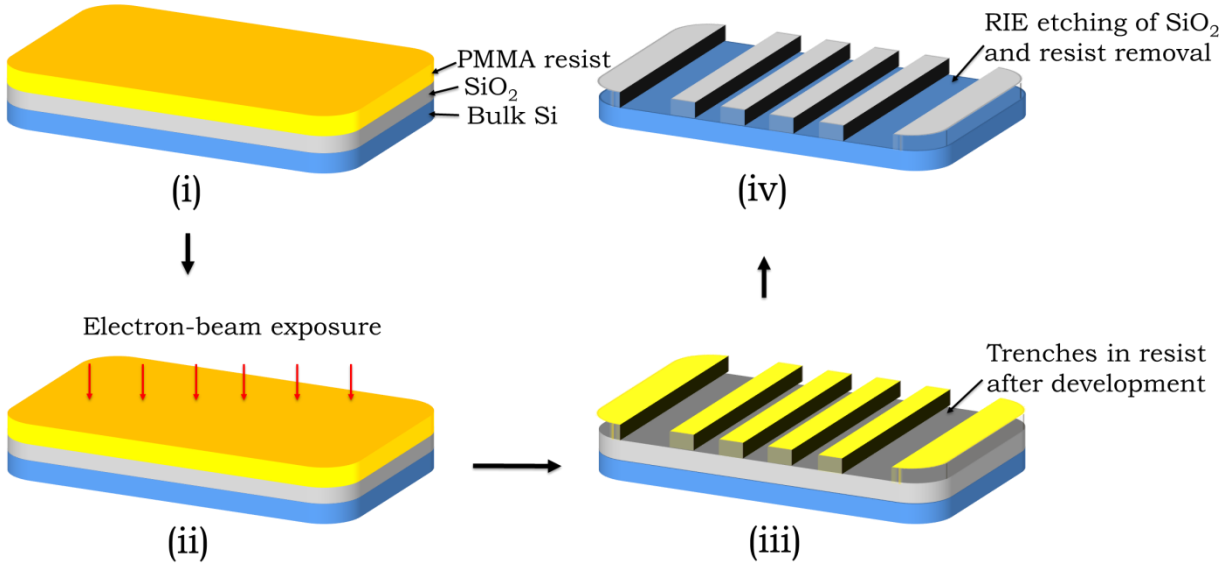

Figure 3.2 Schematic of the NIL mould fabrication on a 6" SiO_2/Si wafer: (i) PMMA resist coated on a SiO_2/Si wafer; (ii) Exposure of the resist coated wafer with electron-beam; (iii) Development of the resist that results in trenches in the resist; and (iv) RIE of the exposed SiO_2 layer and removal of the leftover resist to have the final SiO_2/Si mould.

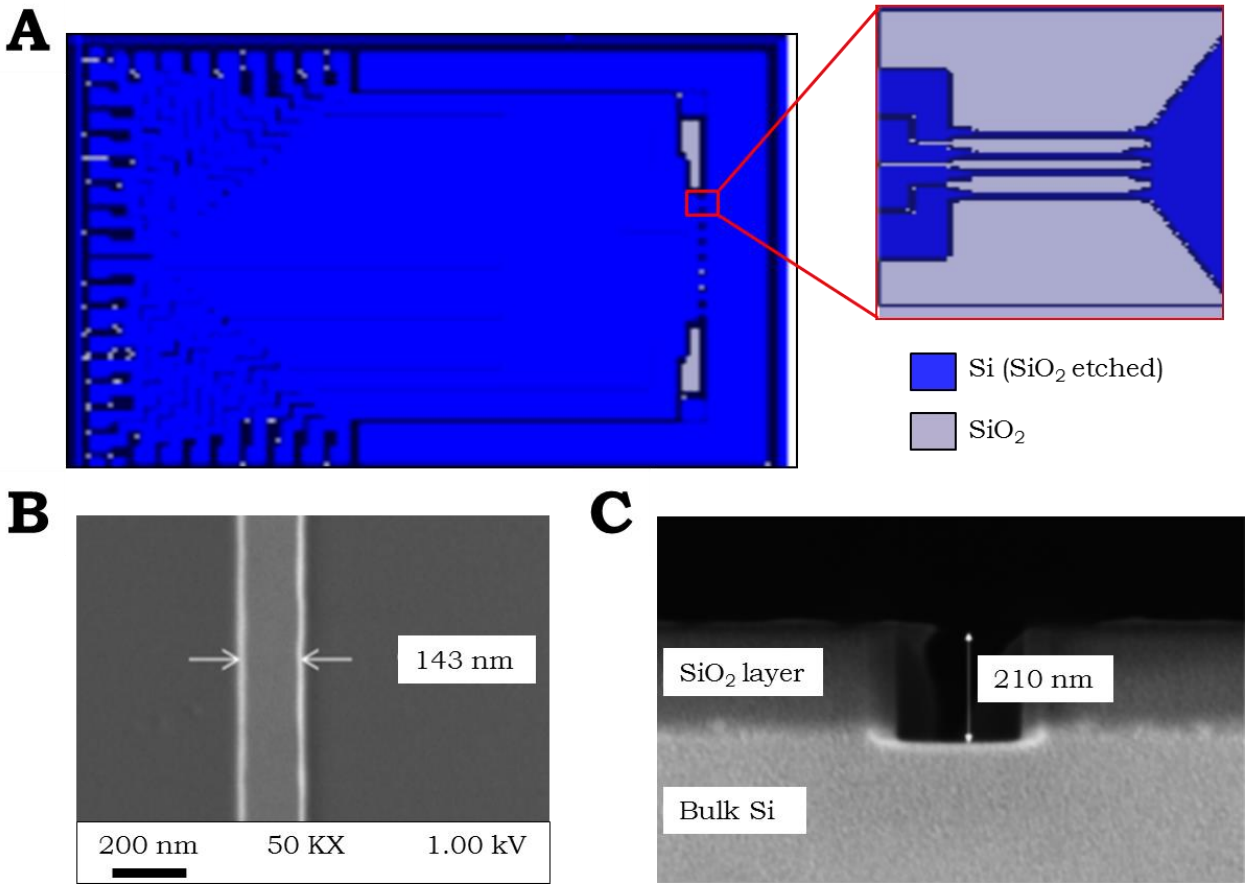

Figure 3.3 (A) Layout of the Si NW FETs structures on the SiO_2/Si mould; SEM images showing (B) Width of a NW structure; and (C) Depth profile in the fabricated SiO_2/Si mould.

As shown in the SEM image in figure 3.3 C, the height profile of the structures in the fabricated SiO_2/Si mould is nearly vertical with a depth of the order of 210 nm and a width of the smallest NW in the order of 143 nm (figure 3.3 B). The aspect ratio (height to width) of the pattern structures in the SiO_2/Si mould was kept low (4:3 approx.) to avoid the pattern fracture after the demoulding process (due to high shear stress at the vertical interface between the polymer resist and the mould) [139-140].

3.1.2. Si NW FETs fabrication process

The mould was cleaned using the standard Radio Corporation of America (RCA**) procedure and the surface was activated by an O_2 plasma treatment. This was followed by silanization of the mould with a fluorosilane in a glove box under inert atmosphere. The water contact angle measurements (= 110° ± 10°) showed an uniform coating of the silane layer. The silane layer over the mould was very stable and prevented sticking of the resist onto the mould to allow many consecutive imprint processes. It also remained stable during the standard cleaning procedures in acetone and ultrasonification [112].

For the fabrication of the Si NW FETs, 8 inch *prime* quality SOI wafers (SOI-Prime-8-880/1450Å) were obtained from SOITEC, France. The wafers were then cut into 4" wafers at Catholic University of Louvain, Belgium and cleaned with the standard RCA protocol. Before starting the processing, the thickness of the different layers on the SOI wafers was measured using a SEN850 ellipsometer from SENTECH GmbH, Berlin. The measured thickness of the top Si was 87.3 nm. The buried oxide (BOX) measured 145.2 nm (table 3.1), which was in close agreement with the values given in the data sheet (Si = 88 ± 12 nm, BOX = 145 ± 6 nm, bulk Si = 725 ± 15 μm). The wafers were with <100> crystal orientation with low boron (p-type) doping with resistivity values ranging from 8 to 22 Ω.cm. The SOI wafers are generally preferred for transistor fabrication as the transistors are built on the top Si layer thereby resulting in a decrease in the leakage current (as transistor area is separated from the bulk Si) and lower working voltages. On SOI wafers, the transistors have faster signal switching capability and they can be arranged more compactly on the chips with minimized "latch up" problems.

The first step in the processing was to grow a thin layer of thermal oxide SiO_2, by a dry thermal oxidation of the top Si layer. This results in thinning down of the Si layer to a thickness of 67 nm with the top oxide thickness of 45 nm. The thicknesses of Si

** RCA cleaning is a standard set of Si wafer cleaning steps used in the semiconductor manufacturing industry (https://en.wikipedia.org/wiki/RCA_clean). Here 3 chemical processes are carried out in a sequence, which includes the removal of organic contaminants, oxide layer and ionic contaminants. For organic contaminants and particles removal (called as standard clean-1), the wafers are dipped in a mixture of H_2O:NH_4OH:H_2O_2 in the ratio of 5:1:1 at 75 °C for 10 minutes. Thereafter, the oxide layer is removed by dipping the wafers in 1% HF at 25 °C for 15 seconds. Further in the next step, wafers are dipped in a mixture of H_2O:HCl:H_2O_2 (6:1:1) at 75 °C for 10 minutes to remove the metallic contaminants (called as standard clean-2).

and SiO_2 were confirmed by ellipsometry measurements shown in table 3.1 and the details are given in the subsection 3.1.3 of this chapter. Throughout the practical work in this thesis, a thorough process optimization was carried out for each step of thermal oxidation, NIL, RIE, wet anisotropic etching and UV lithography to obtain the required pattern structure of the Si NW FETs.

The different steps in the fabrication process are illustrated in figure 3.5. A SOI wafer after the thermal oxidation process shown in figure 3.5 (i) was spin-coated with nanoimprint thermal resist MR9030 (purchased from Micro Resist Technology GmbH) in order to get a 700 nm thick layer. Then the wafer was baked for 2 minutes at 100 °C to evaporate the solvent and to densify the resist after spin-coating. The imprint process (NIL Eitre 6, release version 3.2.6 from OBDUCAT, Sweden) was carried out by pressing the resist coated wafer against the stamp at 95 °C for 900 seconds at 50 bar pressure and followed by de-moulding at 40 °C. This step required initial optimization for the particular NW chip design used in order to find the optimum thermal resist type and thickness required. The imprint pressure and temperature also needed to be optimized.

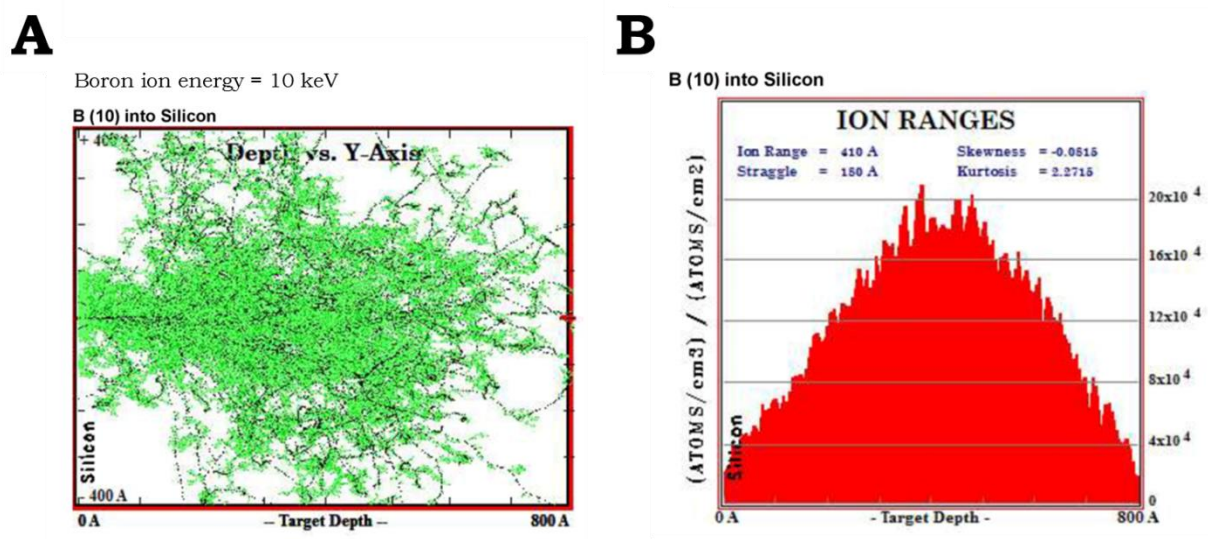

Figure 3.4 Plots showing boron (A) Implantation energy obtained from the SRIM simulation software; and (B) Dose obtained from the TRIM simulation software. Based on these simulations the energy and dose were fixed for the service implantation.

A mirror pattern of the mould, imprinted into the resist layer as shown in figure 3.5 (ii), was used as a mask to structure the 45 nm thick SiO_2 layer underneath in the following step. The residual layer of the imprinted resist was dry etched using a RIE process in 20 sccm O_2 at 100 W power and 2 Pa pressure for 240 seconds (figure 3.5 (iii)). This step was very critical as the whole wafer surface was exposed to the oxygen plasma, which results in etching of the resist over the whole wafer. Here care must be taken not to over-etch the structures, thereby damaging the imprinted structures.

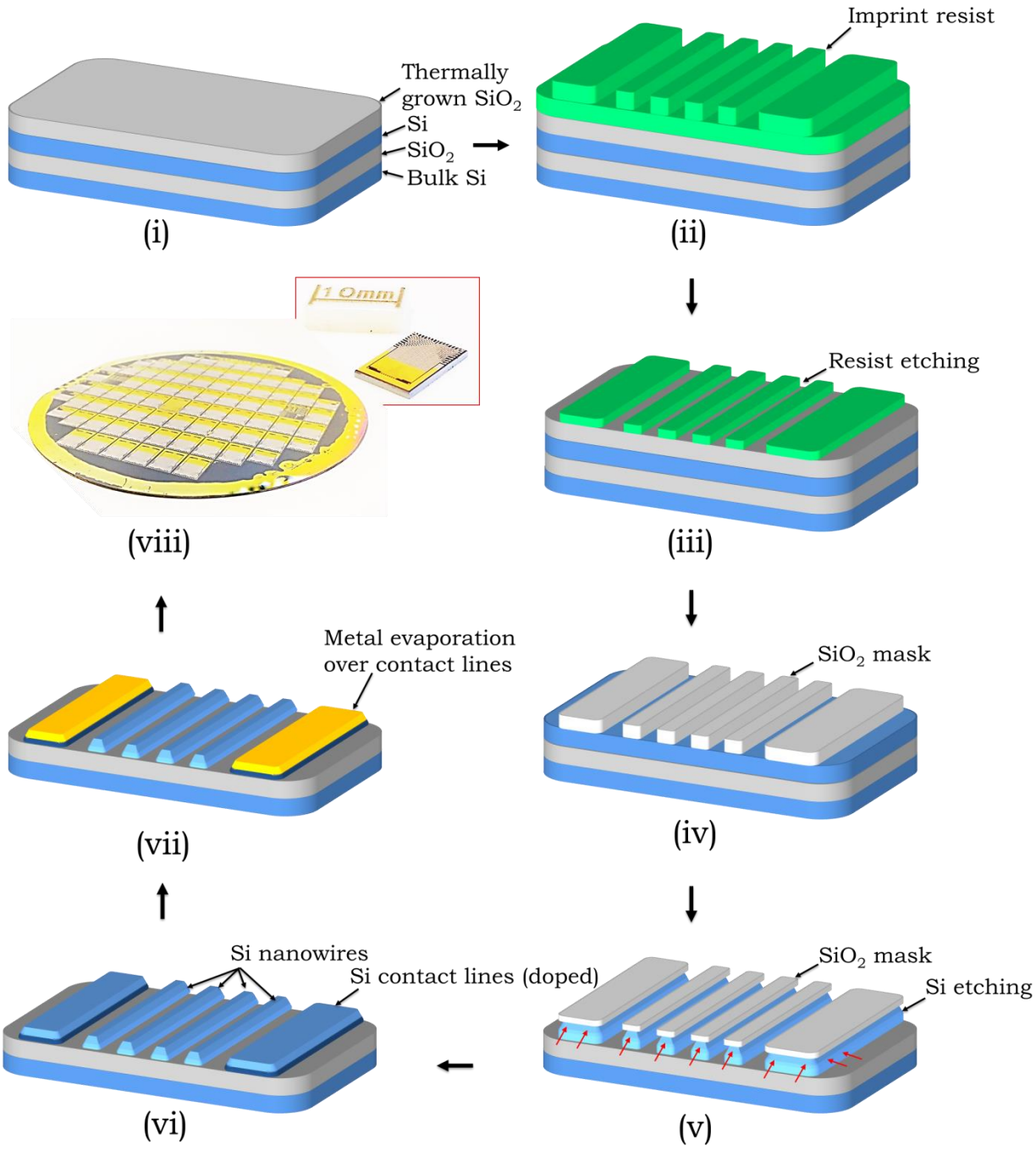

Figure 3.5 Schematics of the process flow for the fabrication of Si NW FETs (clockwise): (i) SOI wafer after the thermal oxidation process to grow a SiO_2 layer on top; (ii) SOI wafer coated with patterned thermoresist after the NIL process; (iii) Thermoresist coated SOI after the RIE of the residual layer; (iv) Structured SiO_2 layer (mask) over the SOI wafer after the dry etching process for SiO_2 and for removal of the leftover thermoresist; (v) Wet anisotropic etching of the Si layer; (vi) Si NW and contact line regions structured in the Si layer after boron implantation of the contact lines using one photolithography step for the NW passivation; (vii) Evaporation of Al/Ti/Au over the implanted Si contact lines using a second photolithography process and a lift-off process; and (viii) Final 4" SOI wafer with the 32 Si NW FETs layout on 7 mm × 10 mm chips (a photograph of a single chip shown in the inset).

The dry etching process was continued further to transfer the pattern to the exposed SiO_2 layer underneath by carrying out RIE in 30 sccm CHF_3 at 200 W power and 3 Pa pressure for 100 seconds (figure 3.5 (iv)). This step also needed initial optimization in order to find the right etching rate for the dry thermal oxide. The patterned SiO_2 layer was then used as a hard mask to structure the underlying Si layer, using TMAH solution in the anisotropic wet etching process (figure 3.5 (v)) as it was described in section 2.4.1 of chapter 2 [116]. After the anisotropic wet etching process, the Si NWs and contact line structures on the mould were finally transferred into the thin Si top layer of the SOI wafer and thus a parallel production of many of Si NW FETs was realized. Before starting the TMAH etching process, the wafers were cleaned with fresh piranha solution (3:1 ratio of H_2SO_4 and H_2O_2) for 10 minutes followed by rinsing with deionized (DI) water. The hard mask residues and native oxide were also removed by dipping the wafers into 1% hydrogen fluoride (HF) solution for 120 seconds. Thereafter, the wafers were rinsed with DI water. Anisotropic etching was carried out by dipping the wafers into 25% TMAH solution at 90 °C for 60 seconds and was followed by several times rinsing with DI water. The Si was etched down to the BOX layer in a few seconds as it was observed by a change of the wafer colour. After the TMAH etching process, the oxide hard mask was completely removed by 1% HF (9 minutes). The NW FETs structured into the top Si layer of the SOI wafers exhibited a semiconductor characteristics with a resistivity of around 8-22 Ω.cm. In the following step, the source and drain contact line regions in the top Si layer were p-doped by boron ions using an ion implantation process. The implantation process was carried out as a service at Ion Beam Services, Peynier, France. Thereby, the serial resistance of the contact lines was reduced by the doping process while keeping the carrier mobility high in the un-doped Si NWs channels [112]. For the implantation of the contact lines and the optimum operation of the resulting Si NW FETs, the ion implantation energy, dose and thickness of the passivation layer on the Si NW regions are very important. Since these parameters were not known and also due to the out-of-house processing of this step it was decided to carry out simulations prior to the implantation process, which are described below.

The implantation energy defines the projection range in the sample and this can be obtained from the stopping/range tables using “The Stopping and Range of ions in Matter (SRIM)” software (2008 version) [141]. With this program the stopping and range of ions into the matter was calculated using quantum mechanical treatment of the ion-atom collisions. For a 40 nm projection range in Si (top Si layer only implanted), 10 keV energy for boron ions was required as it is shown in the graph A of figure 3.4. TRIM is another program which calculates both the final 3D distributions of the ions and also kinetic phenomenon associated with the ion’s energy loss such as target damage, sputtering, etc. Another important parameter required for an ion implantation process is the implantation dose, which defines the concentration of ions that needed to be doped. For the degenerated semiconductor material (quasi-metallic conductivity) a concentration of dopants should be in the order of 10^{20} atoms/cm^3. From the SRIM 2008 version-TRIM calculation, graph B in figure 3.4 was obtained.

Here the Y-axis represents the ratio of atoms/cm^3 (dopant conc.) to atoms/cm^2 (implantation dose). To find the dose i.e., atoms/cm^2, the dopant concentration is divided by the peak value in the graph i.e., 20×10^4 events. Therefore the required implantation dose was estimated to approximately 10^{15} atoms/cm^2.

In order to prevent the implantation in the Si NW region, the surface is usually passivated with a SiO_2 layer. The thickness of the passivation layer was calculated using the following formula [35]:

$$T = \frac{e^{(-u^2)}}{2 \times (\sqrt{\pi}) \times u} \tag{3.2}$$

-where $u = (d - R_p)/((\sqrt{2}) \times \sigma)$, T (Transmission coefficient) = 10^{-4}

-where d is the thickness of the SiO_2 mask required to prevent the ion diffusion, R_p is the projection range and σ is the longitudinal straggling.

For an implantation energy of 10 keV, a SiO_2 layer thickness in the order of 130 nm was calculated (from eq. 3.2) for effective Si NW surface passivation. This thickness was found to be incompatible with our process flow. However, a thick layer of photoresist can also be used for passivation of the Si NW surface. As a result of the above simulations and estimations an implantation energy of 10 keV was used for an ion projection range of 40 nm into the top Si layer with an implantation dose of 10^{15} atoms/cm^2. The ion irradiation was carried out at an angle of 7° tilt in order to prevent the ion channeling effect. To carry out an implantation of the contact lines, an UV lithography step*** was done to passivate the Si NWs by a photoresist layer (2 μm thick). This effectively protected the Si NWs from the ion implantation.

After the implantation step, the photoresist was removed using acetone and isopropanol followed by standard RCA cleaning. The energy of the implanted ions (boron ions) was lost when they penetrated deeper into the substrate. Eventually the crossover energy limit was reached where nuclear stopping becomes prominent. Since most of the lattice disorder occurs near the final ion position, this lattice disorder was necessary to be repaired and thus Rapid thermal annealing was required. Therefore, the implanted ions were activated using a high temperature (at 850 °C for 30 minutes) annealing process in nitrogen (N_2) environment. Thereafter a dry thermal oxidation process in oxygen (O_2) environment (at 820 °C for 45 minutes) was carried out, where a dry oxide layer (SiO_2) of around 8 nm thickness was generated on the Si surface. The grown oxide layer worked as a gate dielectric as well as a passivation layer for the contact lines (figure 3.5 (vi)).

*** The 5” soda lime photolithography masks used in this thesis work were obtained from Delta Mask, Netherlands (http://www.deltamask.nl/). The masks were fabricated with specifications such as bright field, chromium down and right reading.

Lastly, a second UV lithography step was carried out to open the outer part of the contact line regions where the metal needed to be deposited. The oxide in the open areas was removed using a 1% HF dip and the metal evaporation process was carried out. This was followed by a lift-off process resulting in part of the contact lines and contact pad areas covered with a metal layer composed of Al (200 nm), Ti (20 nm) and Au (150 nm) as inferred from figure 3.5 (vii), (viii). After the metal evaporation, wafers were annealed in vacuum at 350 °C for 10 minutes to obtain ohmic contacts between the metal bond pads and the doped Si contact lines. Thus the deposition of metal on the contact line provided a low resistance for the charge carriers to flow through the Si NWs [112].

3.1.3. Characterization at different fabrication steps

During the fabrication process of the Si NW FETs, the structure of the Si NWs was characterized by methods, which include optical microscopy, scanning electron microscopy (SEM) and AFM. Additionally, the thickness of Si device layer before and after the thermal oxidation process was characterized using spectroscopic ellipsometry. These characterization methods were used to optimize the parameters for the fabrication process and they are described in the following subsections.

Ellipsometry measurements of SOI wafers

The thickness of different layers of the SOI wafers was measured using an ellipsometry spectroscopic technique (SEN850 from SENTECH GmbH, Berlin) and some exemplary results are given in table 3.1. The thickness of the initial Si and the underlying buried oxide was measured as 87.3 nm and 145.2 nm, respectively.

Layer	Before oxidation	After oxidation
SiO_2 thermal	-	45.1 nm
Si	87.3 nm	67.0 nm
SiO_2 BOX layer	145.2 nm	147.7 nm

Table 3.1 Exemplary ellipsometry measurements for the thickness of different layers of the SOI wafer before and after the thermal oxidation step.

As explained in the previous section, the top Si layer was oxidized to SiO_2 by a dry thermal oxidation process at 1000 °C for 1 hour in O_2 environment. The as consumed thickness of Si during the oxidation process is given by-

$$t_{Si} = 0.44 \times t_{SiO_2} \tag{3.3}$$

-where, t_{Si} represents the thickness of the consumed Si in order to get the thickness of SiO_2, represented by t_{SiO2}.

From table 3.1, it can be inferred that the thickness of the SiO_2 layer after the oxidation process was around 45 nm. Thus in the oxidation process the consumed Si thickness was

$$t_{Si} = 0.44 \times 45\ nm = 19.8\ nm$$

Since the initial thickness of Si was in the order of 87 nm, the leftover Si thickness was around 67 nm. This is in full agreement with the results obtained from the ellipsometry measurements.

Si NW FETs structural characterization

The structural characterization of the Si NW FETs is shown in figure 3.6.

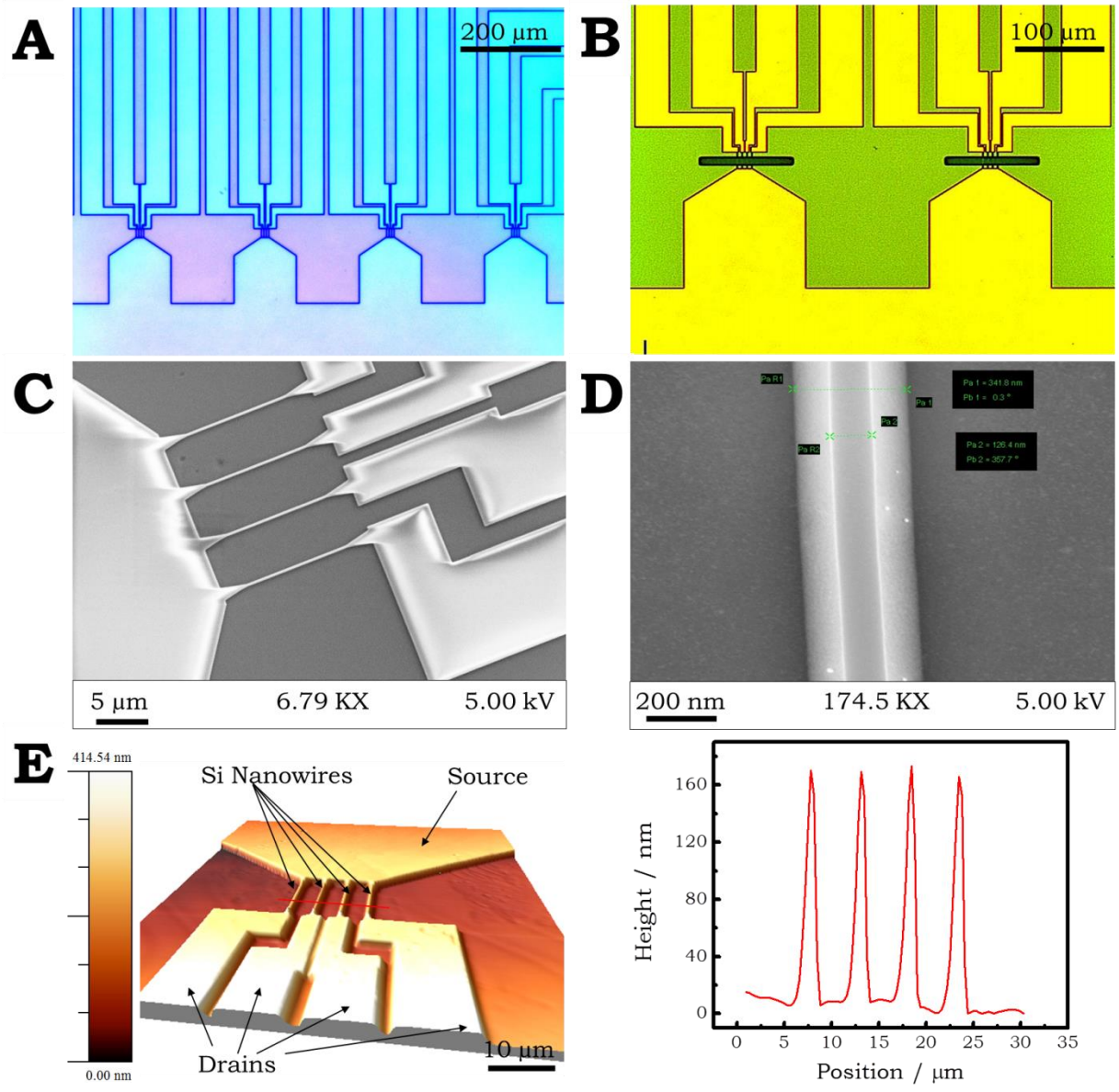

Figure 3.6 Microscopic characterizations of the Si NW FETs: (A) A zoomed out optical microscopy image of the sensor chip after the imprint process; (B) A microscopy image after the photolithography step for passivation of the NWs; (C) SEM image of one Si NW FET set after the TMAH etching process with (D) Zoomed in view of one NW; and (E) A detailed 3D view of one Si NW FET set characterized using AFM with a height profile of four individual NWs shown on the right side.

In figure 3.6 A, an optical image of a part of the sensor chip after the nanoimprint process (4 NW sets with 4 identical Si NWs each) is shown. In figure 3.6 B, another optical microscopy image of two Si NW sets is shown, where the Si NWs are covered with a resist passivation layer patterned using the UV lithography step prior to the ion implantation process. From figure 3.6 A and B it is quite clear that after the nanoimprint process optimization, the thermoresist was homogeneously filling all the micro- and nano-features of the mould. In figure 3.6 C, an SEM image (performed on a Zeiss Supra 40 microscope) of 4 high aspect ratio Si NWs after the TMAH etching process is shown. The length of the Si NWs was around 15 µm. The 4 Si NWs are parallel to each other with a spacing of 5 µm in between. It can also be inferred that the Si NW surfaces are very smooth and identical in structural detail (figure 3.6 C). The anisotropic wet etching process using TMAH resulted in a trapezoidal cross-section (described in section 2.4.1 of chapter 2) of the Si NWs as can be observed from the SEM image shown in figure 3.6 D. From the detailed SEM characterization (figure 3.6 D), the measured width of individual Si NWs is in the order of 126 nm on the top- and 340 nm on the bottom side. Additionally, from the AFM image (performed on Veeco Dimensions 3100) shown in figure 3.6 E, it can be inferred that the height of individual Si NWs was around 160 nm. This is due to etching of the underlying BOX during the previous wet etching steps in the fabrication process. Here care must be taken to not completely etch the BOX, thereby short circuiting the top and bottom Si. Thus, almost a “wrapped around gate” configuration is formed, emerging from the elevation of Si NWs from the BOX floor [112].

3.1.4. Problems related to NIL, RIE and UV lithography

The top-down nanofabrication approach using the combination of NIL and photolithography processes may in the end lead to some inherent issues that could be avoided in the future work in order to further refine the sensor platform realization on wafer-scale. Because of the inhomogeneous distribution of the nano- and micro-structures on the NIL mould, the nanoimprint process leaded to a large variation in the residual layer thickness over the whole wafer. This in turn resulted in inhomogeneous etching of the structures *via* the O_2 plasma thereby resulting in faster etching of the thinner nanowires in comparison to the thicker nanowires. As shown in the SEM images in figure 3.7, the thinner wires in B and C were partly etched, while the thicker ones in A remained unaffected. This can be explained from the fact that the O_2 plasma during a RIE process etches the whole surface of the wafer uniformly and the thinner structures are etched faster in comparison to the thicker ones. It can also be inferred from the SEM image shown in figure 3.8 A that the presence of a thick residual layer near the contact pad region resulted in an incomplete etching of the Si after the TMAH etching process. On account of the wide distribution in width of the structures, during the NIL process the smaller structures were filled easily in comparison to the bigger structures. It can be deduced from the SEM image shown in figure 3.8 A and B, where there is incomplete filling of resist in the contact pad region in A, while it is perfectly filled in the thinner areas near the NWs as seen in B. These

issues are inherent to the NIL process and therefore it is important to consider uniform distribution of structures while designing the NIL mould.

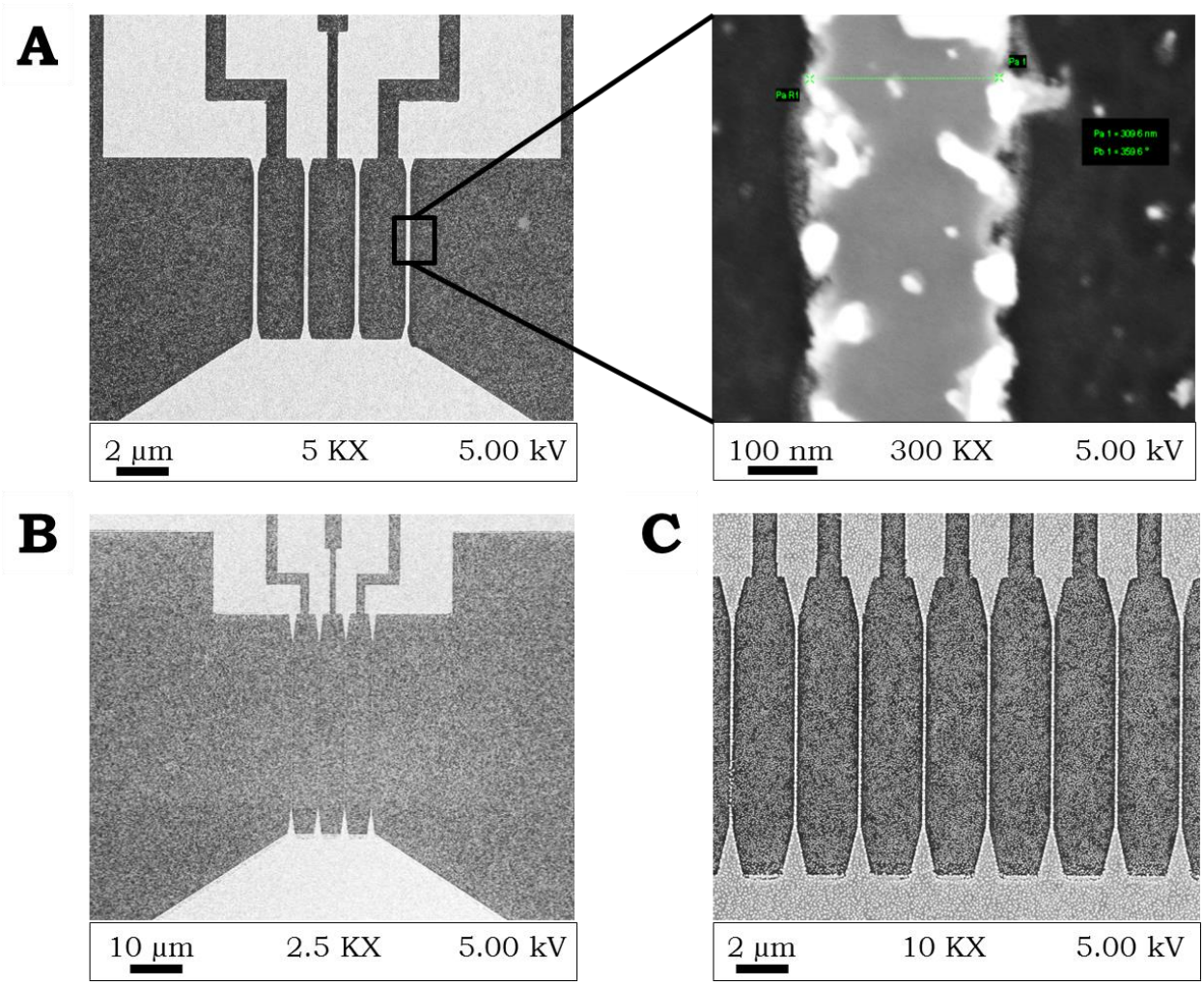

Figure 3.7 SEM characterization results showing the intrinsic problems in Si NW FETs fabrication, when combining the NIL and RIE processes: (A, B, C) SEM images of the NW sets with different NW widths after the RIE process.

Furthermore, the mould and photolithography masks, when obtained from different sources, could result in alignment problems. This could lead to a variation in the sensor properties (discussed in chapter 4) due to the misalignment occurring between the nanoimprint mould and the lithography masks. In our process such a misalignment resulted in a shift of the passivation mask for the nanowires towards the source/drain contact lines. This shift in the alignment could also arise from small variations in the structural features of the nanoimprint system components, such as the loader plate. It could also result from differences in size of the nanoimprint mould and wafers used during the imprint process. In our process a strong shifting of the passivation mask on the nanowires was observed towards the edges of the wafers.

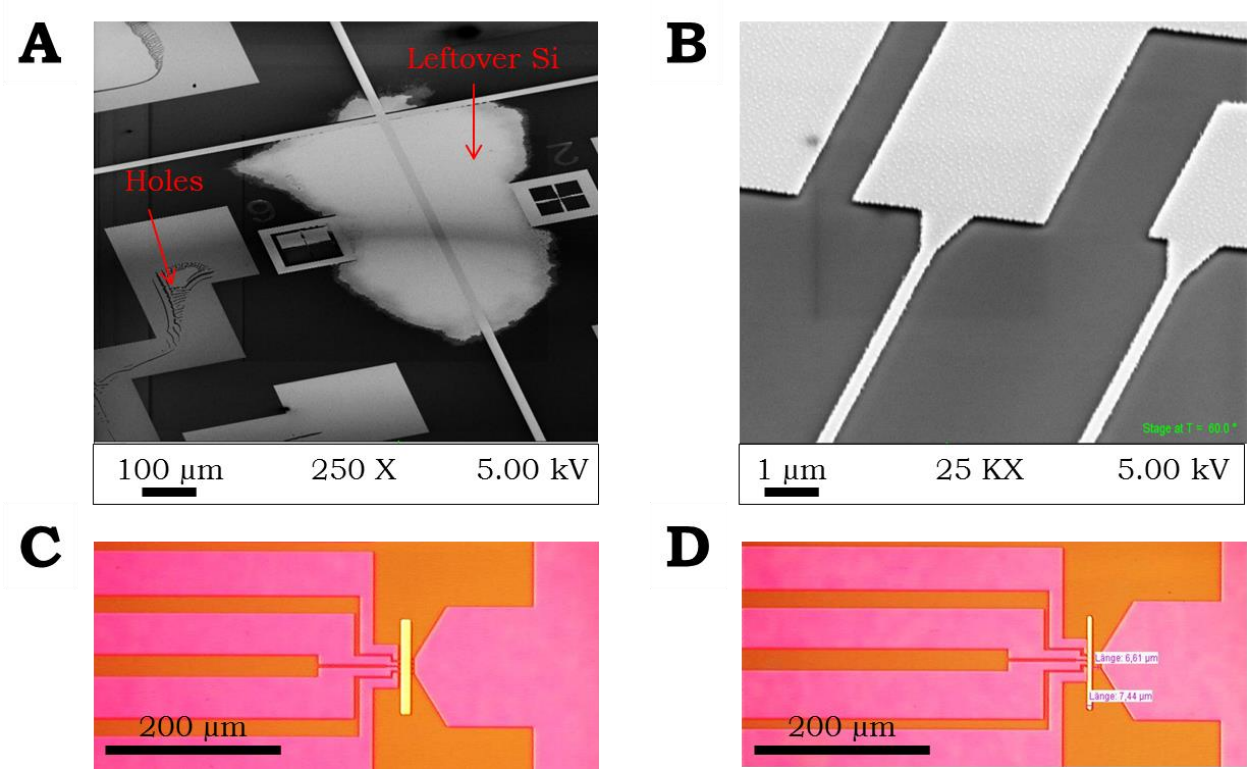

Figure 3.8 Microscopic characterization results showing examples of intrinsic problems in the Si NW FETs fabrication, when combining the NIL and UV lithography processes: (A, B) SEM images at different positions on the wafer after the TMAH etching step; and (C, D) Optical microscopy images of one NW set after the UV lithography step for ion implantation with perfectly aligned (C) and misaligned (D) passivation mask.

The nanowires with centre-aligned and left-aligned passivation masks on the nanowires before the ion implantation process are compared in the two optical images shown in figure 3.8 C and D, respectively. This misalignment resulted in a lower yield of functioning sensor chips per wafer. In general it is important to avoid such intrinsic system defects, when combining nanoimprint and optical lithography systems.

3.2. Si NW FETs sensor preparation

Direct electrical measurements of the Si NW FETs chips in liquid gate configuration are discussed in this section. The procedure for Si NW FET sensor encapsulation in order to enable portable measurements and simultaneous measurements of multiple transistors is also described. Additionally, the details for the microfluidic integration of the Si NW FETs for real-time optical bioassays are given.

3.2.1. Electrical measurement - Si NW FET chip encapsulation

The Si NW FET chips were electrically characterized in a 3 electrode configuration using a Keithley 4200 semiconductor parameter analyser (from Tektronix GmbH) and a wafer probe station. The drain-source voltage was applied *via* the probe needles,

which were in contact with the drain and source contact pads on the chip. Additionally, the gate-source voltage was applied *via* an external Ag/AgCl reference electrode (DRIREF-450 from WPI GmbH) suspended in a liquid droplet (10 mM PB at pH 7.4) over the gate oxide covering the Si NW area. After the basic electrical characterization, the Si NW FET chips were wire bonded on specially designed printed circuit boards (PCBs) in order to connect the chips to multiple transistor readout out systems. Two different kinds of PCBs were designed using the EAGLE software (version 7.3.0) and the pictures are shown in figure 3.9 A and B (both left side). The contact pads on the Si NW chips were wire bonded to the specific contacts on these PCBs with an aluminium wire (Al/Si 1%, 25 µm in diameter) using a wedge-wedge wire bonding system (West Bond Inc., USA). Thereafter, the contact lines and wire bonded contact pads were covered with PDMS (purchased from Dow-Corning (Midland, MI, USA) as a Sylgard 184 silicon elastomer kit) in order to protect and isolate them from the external environment.

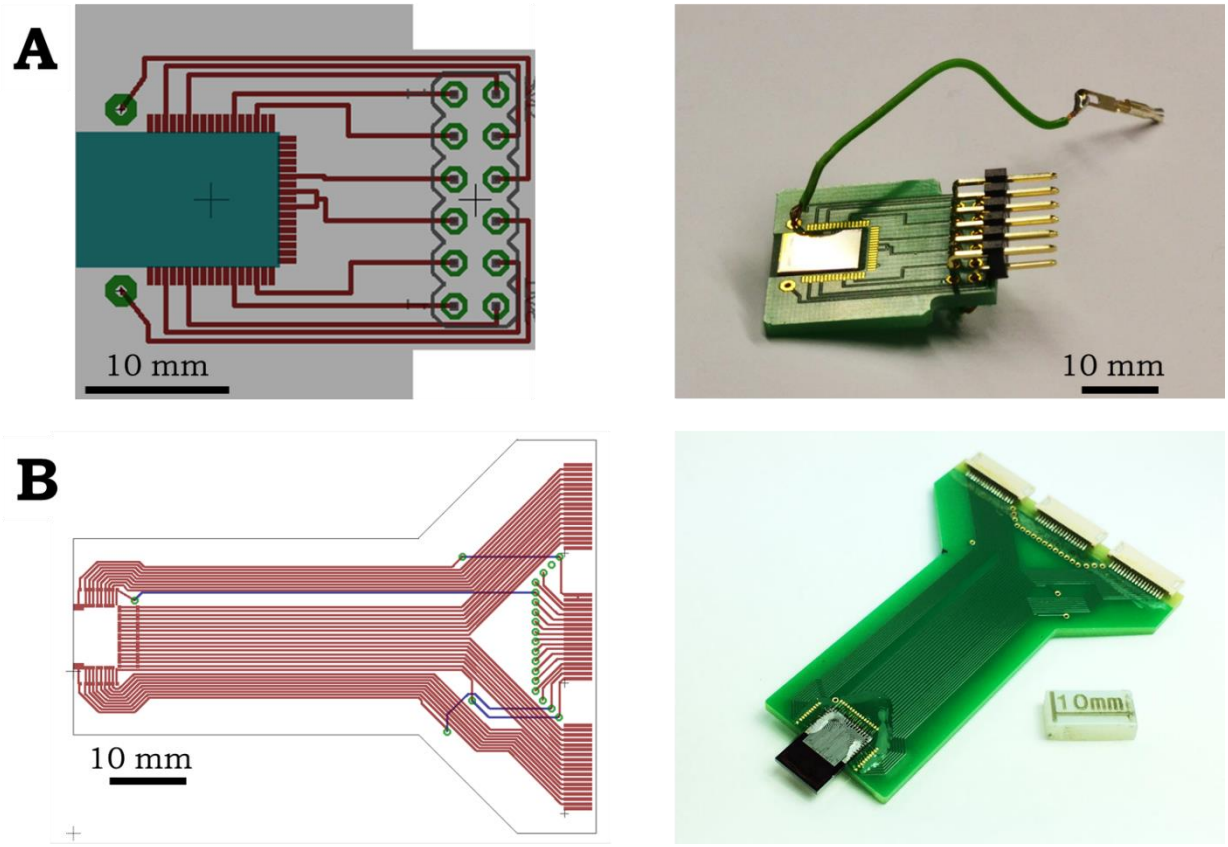

Figure 3.9 Left: A snapshot of the PCB designed using the EAGLE software for the Si NW FET chip for (A) a 4-channel setup with which only 4 FETs can be measured; (B) a 32 channel setup with which 32 FETs can be measured simultaneously. Right: A picture of the Si NW FET chip wire bonded and encapsulated on a (A) PCB for the 4-channel setup; (B) PCB for the 32-channel setup.

The picture of two kinds of encapsulated chips used in this thesis is shown in figure 3.9 A and B (both right side). The PCB design shown in figure 3.9 A is for a “four

channel" readout system with which 4 Si NW ISFETs can be measured simultaneously in transfer characteristics and real-time mode [142]. Further, the PCB design shown in figure 3.9 B is for a "32 channel readout" system for the measurement of 32 Si NW ISFETs, simultaneously.

3.2.2. Optical measurement - Si NW FET chip microfluidic integration

In order to carry out the optical assays for biomolecules, the Si NW FET chips were integrated with a microfluidic structure. For microfluidic integration of the chips, special configurations of PDMS microfluidic channels were designed using conventional lithography methods. The fabrication of two kinds of microfluidic channels is described here. This included a simple straight PDMS channel layout with "one inlet and one outlet". Further, the configuration of a mixer channel with "two inlets and one outlet" is also discussed.

Straight microfluidic channel design

The microfluidic device was fabricated by a conventional process of replication of a PDMS structure from an SU-8 mould [143-144]. The layout of the simple straight microfluidic channel with dimensions of 100 µm width and 4 mm length was designed using the Clewin software. Thereafter, the SU-8 mould with the microfluidic channels layout was fabricated using conventional lithography methods such as direct laser writing and UV lithography.

The different steps in the SU-8 (SU-8 2015, a negative photoresist from MicroChem, Newton, MA, USA) mould fabrication are illustrated in figure 3.10. The fabrication was done in INESC MN, Portugal, as part of a research stay in the framework of the European project PROSENSE (parallel sensing of prostate cancer biomarkers). For the fabrication of the SU-8 mould, Aluminium (Al, 200 nm) on glass wafer (figure 3.10 (i)) was patterned by direct laser writing. As illustrated in figure 3.10, the Al/glass wafer spin coated with resist (figure 3.10 (ii)) was exposed to direct laser writing (figure 3.10 (iii)) with the simple fluidic channel layout. Thereafter, the resist was developed resulting in trenches in the resist layer (figure 3.10 (iv)). Then, the underlying Al was etched to have trenches in the Al layer (figure 3.10 (v)). This patterned Al/glass wafer after the resist removal acted as a mask for patterning the SU-8 on Si wafer (figure 3.10 (vi)). The Si wafer was spin coated with SU-8 (20 µm thick) and then baked at 95 °C for 4 minutes. Next, the SU-8/Si wafer was aligned with the Al mask and exposed to UV light. After a post bake step at 95 °C for 5 minutes, the SU-8/Si wafer was developed in Propylene glycol mono-methyl ether acetate (99.5% from Sigma-Aldrich) for 2 minutes. Then the patterned SU-8/Si wafer (i.e., SU-8 mould) was cleaned with isopropanol (figure 3.10 (vii)) and a final step of hard bake at 150 °C for 15 minutes was carried out. The fabricated SU-8 mould was then ready for curing of the PDMS structures and was useable for multiple times. For the PDMS structures curing, the PDMS components, which included a 1:10 ratio of the curing agent to the PDMS pre-polymer, were mixed well and poured over the SU-8

mould. Then, it was cured in an oven at 70 °C for 75-90 minutes and finally the PDMS structures were peeled off from the SU-8 mould (figure 3.10 (viii)).

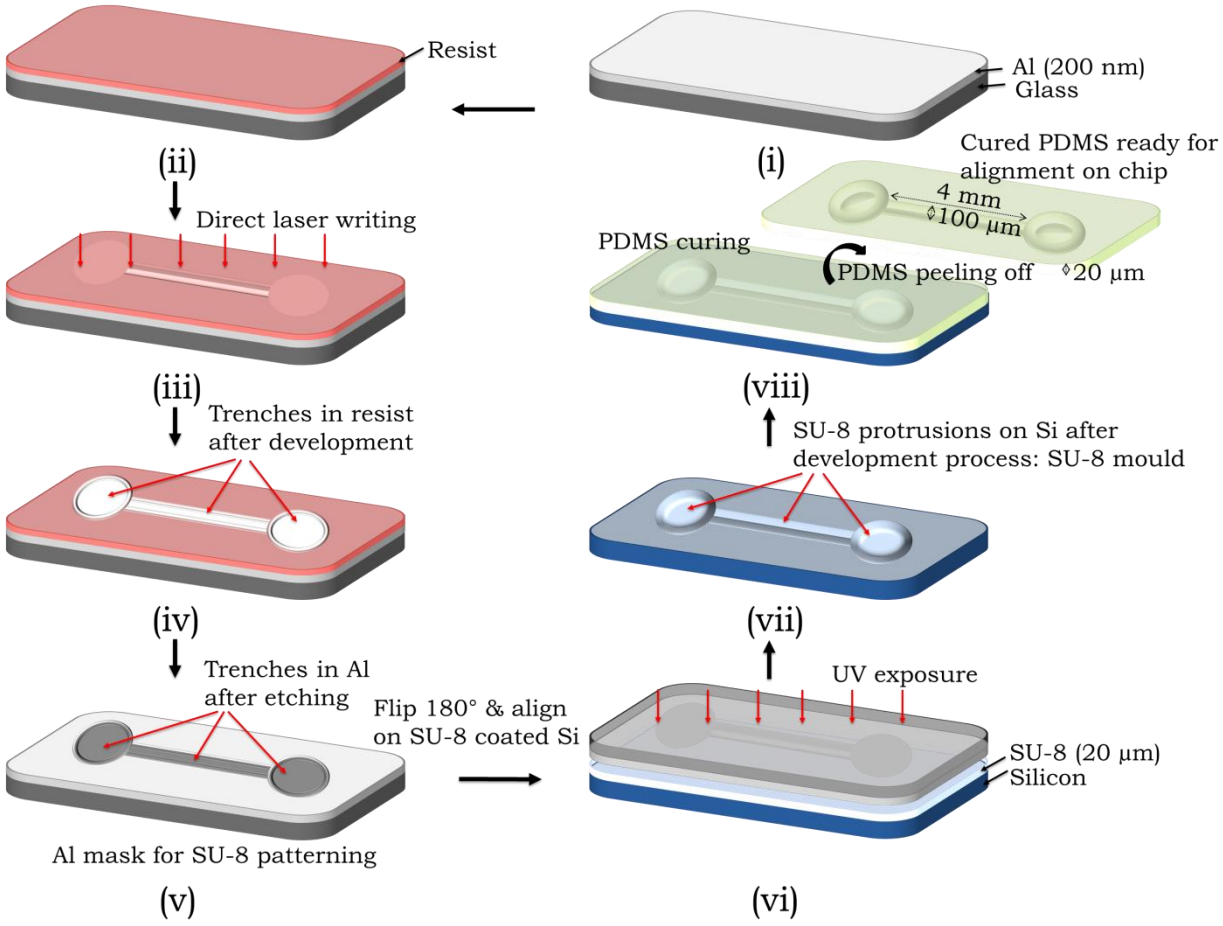

Figure 3.10 Schematic of the process flow of SU-8 mould fabrication for the straight microfluidic channel design (counter clockwise): (i) Al (200 nm) on glass wafer; (ii) Resist coating on Al/glass wafer; (iii) Direct laser writing with the desired microfluidic layout; (iv) Trenches in the resist layer after the development; (v) Etching of the Al layer resulting in trenches in the Al layer and this patterned Al/glass wafer acted as a mask for the patterning of SU-8 resist on the Si wafer; (vi) A Si wafer spin coated with SU-8 (20 µm thick) resist aligned below the structured side of the Al mask and then UV exposure; (vii) After the development process, SU-8 protrusions on Si wafer at the channel region and this patterned SU-8/Si wafer acted as a mould for curing the PDMS; and (viii) Curing of PDMS using the SU-8 mould and then peeling off to have the straight microfluidic channels in the PDMS layer.

Thereafter, holes were punched with a blunt 20-gauge needle (from Instech Solomon, Plymouth Meeting, PA, USA) through the inlets and outlets of the PDMS structure. For sealing of the PDMS structure (with microchannel width, w = 100 µm, height, h = 20 µm and length, l = 4 mm) to the cleaned Si NW FET chip, both were subjected to an UV-ozone treatment for 5 minutes at 28–32 mW cm^{-2} (UVO cleaner 144AX, Jelight Company Inc., CA, USA) for surface oxidation [145]. Then both, the surface oxidized PDMS structure and the Si NW FET chips were aligned under an

optical microscope and pressed gently to ensure a firm bonding. After one day the microfluidic devices were permanently sealed and ready to be used for the optical assays.

Mixer microfluidic channel design

In addition to the simple straight microfluidic channel, a "two inlets and one outlet" mixer channel was also designed to allow the mixing of reagents within the microfluidic channels for biological applications. In general, mixing of two or more substances is required for various biological tests for instance, for dilution of different analyte solutions. The flow of a fluid in channels of micron dimensions is laminar (Reynold's number, R << 2300), where there is a linear movement of particles parallel to the walls of the channel. The flow profile is parabolic with highest velocity at the centre of the channel and zero velocity at the channel walls. The particle transfer can only occur in the direction of the fluid flow and in the absence of turbulence, the mixing occurs only by diffusion between the two different streams [146-147]. Diffusion is a process by which the particles diffuse over time until they are uniformly distributed over the entire volume and is due to Brownian motion of the particles resulting in their random spreading. However, for efficient mixing, the length of the channels should be in cm-range as diffusion time can be in the range of several minutes for µm wide channels. Thus, such systems are impossible to be integrated on a LOC device with mm scale dimensions [148]. Therefore, several other ways have been explored in order to carry out the mixing in microfluidic channels with aim to generate a transversal flow in addition to a laminar flow (turbulences at Reynold's no > 2300 help in mixing-turbulent flow).

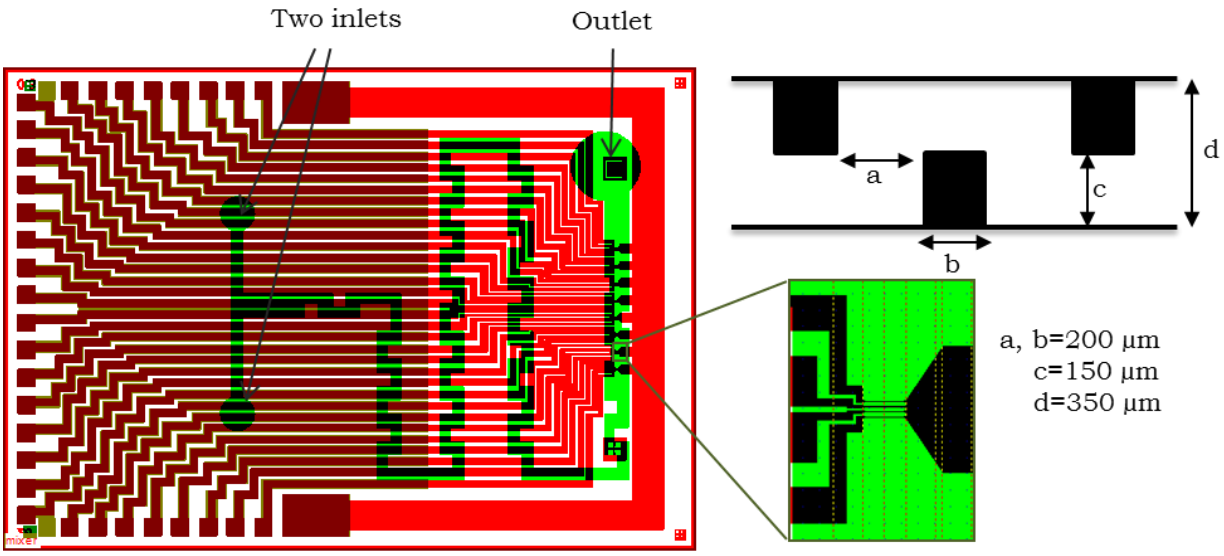

Figure 3.11 Layout of the Si NW FET chip with a mixer channel, which includes two inlets and one outlet. The baffles (black bars shown on the right side top) are created within the channel walls in order to mix the fluids through the two inlets.

Two kinds of mixers have been reported in literature for mixing applications, which include active and passive mixers. In active mixers, external forces (e.g., magnetic) are employed to enable a fluid mixing. On the contrary, in passive mixers the channel geometry is modified to fold the fluid streams to increase the interface between the involved liquids with shortened mixing path [149-151]. Although mixing efficiency of active mixers is better than that of passive mixers, their complex integration on a microchip makes the fabrication process more complicated and expensive. Consequently, passive mixers are more commonly employed in LOC devices. For the work reported in this thesis, a simple configuration of a passive mixer was designed.

A simple passive mixer channel with two inlets, one outlet and baffles (obstacles shown as black bars) at the channel walls was designed (illustrated in figure 3.11). The presence of baffles at the channel walls allows more interfacial contacts between the fluids [152]. The width of the channel was on the order of 350 µm and the length of 15 mm in order to allow the fluids through the two inlets to mix well before reaching the NW region.

The above described microfluidic design can also be fabricated *via* the lithography procedure described in figure 3.10. Thereafter, the fabricated SU-8 mould can be used for curing PDMS structures for future alignment on the Si NW FET chips.

After the microfluidic integration of the Si NW FET chips by the above described methods, the optical assays for biomolecules were carried out. A fluorescence microscope (Leica DMLM) linked to a digital camera (Leica DFC300FX) was used for imaging the microfluidic channels and recording of the signals.

3.3. Surface functionalization of Si NW FET chips for sensing experiments

The Si NW FET chips were surface functionalized in order to use them for sensing of pH and biomolecules such as prostate cancer biomarkers and T-cell cytokines. The different steps involved in the surface functionalization are described in the following subsections.

3.3.1. Functionalization for pH sensing applications

The Si NW FETs were deployed as pH sensors to determine the sensor characteristics, reproducibility and variation in their sensor characteristics. The Si NW FET chips were surface-modified with pH sensitive molecules such as APTES in a gas-phase silanization method [153]. Before the silanization process, the chips were cleaned using piranha solution (1:3 ratio of H_2O_2 and H_2SO_4) for 10 minutes at 60 °C. This resulted in a high density of hydroxyl groups (-OH) on the nanowire surface as it is illustrated in figure 3.12 A. For the silanization in an oxygen free environment the Si NW FET chips were placed inside a vacuum chamber (illustrated in figure 3.12) and a silane container tube with 200 µl of APTES was connected to the vacuum chamber.

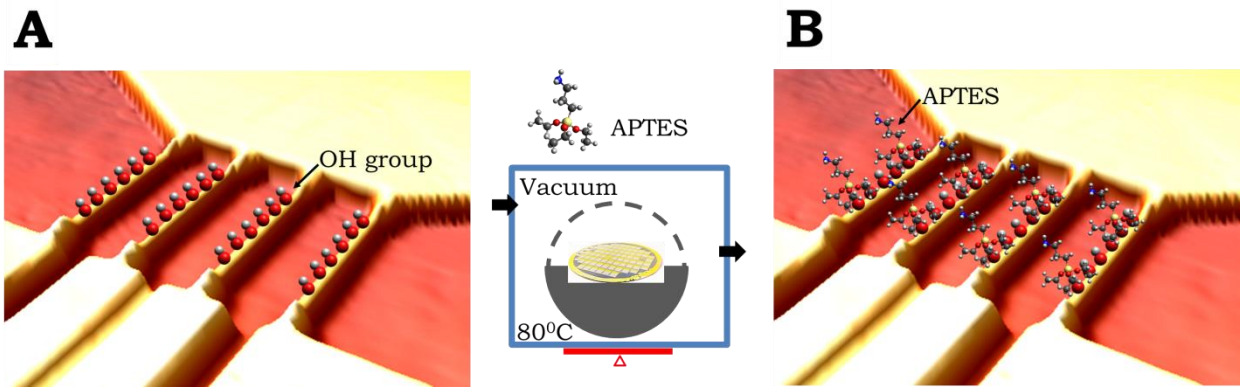

Figure 3.12 Schematic for the gas phase silanization process of the Si NW FET chips: (A) Piranha cleaning of the Si NW FETs to have a high density of -OH groups at the Si NW surfaces; and (B) APTES silanization in gas phase to uniformly assemble APTES molecules on the Si NW surfaces.

Thereafter, the vacuum chamber was heated up to 80 °C and the silanization process was carried out for 2 hours and 30 minutes. A similar process was used for silanization of the chips with GPTES. After the silanization, the chips were cleaned with DI water to remove the excess silane. During this surface functionalization process the silane molecules form a covalent bond with the -OH groups present on the gate oxide (SiO_2) of the Si NW surfaces. Thus, the silane molecules uniformly assemble on the Si NWs as it is illustrated in figure 3.12 B. The gas-phase silanization methods are comparatively better suited against other protocols, for realizing highly homogeneous self-assemblies of molecular layers over large surface areas [153].

After the APTES functionalization, the chips were measured in PB solutions of different pH (from pH 4 to 10) at the same concentration (10 mM) in order to study the influence of buffer pH on the current through the transistors.

3.3.2. Functionalization for PSA detection applications

The electronic detection of prostate cancer biomarkers such as PSA was carried out using a new receptor-analyte combination, where PSA-specific aptamers were used as receptors and PSA molecules as analytes. The PSA immobilization protocol was firstly optimized on micro (μ) Si FET chips available in our research group (fabrication described earlier [142]) and then transferred on to the Si NW FET chips. Additionally, the PSA-aptamer immobilization on the Si NW surfaces was also confirmed by optical methods using chemiluminescence and fluorescence immunoassays. In order to carry out the optical assays, the Si NW FET chips were integrated with microfluidics using PDMS microfluidic channels as it was described in section 3.2.2 of this chapter. The details of the surface immobilization steps carried out for the detection of PSA by electronic and optical methods are given in the following subsections.

Electronic assay for PSA

For the electronic detection of PSA, PSA-specific receptors were covalently immobilized over the Si NW surfaces and the different immobilization steps are illustrated in figure 3.13. Here, PSA-specific amine-terminated aptamers with a 32 nucleotide sequence ([AmC6T]TTTTTAATTAAAGCTCGCCATCAAATAGCTTT) were used as receptor molecules for the detection of PSA [16, 154-155]. Firstly, the Si µ / NW FET chips were cleaned using piranha solution for 10 minutes at 60 °C in order to have high density of -OH groups at the gate oxide of the Si NW surfaces (illustrated in figure 3.13 A). Then, the chips were rinsed with DI water and silanized with 200 µl of GPTES using the above described gas phase silanization process (section 3.3.1). The silanization process resulted in a covalent binding of the silane molecules onto the surface of the SiO_2 gate oxide (figure 3.13 B) [112, 142]. Thereafter, the excessive silane molecules were removed by rinsing the chips with DI water. This was followed by site-specific spotting of the receptor aptamers over the Si NW sets using a microspotting technique (sciFLEXARRAYER S3, Scienion AG, Germany). Here around 800 pl volume of the aptamers with 2 µM concentration was used. After overnight incubation of the sensor chips in humid environment, the aptamers were covalently bound over the GPTES-functionalized Si NW surfaces (figure 3.13 C). Subsequently, the sensor chips were rinsed with 10 mM PB and dried. The remaining exposed sites of GPTES were then blocked using 1 M ethanolamine for 30 minutes as it is shown in figure 3.13 D. This was also followed by rinsing and drying of the sensor chips [154]. In the last step, increasing concentrations of PSA (from 1 pg/ml to 1 µg/ml) were immobilized in a humid environment consecutively each for 2 hours on the sensor chips (figure 3.13 E). Here after each immobilization step, the sensor chips were rinsed with 10 mM PB. After each of the above described immobilization steps (which include the immobilization of GPTES, aptamer, ethanolamine and different concentrations of PSA), the Si NW sensor chips were measured electronically in 10 mM PB at pH 7.4 [143-144].

Chemiluminescence immunoassays for PSA

In the chemiluminescence assays, a secondary antibody for PSA was immobilized in addition to the PSA-aptamer immobilization on the Si NW surfaces (figure 3.13 F). The secondary antibody for PSA was labelled with an enzyme, horseradish peroxidase (HRP) and is therefore called as anti-PSA HRP. After the immobilization of the secondary antibody on the Si NW surfaces, it is reacted with a substrate called Luminol (which was in an excited intermediate state after the oxidation reaction with hydrogen peroxide). On the reaction of Luminol with the HRP enzyme, the Luminol returns back to the ground state with emission of a photon (425 nm) [156]. Thus, the presence of HRP labelled secondary antibody indirectly confirms the presence of PSA bound over the Si NW surfaces [143-144].

The scheme of experimental steps in the chemiluminescence assay was the same as in the electronic assays (illustrated in figure 3.13). Here the biomolecules were allowed to flow through the microfluidic channel integrated Si NW chip at a controlled flow rate using a NE-300 syringe pump from New Era (NY, USA).

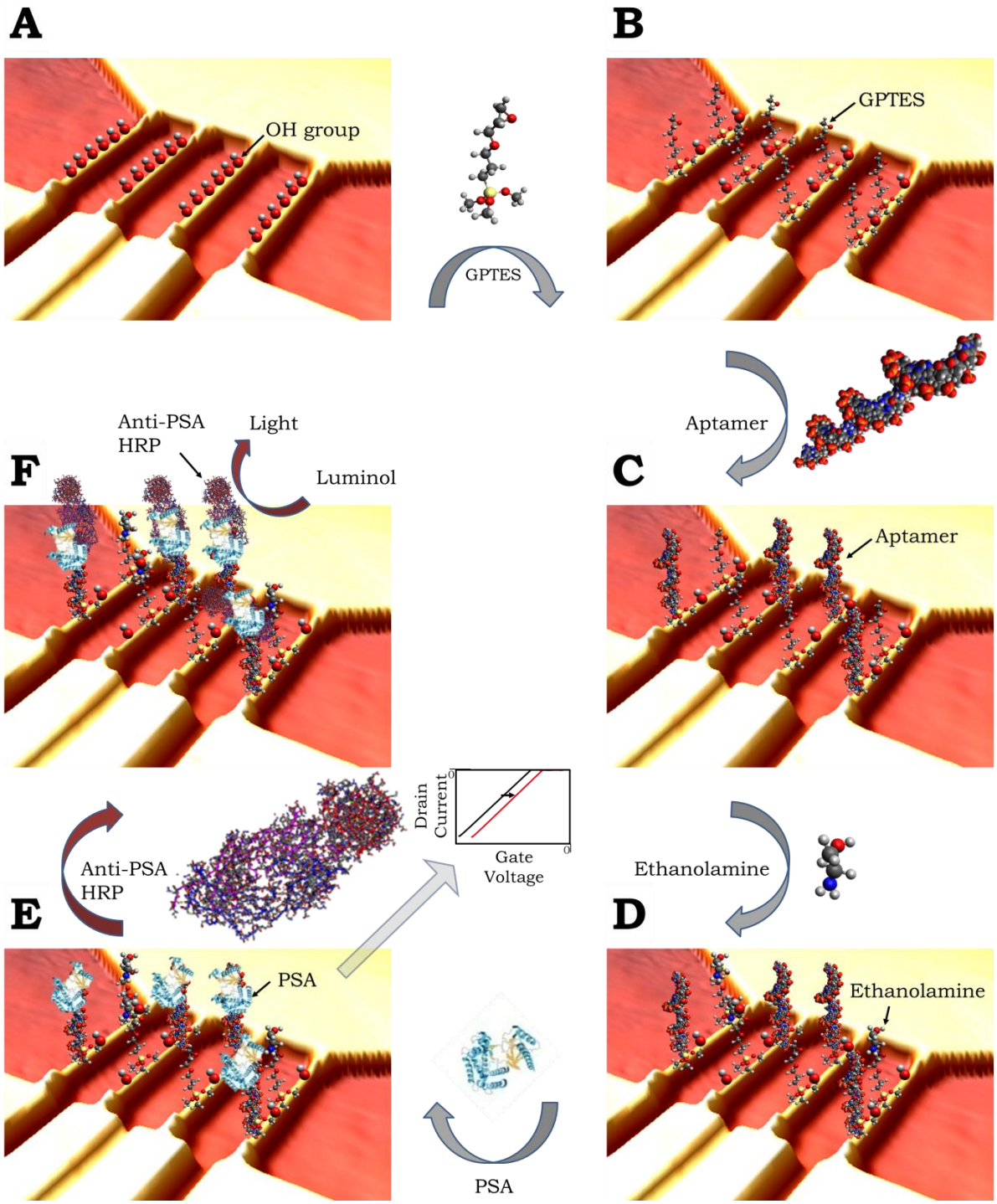

Figure 3.13 Schematic of different steps in the surface functionalization of Si NW FET chips for electronic and optical detection of PSA (clockwise): (A) Piranha cleaning for activation of the Si NWs to have high density of -OH groups; (B) Silanization of the Si NWs with GPTES in gas phase; (C) Amine-terminated, PSA-specific aptamer immobilization on the Si NWs; (D) Blocking using ethanolamine for the leftover GPTES sites on the Si NWs; (E) PSA binding to the aptamer-functionalized Si NW surfaces; and (F) Anti-PSA-HRP antibody binding to the PSA-aptamer complex on the Si NW surfaces. As indicated by the central inset, step E is typically the event for the electronic detection of PSA using Si NW FETs.

In short, the Si NW surfaces was silanized using GPTES (flow rate, Q = 0.5 µl/minute for 15 minutes), followed by cleaning with DI water (Q = 5 µl/minute for 5 minutes). Thereafter, the NH_2-terminated, PSA-specific aptamer with 20 µM concentration (Q = 0.5 µl/minute for 15 minutes), was flowed through the channels to bind to the Si NW surfaces. Then the Si NW surfaces was rinsed (Q = 5 µl/minute for 1 minute with PB) and the free GPTES sites were blocked using 16 mM ethanolamine (Q = 0.5 µl/minute for 5 minutes). This step was also followed by rinsing (Q = 5 µl/minute for 1 minute with PB) and then different concentrations of PSA ranging from 0 ng/ml, 50 ng/ml and 100 ng/ml were flowed through the different chips. Control experiments were carried out by using 20 µM concentration of a non-specific aptamer (5'-H3N-(CH2)6-AAAAATTAATTTCGAGCGGTAGTTTATCGAAA-3') sequence as the receptor molecule for each PSA concentration. This non-specific aptamer sequence should result in no binding of PSA. The non-specific aptamer was flowed through the channels at the same rate as the PSA-specific aptamer. In the end, 100 µg/ml of anti-PSA HRP antibody was flowed through the channels. For all the other reagents, a flow rate of Q = 0.5 µl/minute for 10 minutes was used and rinsing with PB was done at Q = 5 µl/minute for 1 minute. Additionally, for Luminol a flow rate of Q = 10 µl/minute was used [143].

Fluorescence immunoassay for PSA

In addition to the chemiluminescence immunoassay, a fluorescence immunoassay for PSA was carried out. Here another secondary antibody for PSA, which is labelled with a fluorescent dye Fluorescein isothiocyanate (FITC), was used. The so called "FITC anti-PSA antibody" was used to confirm the presence of PSA on the aptamer-functionalized Si NW surfaces. The scheme of the experimental steps for the fluorescence immunoassay was same as for the chemiluminescence assay. Here an anti-PSA FITC antibody was flown through the channels instead of the anti-PSA HRP antibody. The measurements were carried out directly after the rinsing step of anti-PSA FITC antibody (100 µg/ml) using a fluorescent microscope.

3.3.3. Functionalization for IL – 4 detection applications

Electronic detection of IL-4, which is a T cell cytokine, was carried out by the passive adsorption of IL-4 specific receptor antibodies over the Si NW surfaces. The different immobilization steps are illustrated in figure 3.14. Alpha (α) IL-4 antibody was used as the receptor molecule to do the specific detection of IL-4. For the passive adsorption of α IL-4 antibodies, the Si NW FET chips were cleaned using piranha solution (as described in the previous section) to have a high density of -OH groups at the Si NW surfaces (figure 3.14 A). The sensor chips were then rinsed with DI water and dried. Thereafter, they were incubated with α IL-4 (1 µg/ml) antibodies in humid environment overnight at 37 °C (figure 3.14 B). After the incubation, the sensor chips were rinsed with 10 mM PB and dried. Here, the passive adsorption of antibodies over the Si NW surfaces was monitored electronically by carrying out the transfer characteristic measurements (in 10 mM PB at pH 7.4) before and after the receptor antibodies immobilization.

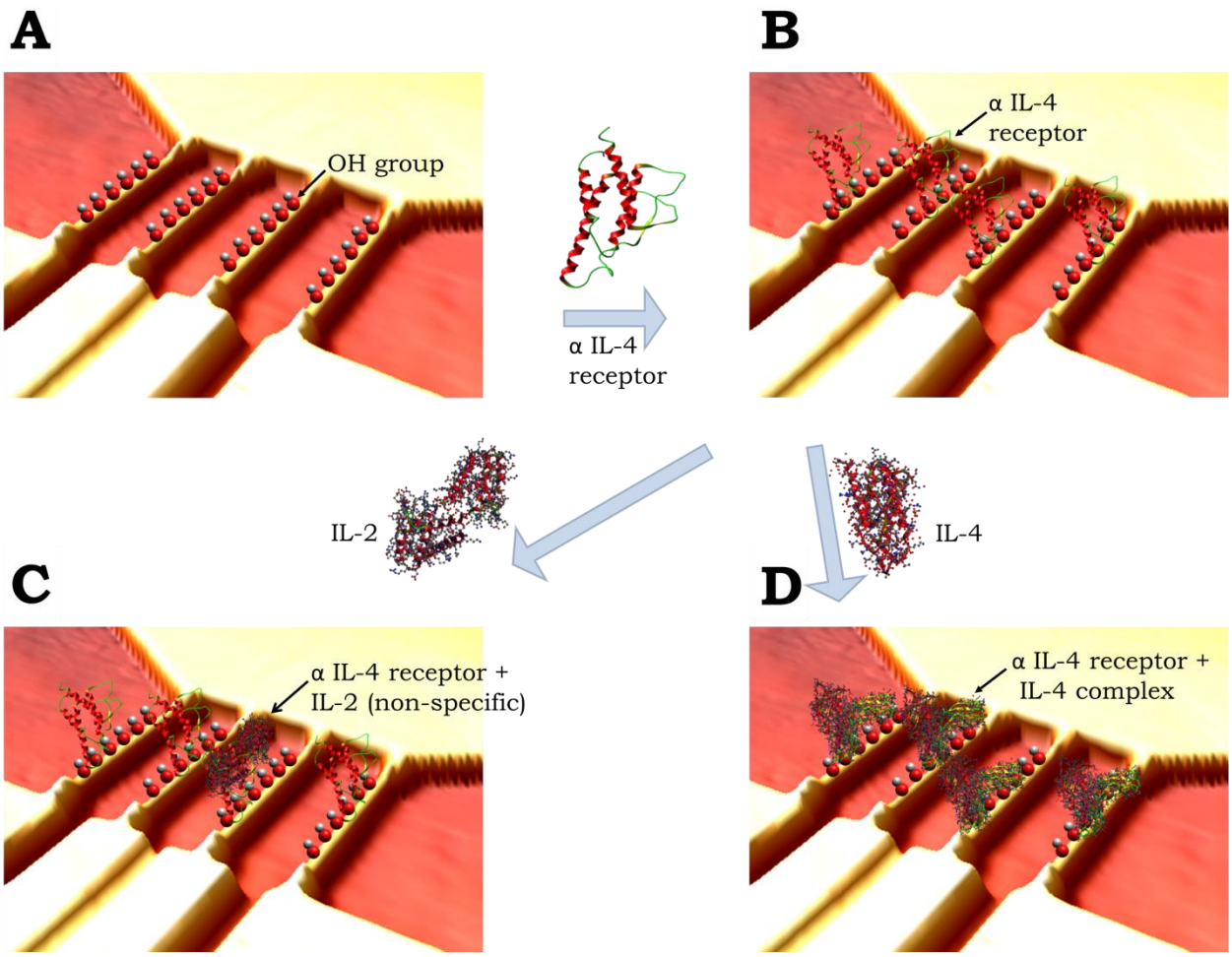

Figure 3.14 Schematic of the surface functionalization of Si NW FETs for electronic detection of cytokine IL-4: (A) High density of -OH groups after the activation of Si NWs using piranha cleaning; (B) α IL-4 adsorption over the Si NW surfaces; (C) IL-2 immobilization on the α IL-4 functionalized Si NW surfaces to check non-specific binding of IL-2; and (D) IL-4 and α IL-4 complex formation after IL-4 immobilization over α IL-4 functionalized Si NW surfaces (3D structure of proteins adapted from - Pdb: 1IAR, 2B8U) [157-158].

In the next step, the sensor chips were immobilized with known concentration of the recombinant protein IL-4 (250 µg/ml) and unknown concentrations of Th 2 (which is the cell culture medium with IL-4) for 2 hours at 37 °C in a humid environment. Separate sensor chips were used for respective control experiments. The control chips were immobilized with known concentration of recombinant IL-2 (100 µg/ml) and unknown concentrations of Th 0 (which is the cell culture medium without IL-4) in the same conditions as mentioned before. Thereafter, the sensor chips were rinsed and dried. On immobilization of IL-4 onto α IL-4 functionalized Si NW surface, a complex of IL-4 and α IL-4 is formed (figure 3.14 D). For the control experiments, the IL-2 was non-specifically adsorbed over α IL-4 functionalized Si NW surfaces as it is illustrated in figure 3.14 C. In each of the above-mentioned immobilization steps for IL-2 and IL-4, transfer characteristic measurements of the FET sensors were carried out to monitor the binding of antibodies over the Si NW surfaces electronically. Further, real-

time measurements were carried out by continuous drain-source current measurements with increase in the concentrations of recombinant IL-4 protein from 25 fg/ml to 2.5 μg/ml. In these measurements each concentration of IL-4 was made to run for 2 hours.

This chapter provided a detailed account of the different processes and methods involved in the fabrication of Si NW FET sensors in our top-down, wafer-scale procedure. The use of NIL for wafer-scale production of Si NW FETs was successfully demonstrated. Si NWs as small as 250 nm in width were fabricated. The process involved a wet-etching step, which was one of the merits to fabricate such high-quality Si NW FETs for development of label-free electronic detection strategies for different bioassays. The common problems related to the top-down processes involved for the sensor fabrication and eventually their effect on the sensor performance were also discussed.

In order to use the developed sensors as label-free biosensors, the Si NW FETs were integrated with a specially-designed microfluidic platform, which facilitated a more controlled handling of analytes. The nanowires were firstly modified with ion-selective functional groups in order to determine the basic sensing performance of the devices in liquids, which will be discussed in the next chapter. Deploying as label-free biosensor, the Si NW FETs were successfully surface functionalized with PSA-specific and IL-4 specific receptor molecules. The properties of the Si NW ISFETs and their deployment as biosensors will be discussed in detail in the next chapters.

Chapter 4: Electrical characterization of Si NW ISFET devices and pH sensing*

The fabricated Si NW FETs were characterized electrically by operating them in a liquid gate configuration and are therefore referred as Si NW ISFETs. The transistors were characterized electrically to evaluate the required operating voltages and operating mode. In this chapter, the basic electrical characterization results of the Si NW ISFETs are shown. The variation in the transistor characteristics on a single chip and from chip-to-chip on the whole wafer is also discussed. Further, the Si NW sensors were functionalized with ion-sensitive molecules and thereafter used for proof-of-principle experiments such as pH sensing. The obtained sensitivity of the Si NW sensors to a variation in pH of the buffer solution is shown. The Si NW sensors were also connected to a portable measurement system in order to carry out real-time pH measurements. The merits of the sensors in terms of stability and reproducibility for long continuous measurement are also discussed.

4.1. Background information

The schematic for the operation of Si NW FETs in liquid gate configuration is shown in figure 4.1. On a single chip with dimensions of 10 mm × 7 mm, 32 Si NW

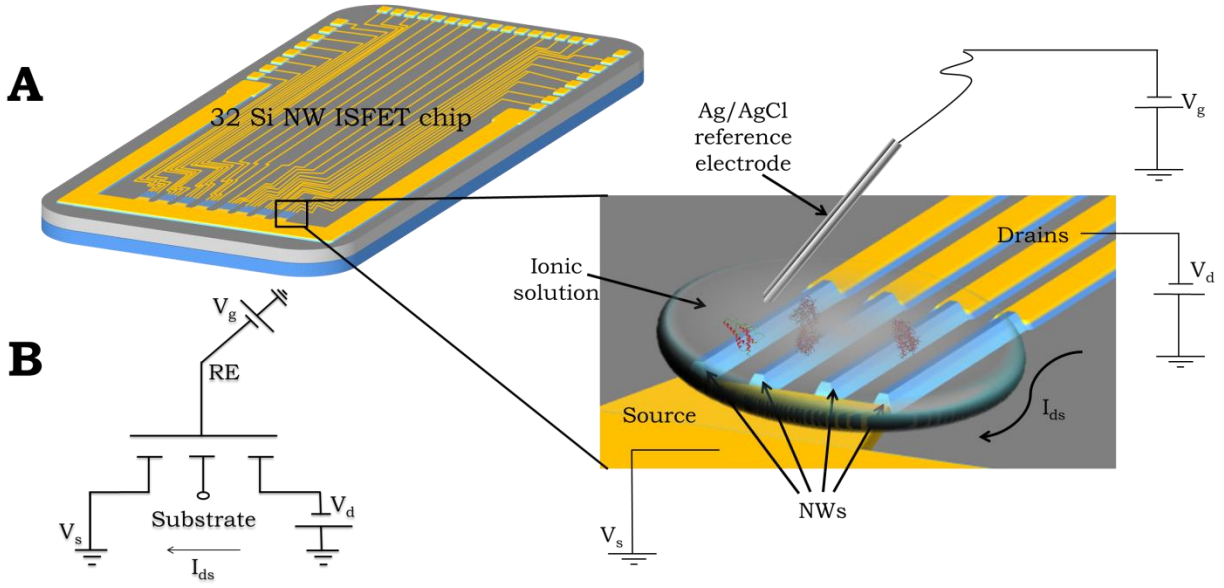

Figure 4.1 (A) Schematic of the Si NW ISFET chip with liquid gate configuration shown in the inset; and (B) Equivalent electronic circuit for the Si NW FET operation in liquid gate configuration.

* The results of this chapter are published in ACS Omega journal: D. Rani, V. Pachauri, A. Mueller, X. T. Vu, T. C. Nguyen, S. Ingebrandt; On the use of scalable NanoISFETs of silicon with highly reproducible sensor performance for assay based applications; ACS Omega 2016, doi:10.1021/acsomega.6b00014.

ISFETs are arranged with a common source and individual drain electrode configuration (figure 4.1 A). For liquid gate operation, the source electrode was grounded while a small negative voltage was applied to the drain electrode as it is shown in the inset in figure 4.1 A. An external reference electrode suspended in the electrolyte solution over the gate oxide covering the Si NW was used to apply the gate-source voltage (V_{gs}). The current was measured between the drain and source electrodes, called drain-source current (I_{ds}). The equivalent electronic circuit for the Si NW ISFET operation is shown in figure 4.1 B, where the bulk Si substrate is shown as floating (optional).

4.2. Basic electrical characterization of the Si NW ISFETs

The Si NW ISFETs were characterized electrically using a Keithley semiconductor parameter analyser (Keithley 4200) and probe station to find the range of operating voltages and the mode of the NW transistors operation. The transfer and output characteristic measurements of the Si NW ISFET devices were carried out by operating the transistors in a 3 electrode configuration. An external Ag/AgCl reference electrode was suspended in 10 mM PB (pH 7.4) over the Si NW surfaces.

For the transfer characteristic measurements, the drain-source current (I_{ds}) was measured as a function of gate-source voltage (V_{gs}). The gate-source voltage was swept between 0 to -2 V at different drain-source voltages applied in steps of 0.25 from 0 to -1 V, as is shown in figure 4.2 A. For the output characteristic measurements shown in figure 4.2 B, the drain-source current was measured as a function of drain-source voltage. The drain-source voltage was swept between 0 to -2 V at different gate-source voltages applied in steps of 0.25 V from 0 to -1 V. From the transfer and output characteristic measurements, a p-type enhancement mode behaviour of the Si NW ISFETs was observed. This can be explained from the partial depletion of charge carriers in the Si NW FET due to the positive fixed charges in the gate oxide. The threshold voltage, V_{th}, was calculated by implementing the commonly used transconductance (g_m) extrapolation method, where the first derivative of the drain-source current (i.e., dI_{ds}/dV_{gs}) is plotted as a function of V_{gs} [159]. The threshold voltage, V_{th}, is given by the gate-source voltage axis intercept of the linear extrapolation of the g_m-V_{gs} characteristics (as shown in figure 4.2 C) at its maximum slope point and was in the order of V_{th} = -0.56 V for our devices.

As can be seen in figure 4.2 B, there was no current flow (majority charge carriers-holes) for gate-source voltages below the threshold voltage V_{th} = -0.56 V. For a gate-source voltage above the threshold voltage ($V_{gs} > V_{th}$) and at low drain-source voltage ($V_{ds} < V_{gs}-V_{th}$), the variation in drain-source current with the drain-source voltage was linear. On the contrary, for higher drain-source voltages ($V_{ds} \geq V_{gs}-V_{th}$) the channel was pinched-off and the drain-source current was saturated. Additionally, the obtained source to source current-voltage relationship was linear as it can be seen in figure 4.2 D. This confirmed that the contact between the metal contact pads and doped Si contact lines was ohmic, which is important for a reliable sensor operation.

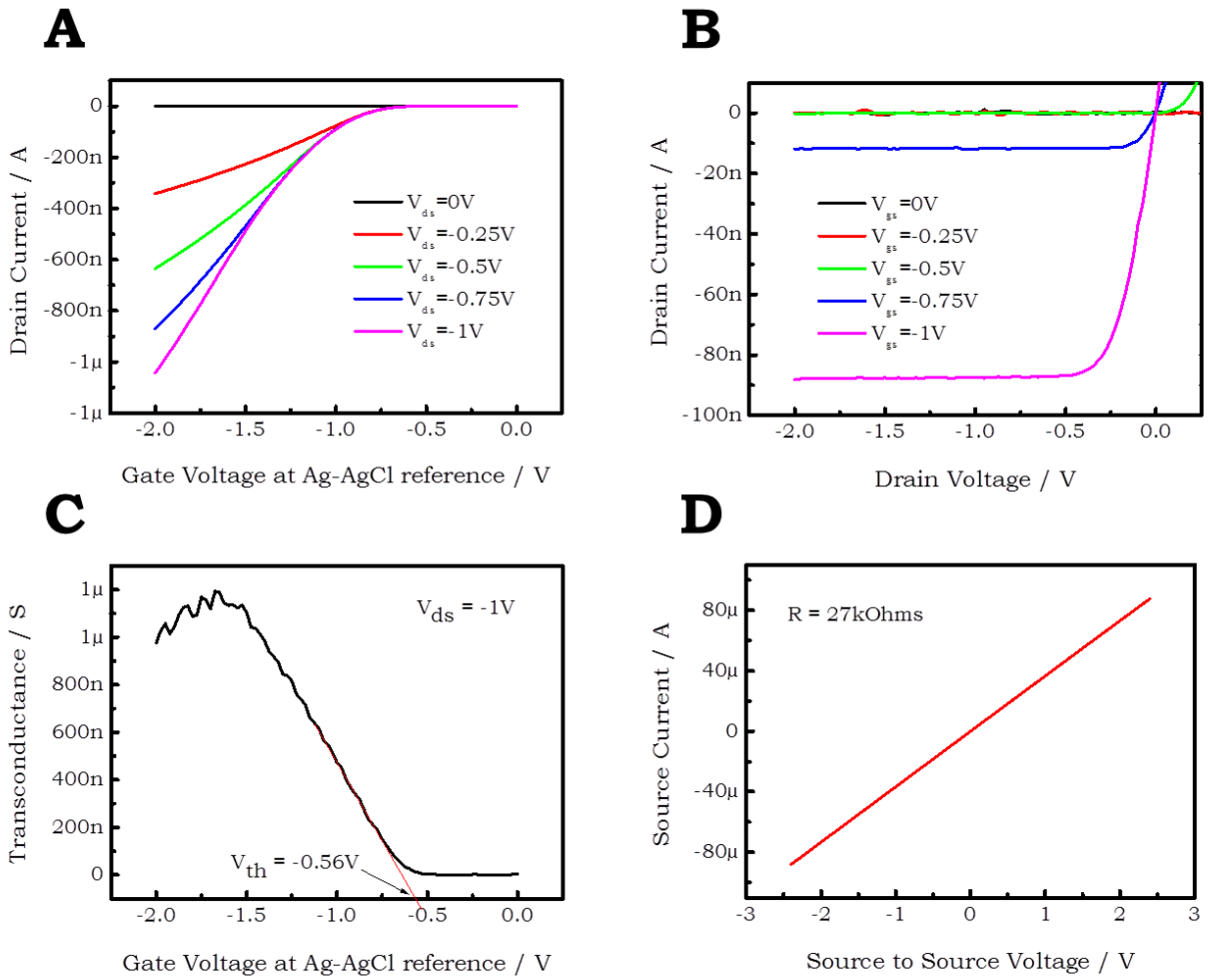

Figure 4.2 Electrical characterization of a Si NW ISFET: (A) Transfer characteristic where the drain-source current (I_{ds}) was measured as a function of the gate-source voltage (V_{gs}) with the drain-source voltage varying from 0 to -1 V in steps of 0.25 V; (B) Output characteristics where the drain-source current was measured as a function of the drain-source voltage (V_{ds}) with gate-source voltage varying from 0 to -1 V in steps of 0.25 V; (C) Transconductance as a function of gate-source voltage for a drain-source voltage of -1 V; and (D) Current between the two source electrode contacts of the chip showing that the contact between the metal contacts and the doped Si contact lines is perfectly ohmic.

4.3. Reproducibility check of the Si NW ISFETs

The threshold voltages of the Si NW ISFETs on a single chip and on different chips of a wafer were characterized in 10 mM PB at pH 7.4 (as it was described in the previous section). The transistors were measured before and after the GPTES silanization process (as described in section 3.3.1 of chapter 3). The variation in V_{th} of the ISFETs on a single chip and from chip-to-chip on a wafer was evaluated for verifying the reproducibility of the fabrication process. The extracted threshold voltages (V_{th}) of 54 Si NW ISFETs chosen from different chips on a wafer before and after the GPTES silanization is shown in figure 4.3 (left side). The V_{th} of the different Si NW ISFETs on a single chip is illustrated in figure 4.3 (left side) from ISFET no.1 to 25. The average V_{th} of the Si NW ISFETs on a single chip (figure 4.3, right side) before and

after the silanization was in the range of $V_{th,before}$ = -0.313 ± 0.024 V and $V_{th,GPTES}$ = -0.335 ± 0.025 V. This indicates that the Si NW ISFETs on a single chip have nearly-identical characteristics.

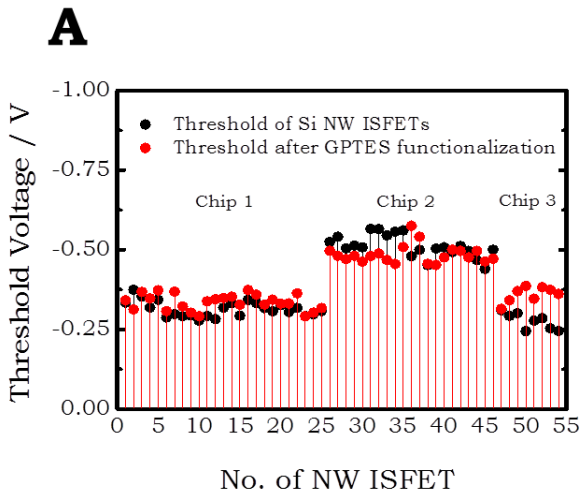

Condition / Chip	Average V_{th} (V) of Si NW ISFETs	Average V_{th} (V) of Si NW ISFETs after GPTES
Chip 1	-0.313 ± 0.024	-0.335 ± 0.025 ***
Chip 2	-0.511 ± 0.035	-0.485 ± 0.029 *
Chip 3	-0.276 ± 0.025	-0.359 ± 0.024 **

Figure 4.3 Extracted threshold voltage of 54 Si NW ISFETs chosen from three different chips on a wafer before (black) and after the GPTES silanization process (red) shown on the left side; and the corresponding average threshold voltage before and after the silanization process for three different chips shown in the table on the right side. The statistical analysis was done using a paired t-test (*** for P < 0.001, ** for P < 0.01 and * for P < 0.1).

When comparing the shifts in V_{th} for all 54 Si NW ISFETs one can see that the voltages shift sometimes into the positive and sometimes into the negative direction. This could be attributed to the local variations of the surface chemistry on the sensor devices. The statistical evaluation of the data was done using a paired t-test (test to determine if the mean difference between paired observations at a particular outcome is statistically different) and is shown in figure 4.3 (right side). When comparing the response of individual Si NW ISFETs to GPTES silanization, it can be seen that the V_{th} of some of the Si NW ISFETs decreases depending on the chip type. The variation in V_{th} of the Si NW ISFETs from chip-to-chip and as a response to the GPTES silanization (shown in figure 4.3) over the wafer, could also be due to the intrinsic limitations in the fabrication process deployed. The intrinsic limitations include variations in the effective channel lengths coming from the issues in the fabrication process such as the alignment problem between different lithography masks (described in section 3.1.4 of chapter 3). Other limitations could be variation in the dopant concentration during the implantation process, gate oxide thickness and fixed charges. Thus, these factors play an important role in determining the uniformity of the transistor sensor characteristics over the wafer and need to be precisely controlled in order to improve the reproducibility of the fabrication process.

4.4. pH sensing using Si NW ISFETs

To deploy the Si NW ISFETs for sensing applications, basic proof-of principle experiments such as pH sensing were done. For pH measurements, the Si NW ISFETs chips were silanized with APTES *via* the gas phase silanization method (as it was described in section 3.3.1 of chapter 3). The pH sensing mechanism is based on protonation and deprotonation of the hydroxyl groups at the gate oxide (SiO_2) surface of the Si NWs (described in detail in section 2.2 of chapter 2). After the gas phase silanization of the Si NWs with APTES there are both -NH_2 and Si-OH groups present at the solid-liquid interface, which have different densities and dissociation constants. At low buffer pH the amino group is protonated to NH_3^+ while at high buffer pH the Si-OH is deprotonated to –SiO^-.

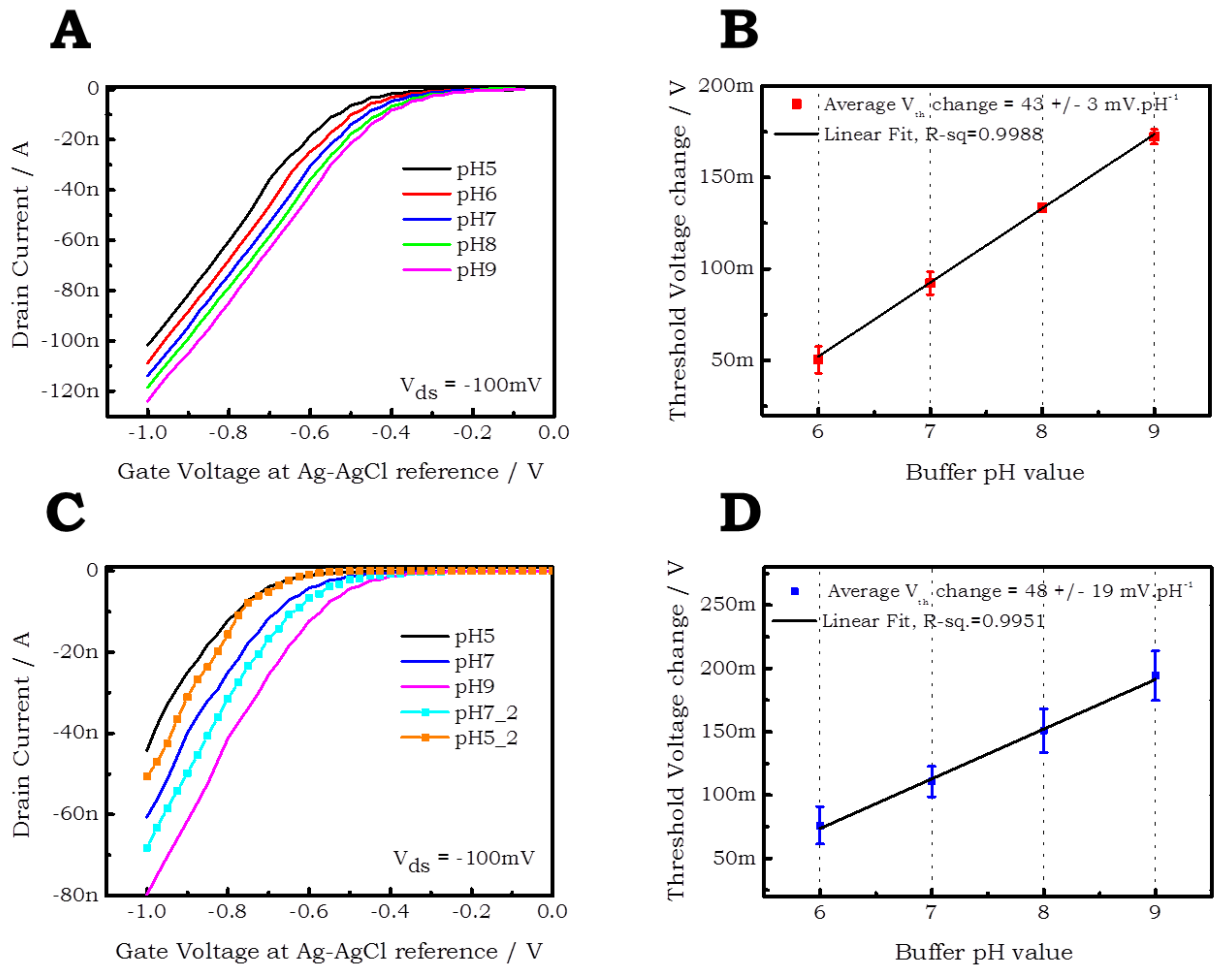

Figure 4.4 (A) Transfer characteristic curves of a Si NW ISFET with increase in pH (of 10 mM PB) from 5 to 9 at V_{ds} = -100 mV; (B) Change in threshold voltage plotted as a function of pH of the buffer solution with an average change of ΔV_{th} = 43 ± 3 mV/pH; (C) Transfer characteristic curves of a Si NW ISFET with increase and decrease in pH of the buffer from 5 to 9 and 9 to 5 at V_{ds} = -100 mV; and (D) Change in threshold voltage of a Si NW ISFET (from a different chip) plotted as a function of pH of the buffer solution with an average change of ΔV_{th} = 48 ± 19 mV/pH.

For the measurements, 5 different pH solutions 5, 6, 7, 8 and 9 of 10 mM PB were used. The transfer characteristics were measured by applying a small drain-source voltage, V_{ds} = -100 mV. The results are shown in figure 4.4 A. From the transfer characteristics, it can be inferred that the threshold voltage of the Si NW ISFETs decreased with increase in pH in accordance with the theory. The average change in threshold voltage calculated per pH using liquid gating measurements was, ΔV_{th} = 43 ± 3 mV. It can also be seen from the graph between ΔV_{th} and pH shown in figure 4.4 B, that the relationship is linear. The obtained pH sensitivity with Si NW ISFETs is comparable to other ISFET-based platforms reported in literature. It is known that the pH response of ISFETs with bare SiO_2 surfaces is in the order of 34 mV/pH and it may increase up to 45 mV/pH, with the modification of the gate oxide surface with functional molecules such as APTES [79, 114, 142].

Though high sensitivities for pH measurements were obtained with the Si NW ISFETs, the variation in response from chip-to-chip on a wafer was evaluated in order to know the reproducibility of the fabrication process. From figure 4.4 D it can be deduced that the average change in V_{th} with pH of ΔV_{th} = 48 ± 19 mV/pH for a different Si NW chip was much higher. This variation in pH response from chip-to-chip could be related to the intrinsic limitations in the fabrication process and the non-uniform surface activation and modification as reported in the previous section.

Moreover, the hysteresis in the response of Si NW ISFETs for pH was also characterized and it is shown in figure 4.4 C. The transfer characteristics were measured with increase (pH 5, pH 7 and pH 9) and decrease in pH (from pH 9, pH 7_2 and pH 5_2) of the buffer solution. It can be inferred that the V_{th} decreases with increase in pH and vice versa. However, when the pH of the buffer solution is increased and decreased, the transfer characteristic curves at the same pH value (pH 7 and pH7_2, pH 5 and pH 5_2) do not overlap with each other. This could be due to imperfect process of changing the pH solutions in our measurements. This effect is known as electrochemical hysteresis and it is highly influenced by the method of pH solution exchange and surface effects at the liquid-solid interface [112].

To deploy the sensors for POC applications, real-time pH measurements as conceptual tests were carried out using a portable hand-held readout system. With our portable setup, 4 NW ISFETs can be measured simultaneously [32, 142]. The portable measurement setup is shown in figure 4.5 A, where the Si NW ISFET chips were wire bonded on to a PCB carrier (described in section 3.2.1 of chapter 3). An external Ag/AgCl reference electrode was immersed in to the buffer solution within the PDMS fluidic layer on top of the Si NWs.

The portable measurement setup was developed in our research group in a parallel PhD thesis work. It was built around a 32 bit PIC microcontroller with user friendly Labview software to record and display the electrical measurements on a computer screen [142]. The real-time measurements were carried out at maximum sensitivity of the devices.

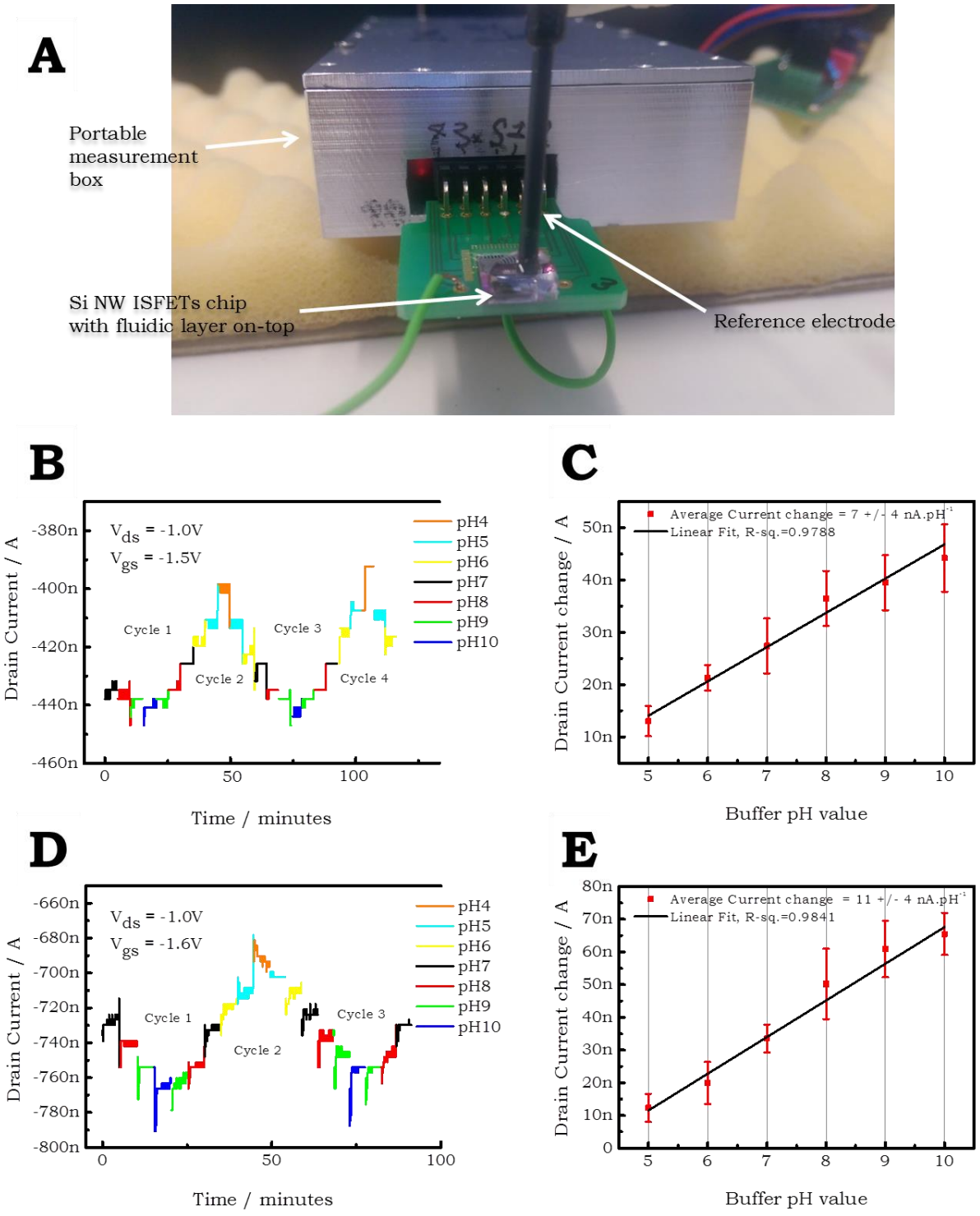

Figure 4.5 (A) Picture of a portable Si NW ISFET measurement system with a sensor chip and an external reference electrode immersed in the buffer solution over the Si NW; (B,D) Real-time pH measurements with two different Si NW ISFET chips, where the drain-source current was measured as a function of time and the pH of the buffer solution was changed from 4 to 10 in multiple cycles; and (C,E) Average change in the drain-source current as a function of the buffer solution pH for two different Si NW ISFET chips.

For this the V_{gs} with maximum transconductance value at a fixed drain-source voltage, V_{ds} = -1 V was chosen. The drain-source current was then measured as a function of time with pH of 10 mM PB changed in 4 to 10 in multiple cycles. As illustrated in figure 4.5 B and C, the drain-source current of the Si NW ISFET was measured at fixed gate-source voltage, V_{gs} = -1.5 V. The average change in the drain-source current with pH was in the order of, ΔI_{ds} = 7 ± 4 nA/pH.

On changing the pH of the buffer solution in multiple cycles from low to high and high to low, it was observed that the response of the Si NW ISFETs was reproducible and the NW sensor remained stable for long working hours. However, the drain-source current values were not same at the same pH in different cycles. This could be due to the imperfect changing process of the pH solutions as described in the previous section.

Moreover, a comparison of the response of the Si NW ISFET from two different chips shown in figure 4.5 B, C and 4.5 D, E, respectively was also carried out. From figure 4.5 D and E, it can be seen that the average change in drain-source current was higher, ΔI_{ds} = 11 ± 4 nA/pH (for V_{gs} = -1.6 V, V_{ds} = -1 V), than the one described earlier. Thus, the sensor response varies from chip-to-chip and could be due to the intrinsic limitations in the fabrication process.

4.5. Conclusion

In conclusion, a thorough electrical characterization of the “top-down” fabricated Si NW ISFETs was done in liquid gate configuration using a Keithley semiconducting parameter analyser and a probe station. The NW transistors while operated in a liquid gate configuration showed p-type enhancement mode transistor characteristics with nearly-identical device characteristics on wafer-scale. In addition to that, a slight variation in the sensor characteristics from chip-to-chip over the wafer was evaluated and correlated with the intrinsic limitations in the fabrication procedure when combining NIL and optical lithography.

To deploy the transistors for sensing applications, basic proof-of-principle experiments such as pH measurements were carried out. On evaluating the threshold voltage for each pH buffer, typical SiO_2 sensitivities were achieved with an average change in threshold voltage of ΔV_{th} = 43 ± 3 mV/pH. Further, on measuring the sensors continuously for long hours using a portable measurement setup, stable and reproducible sensor characteristics were obtained. Statistical variations in the responses were attributed to differences in the chemical treatment of the surfaces and to imperfect solution exchanges during pH measurements. It is to be noted that statistical evaluation of many sensors on a chip over several independent experiments is necessary to extract meaningful result from a bio/chemical assay. In summary our “top-down” fabricated Si NW transistors showed sensitive, stable and reproducible characteristics. The usage of these devices for biomolecule sensing is discussed in the following chapters.

Chapter 5: Detection of PSA by electronic and optical methods using Si NW ISFETs*

As a central part of this thesis work, the Si NW ISFET sensors were deployed for label-free detection of prostate cancer (PCa) biomarker, "Prostate specific antigen (PSA)". This chapter gives an overview on the state-of-art of the PCa screening methods. The importance of PSA as a standard biomarker is also discussed.

A new receptor-analyte combination was used for the detection of PSA using highly reproducible Si NW sensors. Here, PSA-specific DNA aptamers were used as receptors for PSA as an analyte. The aptamer-PSA immobilization was initially optimized on conventional Si μ ISFETs and then the immobilization protocol was transferred onto the Si NW ISFETs. The aptamers were covalently immobilized onto the Si NW surfaces and thereafter the potentiometric detection of PSA binding was carried out. The achieved detection range for PSA using our Si NW ISFETs is discussed in this chapter. The merits of Si NW ISFETs against μ ISFETs towards detection of PSA are also reviewed. Further, the variation in the sensor responses on site-specific immobilization of aptamers over the Si NW sets is also described. Moreover, the issues that occur on obtaining two different sets of PSA and their effect on the response of the sensors are studied.

The detection of PSA by the above-described method was also confirmed by optical detection methods as a reference. The binding of PSA to the aptamer-functionalized Si NW surfaces was confirmed by chemiluminescence and fluorescense methods in which specific secondary antibodies were used. The NW transistors were also integrated with a PDMS-based microfluidic structure, for controlled handling of the biomolecules during the optical detection. The tested detection range for PSA and the merits of the detection methods in terms of specificity are also discussed

5.1. Prostate cancer and diagnosis

PCa occurs when the rate of cell division is higher than that of the cell death leading to uncontrolled tumour growth [160-161]. Most of the PCa's are adenocarcinoma's (95%), which arise from the prostatic epithelial cells that make and release seminal fluid. PCa mainly occurs in older men with 65% cases reported in the age group ≥ 65 years. With time, the abnormal growth advances into a noticeable malignant form and

* The results of this chapter are submitted for publication (September 2017): D. Rani, V. Pachauri, N. M. Srinivasan, P. Jolly, P. Estrela, V. Chu, J. P. Conde, X. T. Vu, S. Ingebrandt; Silicon nanowire ion-sensitive field-effect transistor-based biosensor towards electronic and optical detection of prostate specific antigen.

can be classified into four different stages - I, II, III and IV using Gleason's score method after biopsy examination. In stage I and II, the cancer is localized in the prostate gland, whereas in stages III and IV, it spreads to other organs such as bladder, bone, liver, etc. There are no symptoms evident in stage I, however these appear as the disease progresses to further stages. As the disease progresses to stage IV, the patient's 5-year survival rate significantly decreases (< 27%) [162].

Current early screening methods for PCa include testing of PSA levels in blood serum combined with Digital Rectal Examination (DRE) to examine the prostate texture and size [162]. These methods are not sensitive enough and the patients normally need to undergo Trans Rectal Ultrasonography (TRUS). With TRUS it is possible to obtain visual information of the gland to conduct instant, later biopsies to guarantee a reliable and accurate diagnosis. However, biopsies are painful and they carry a potential risk of infections due to migrated microbes from the rectum, which can result in prostate gland inflammation.

The PSA molecule is a 33 kDa single-chain glycoprotein produced by the epithelial cells of the prostate gland. It helps to keep the semen in a liquid state and also escapes in the blood stream. PSA test into blood serum is used as an acceptable standard worldwide for screening, diagnosing and monitoring of PCa [162]. It is a relatively inexpensive procedure and easily accepted by patients [163]. Two major forms of PSA are tested in the blood, which include free PSA (fPSA) and total PSA testing. The major form of detected PSA is complexed with the serine protease inhibitor, alpha-1-antichymotrypsin (called as total PSA), while the other form is uncomplexed or free PSA. fPSA and PSA are the only two assays approved by the US Food and Drug Administration for PCa testing. Patients with a PSA level above 4 ng/ml in blood serum are considered to be at the risk of PCa and are recommended to undergo further tests such as TRUS and biopsy [164]. Although PSA testing in blood serum is more common, its levels are also tested in other body fluids such as urine and semen [89, 154, 162].

Increased levels of PSA, however, could also be due to a noncancerous enlargement of the prostate gland (called as benign prostatic hyperplasia) as well as urinary tract infections. Moreover, PSA levels in blood are age dependent. For men below 50 years, the normal PSA level is less than 2.5 ng/ml and for men above 59 years, the normal PSA level is less than 4 ng/ml [165]. Thus, relying on a PSA test alone can result in ambiguity in diagnosing a PCa. Here, the need of a prostate biopsy is determined by the age-specific PSA level together with DRE result. The presence of other risk factors such as age and ethnicity are also considered.

Several other blood serum-based and urine-based biomarkers specific to PCa are under development [162]. In order to overcome the problems related to conventional screening methods for PCa, a sensitive detection technique needs to be developed, where other biomarkers in addition to PSA can be tested, simultaneously. For an early

diagnosis, detection of biomarkers associated with different stages of the disease pathogenesis is required [97].

In recent years, nanotechnology-based detection platforms such as electrochemical, plasmonic and mechanical, etc. have gained interest among researchers, because of their high specificity, sensitivity and label-free mode of detection. Within these, nanoscale, Si FET-based biosensors also called nanoISFETs (e.g., Si NW ISFETs) are in forefront, because of the well-known properties of Si and its methods available for mass-fabrication [3, 166-169]. Many microfluidic integrated Si NW transistor biosensors were reported in the last years for the detection of PSA by immobilizing PSA-specific antibodies as receptors [76, 128, 170]. For instance, Zheng and co-workers reported multiplexed, real-time and highly sensitive detection of PSA using n- and p-type Si NW FETs [97]. Recently, the usage of DNA aptamers as receptors has become popular, because of their low-cost availability and thermal stability in comparison to antibodies. DNA aptamers are artificial, single-stranded nucleotide sequences developed by an in-vitro selection procedure for a particular analyte [89]. For instance, Tzouvadaki and co-workers reported a Si NW transistors based, ultrasensitive, memristive aptasensor for the detection of PSA, where biotinylated anti-PSA aptamer molecules were used as the receptor layer on the Si NW surfaces [171].

The details of PSA detection using the Si NW ISFET biosensors of this thesis work by covalent immobilization of PSA-specific DNA aptamers *via* both electronic and optical methods are given in the following sections.

5.2. Electronic - potentiometric detection of PSA

Two kinds of Si ISFETs – Si μ and NW ISFETs sensors were used for the PSA assays in this thesis work. Main difference between these sensors is the largely different surface area, which lead to the biosensor response. The fabrication of the p-type Si μ ISFET chips was described earlier in other works of our group [142, 172-173]. Briefly the fabrication process consisted of a strong implantation of the source and drain contact lines (defined by photolithography on a lowly doped, n-type Si wafer) with boron ions, while keeping the gate area undoped. The whole wafer surface was passivated against the electrolyte solution with an oxide-nitride-oxide stack and a 10 nm thin SiO_2 gate oxide was formed by dry thermal oxidation. For ohmic contact formation, Al metal was deposited at the bond pads. A picture of an encapsulated Si μ ISFETs chip is shown in figure 5.1 A. The Si μ ISFET chip measuring 2.5 mm by 5 mm consisted of two columns of 4 transistors with 200 μm spacing. The ISFETs were arranged in a common source and separate drain layout in order to be used in a dip-chip configuration with typical gate dimensions of 16 μm in width and 7 μm in length. The microscopic image of one μ ISFET is shown in figure 5.1 B. The fabricated μ ISFETs, when characterized in liquid gate configuration, showed a p-type, enhancement-mode transistor characteristics.

The Si NW ISFET chip used in this work consisted of 32 Si NW ISFETs arranged in 8 sets of four Si NWs with a common source and separated drains. The fabrication and electrical characterization of the Si NW ISFETs chips was described in detail in chapter 3 and 4 of this thesis.

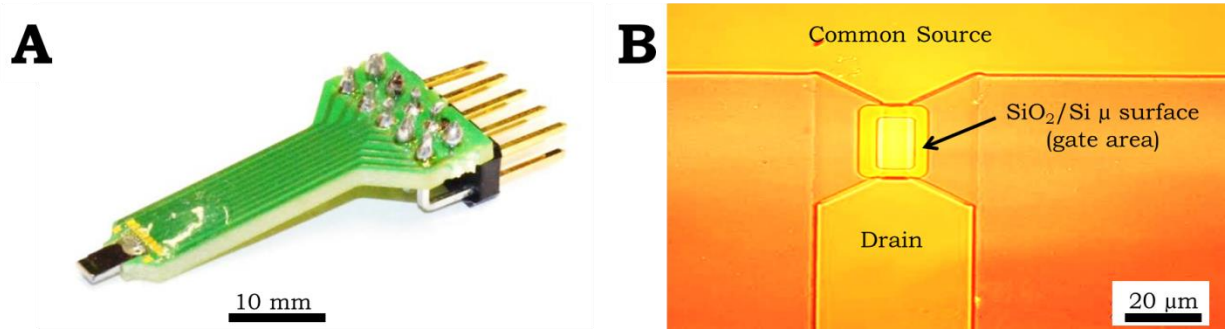

Figure 5.1 (A) A picture of an encapsulated Si μ ISFETs chip; and (B) Optical microscopy image of one μ ISFET consisting of a common source electrode, one drain electrode and a gate area.

The different steps in the immobilization of the aptamer sequence and the PSA were described in section 3.3.2 of chapter 3 (described for Si NW ISFETs only, but the protocol applies for both μ / Si NW ISFETs). The immobilization steps are illustrated in figure 5.2.

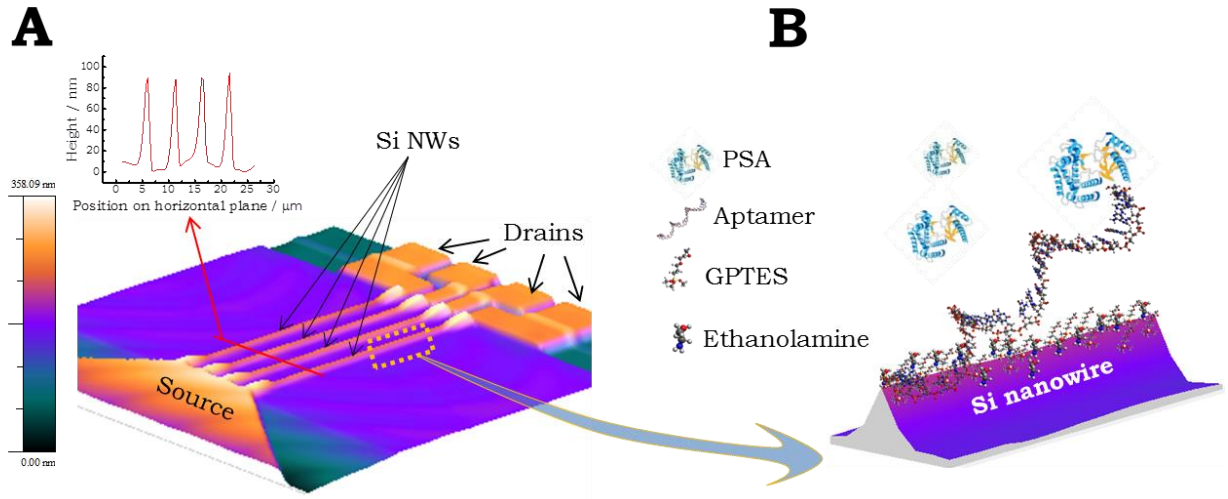

Figure 5.2 Schematics of the surface functionalization of Si NW ISFETs for PSA detection: (A) A 3D AFM image of one set of Si NW ISFETs with the height profile shown on the left top side; and (B) The Si NW surface was silanized with GPTES and immobilized with PSA-specific aptamers. The leftover GPTES sites were then blocked with ethanolamine. The binding of PSA onto the aptamer-functionalized Si NW surfaces resulted in a change in the conformation of the aptamers and thus the electronic detection was carried out.

The surfaces of the Si NWs were silanized with GPTES and covalently immobilized with PSA-specific aptamers. The leftover GPTES sites were then blocked using

ethanolamine. Thereafter, increasing concentrations of PSA were allowed to bind to the aptamer-functionalized Si NW surfaces. The binding of PSA to the aptamer-functionalized Si NW surfaces resulted in a change in conformation of the aptamers and it was detected as a change in V_{th} of the Si NW ISFETs.

The transfer characteristic measurements of both Si μ as well as NW ISFETs were carried out in 10 mM PB at pH 7.4. An exemplary result after each surface immobilization step is depicted in figure 5.3 A, B, respectively. The binding events of different molecules (i.e., GPTES, aptamer, ethanolamine (EA) and PSA (different concentrations)) at the Si μ ISFET and Si NW ISFET surface were monitored, electronically.

At first, the aptamer-PSA immobilization protocol was optimized on the Si μ ISFETs chips and later the same protocol was applied for the Si NW ISFETs. The DNA aptamers carry a negative charge due to their phosphate backbone. Thus, the aptamer binding onto the silanized Si NW surface resulted in a decrease in the threshold voltage (V_{th}) of the p-type Si μ / NW ISFETs. This V_{th} decrease can be observed from the transfer characteristic curves of the μ and NW ISFETs shown in figure 5.3 A, B, respectively [142, 174]. Here, the exact configuration of the aptamers on the Si NW ISFET surface, which can be regarded as an almost wrapped around gate configuration and their position within/outside the Debye length (λ_D = 1 nm, in 10 mM PB) is difficult to access [32]. Therefore, the binding of the aptamers on the Si NW surface, thereby the change in V_{th}, was confirmed by analysing the changes in the Si NW height before and after the aptamer immobilization using AFM. The AFM images and the corresponding line plot for height analysis of a Si NW are shown in figure 5.4 A. It can be observed from the line plot that after the aptamer immobilization, the height of the Si NW increased. This confirmed the presence of the aptamers on the Si NW surfaces.

After the aptamer immobilization, the non-reacted GPTES sites on the Si NW surfaces were blocked *via* binding of EA. This step added an additional negative charge to the Si NW surfaces as well, resulting in a decrease in V_{th} (figure 5.3 A, B) [63, 175-176]. Thereafter 30 nM (1 μg/ml) PSA was allowed to bind to the aptamer-functionalized Si NW surfaces. From the scientific literature it is known that the PI of PSA can vary in a large range from pH 6.4 to 8 owing to the variable degree of glycosylation [128, 177-178]. Accordingly, the observed increase in V_{th} upon PSA binding to the Si NW surface at pH 7.4 can be explained by a positive charge addition onto the Si NW surface (figure 5.3 A, B). In our experiments the PI of PSA is expected to be higher than pH 7.4 as PSA is positively charged at pH 7.4. The binding of PSA to the aptamer-functionalized Si NW surfaces was also confirmed by AFM. The AFM images and the corresponding line plot for height analysis of one Si NW after aptamer immobilization and after 30 nM PSA reaction are shown in figure 5.4 B. It can be observed from the height profile, that there was an increase in the Si NWs height after PSA immobilization, which also confirmed the presence of bound PSA.

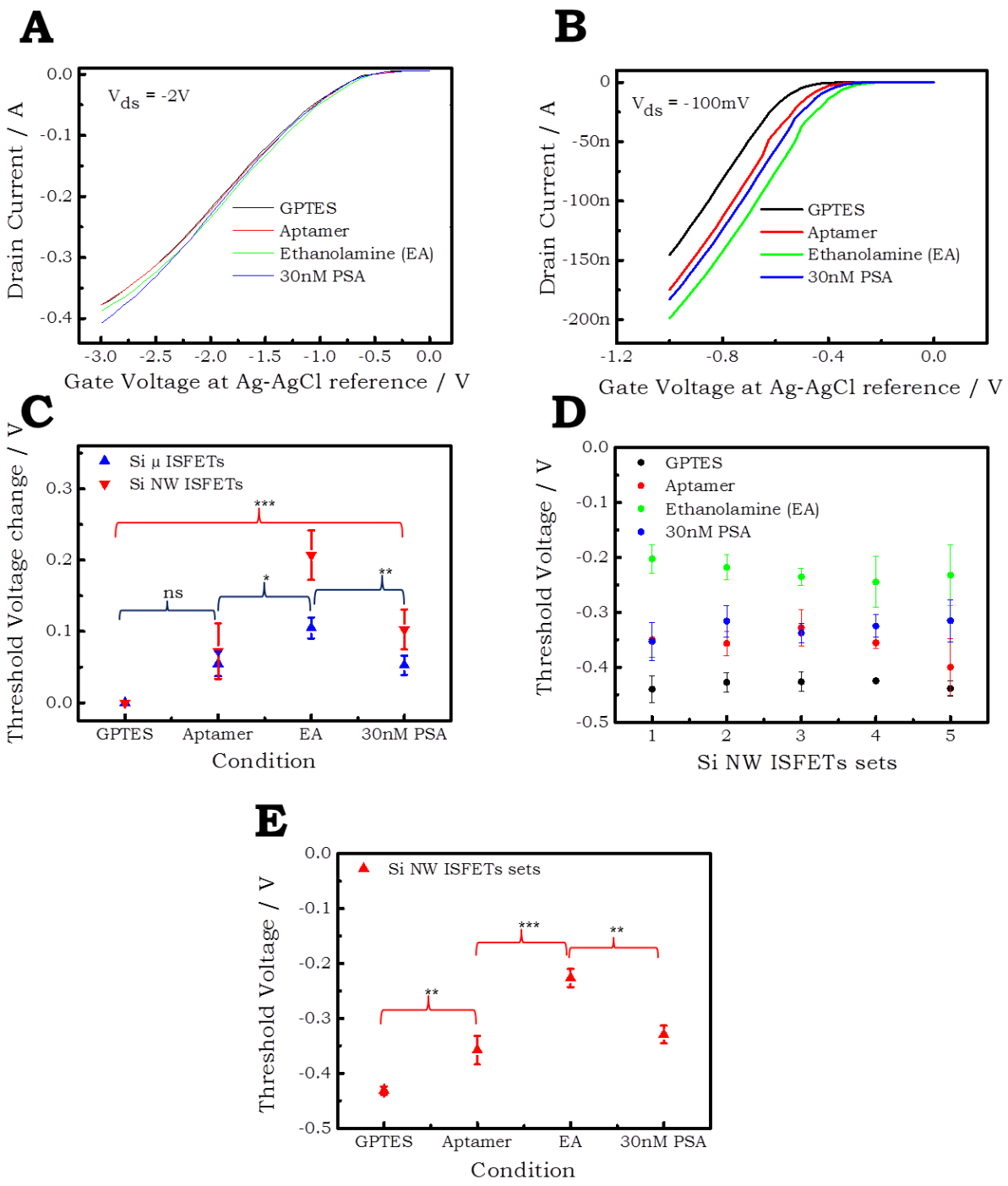

Figure 5.3 (A) Si μ ISFET transfer characteristic curves after the different immobilization steps (GPTES, aptamer, EA, 30 nM PSA); (B) Si NW ISFET transfer characteristic curves after the different immobilization steps; (C) Change in the V_{th} (with respect to GPTES) after each immobilization step for Si μ ISFETs (n = 2) and Si NW ISFETs (n = 18) shown as a scatter plot. The data was analysed using a paired t-test (ns for not significant, *** for P < 0.001, ** for P < 0.01 and * for P < 0.1); and (D, E) Variation in the V_{th} for different sets (composed of 4 Si NWs each) of Si NW ISFETs on a single chip after the different immobilization steps and the corresponding average V_{th}, both shown as a scatter plot. (note: n indicates the number of ISFETs)

Thus, from the transfer characteristics curves, in figure 5.3 A, B Si µ /NW ISFET show similar responses at different immobilization steps.

In addition to that, statistical analysis of the change in V_{th} after each immobilization step with respect to GPTES for Si µ and NW ISFETs was done using a paired t-test. From the scatter plot shown in figure 5.3 C, it can be observed that the change in V_{th} after each immobilization step was extremely statistically significant for Si NW ISFETs (*** for $p < 0.001$). On the other hand, the change in V_{th} for Si µ ISFETs was not significant after the aptamer immobilization step (ns for not significant). However, it was significant for ethanolamine blocking and 30 nM PSA reaction (** for $p < 0.01$ and * for $p < 0.1$). Thus, the change in V_{th} for the Si NW ISFETs was generally higher than that for the µ ISFETs. This difference could be because of the generally higher sensitivity of nanoISFETs (e.g., Si NW ISFETs) compared to conventional ISFETs (e.g., Si µ ISFETs) as it was reported in literature [179].

The variation in V_{th} of different sets of Si NW ISFETs at different immobilization steps (i.e., GPTES, aptamer, EA and 30 nM PSA) is shown in figure 5.3 D. The corresponding average V_{th} of Si NW ISFET sets is shown in the scatter plot in figure 5.3 E and it can be observed that the variation in V_{th} at each immobilization step was very statistically significant (*** for $p < 0.001$ and ** for $p < 0.01$). It can also be inferred that the standard deviation in V_{th} of different Si NW ISFETs sets increased after aptamer microspotting on the Si NW surfaces, in comparison to the standard deviation after GPTES immobilization. This could result from the variation in the aptamer density bound to the different Si NW sets, since the microspotted droplets are quickly evaporating while spotting from one Si NW set to another (an image after the microspotting process on the Si NW sets in shown in figure 5.4 C). This also increased the standard deviation of the Si NW ISFET sets in the consecutive immobilization steps of EA and 30 nM PSA. As it can be observed, the standard deviation in V_{th} of Si NW ISFET sets increased from 1.7% at GPTES ($V_{th\ at\ GPTES} = -0.43 \pm 0.01$) to 4.9% at 30 nM PSA immobilization step ($V_{th\ at\ PSA} = -0.33 \pm 0.02$). This was most likely due to the variation in the density of aptamers and PSA at different Si NW ISFET sets and needs to be improved further by optimizing the surface functionalization protocol.

The variation in V_{th} of different Si NW ISFET sets of two chips with aptamer microspotting and without microspotting (i.e., drop casting) was compared and the results are shown in figure 5.5. It can be seen in figure 5.5 A and B that the V_{th} of all Si NW ISFETs sets decreased after the aptamer immobilization by the microspotting technique. Similarly, the V_{th} of all Si NW ISFETs sets also decreased without microspotting, i.e., aptamer drop casting technique, as it is shown in figure 5.5 C and D. Moreover, the average change in V_{th} of all Si NW ISFET sets upon aptamers immobilization by both microspotting and drop casting techniques was comparable and statistically significant (*** for $p < 0.001$, ** for $p < 0.01$ and * for $p < 0.1$). This indicated that the variation in V_{th} of Si NW ISFET sets was not limited only to the

microspotting technique but also to the drop casting technique and needs to be further optimized by modifying the immobilization protocol.

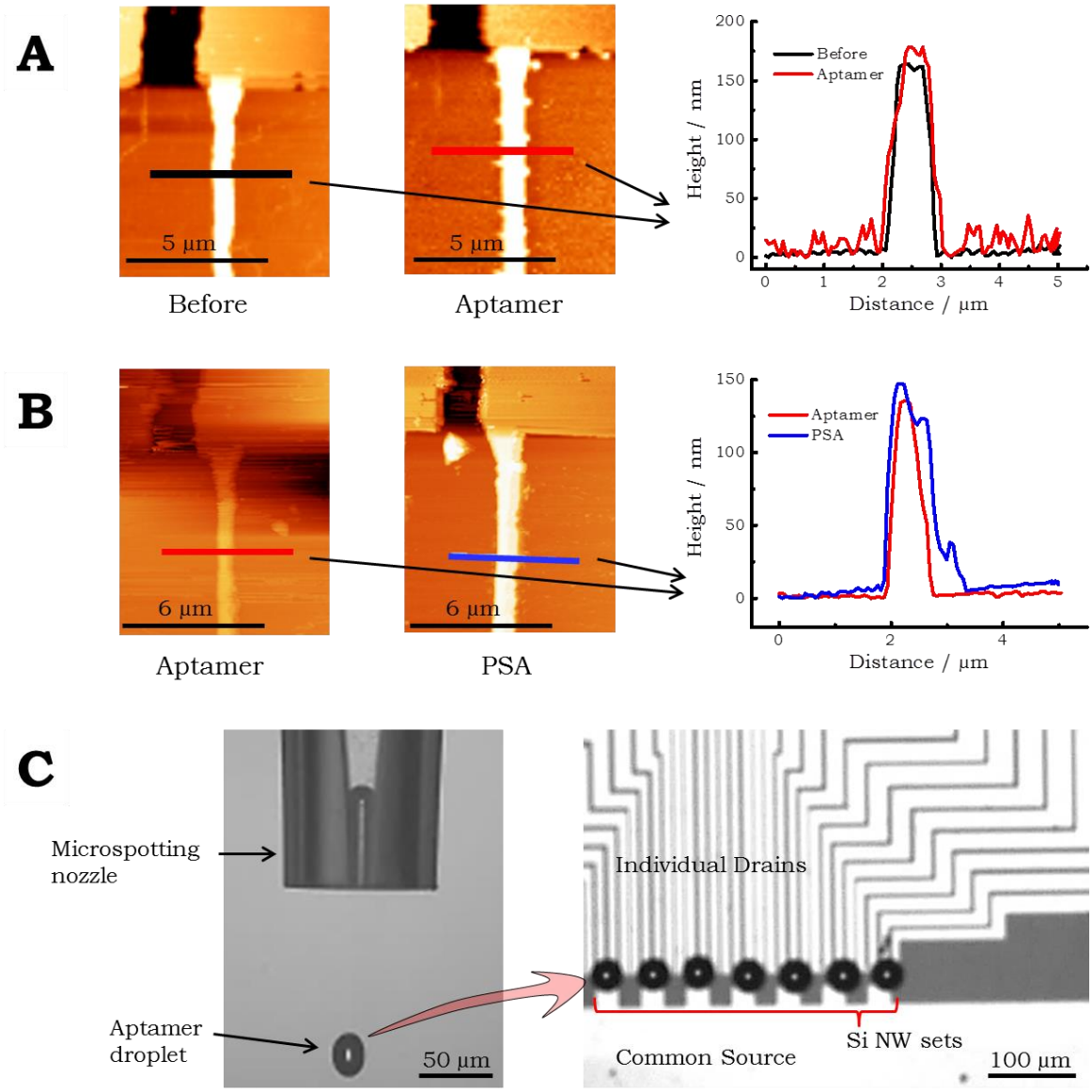

Figure 5.4 (A) Exemplary AFM image of one Si NW before and after the aptamer immobilization and the corresponding line plot for Si NW height analysis (right side); (B) AFM image of one Si NW after the aptamer and 30 nM PSA immobilization and the corresponding line plot for height analysis; and (C) Microspotting nozzle image with a DNA aptamer droplet and the Si NW ISFET chip image with microspotted aptamer droplets on the Si NW sets (right side).

In figure 5.6 A the variations in V_{th} of Si NW ISFETs on a single chip at different immobilization steps are shown. Some of the Si NW ISFETs (n = 1 to 20) were immobilized with PSA-specific aptamers while others (n = 21 to 32) were kept without aptamer (with PB) as a control in order to check the non-specific binding of PSA. The average V_{th} of Si NW ISFETs with aptamer and without aptamer at different

immobilization steps are illustrated in the scatter plot in figure 5.6 B. The V_{th} of Si NW ISFETs without aptamer (for n = 21 to 32) shown in figure 5.6 A, remained same as for GPTES and this can be observed clearly in the scatter plot for V_{th} shown in figure 5.6 B (ns for not significant). This indicated that the observed change in V_{th} (for n = 1 to 20) was specific to the presence of aptamers on the Si NW surfaces (*** for p < 0.001).

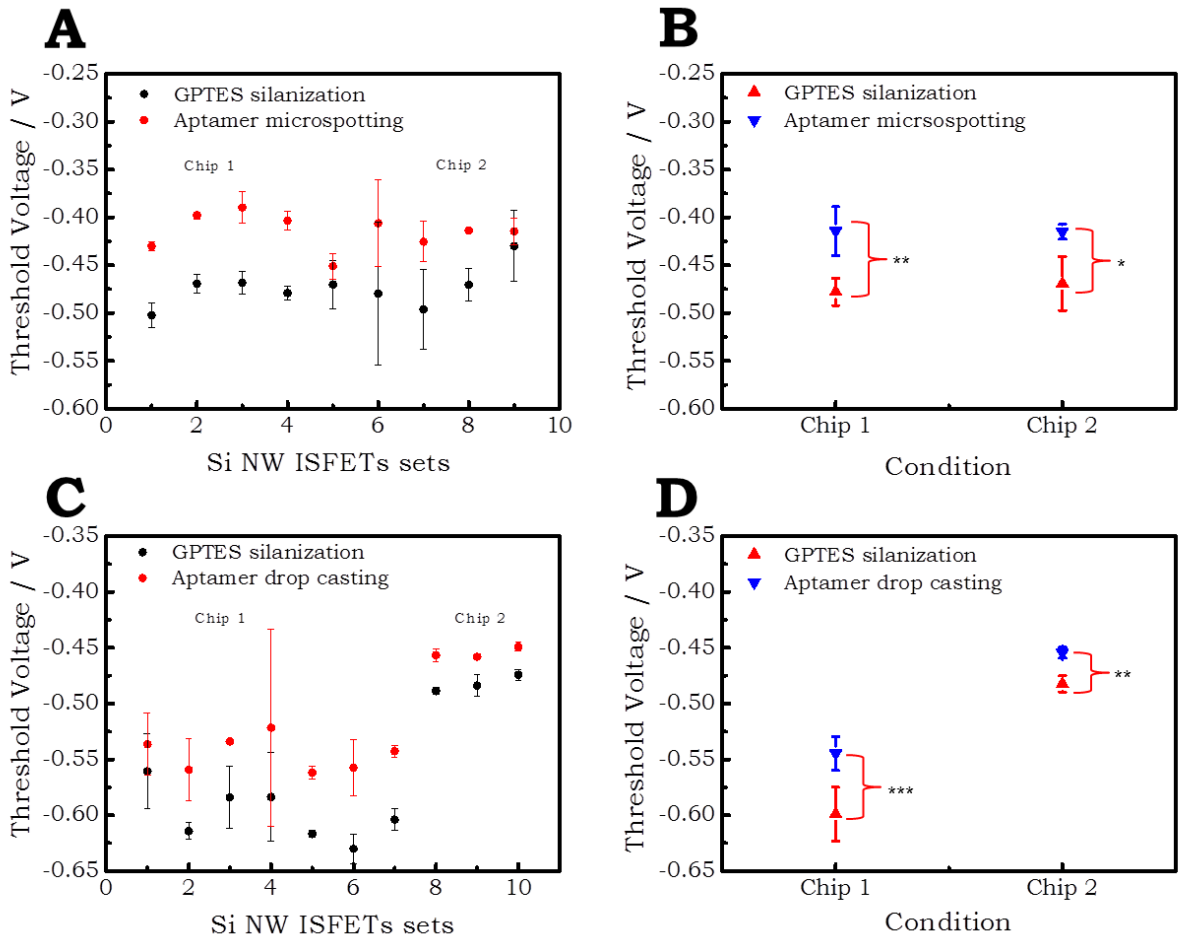

Figure 5.5 (A, B) Variation in V_{th} for different sets (n = 9) of Si NW ISFETs on two chips after GPTES silanization and after the aptamer microspotting process shown as a scatter plot. Average V_{th} of the Si NW ISFETs sets with GPTES and microspotted aptamer shown in the scatter plot (** for p < 0.01 and * for p < 0.1); and (C, D) Variation in the V_{th} for different sets (n = 10) of Si NW ISFETs on two chips after GPTES and aptamer drop casting (without microspotting) process shown as a scatter plot. Average V_{th} of the Si NW ISFETs sets with GPTES and drop casted aptamer shown in the scatter plot (*** for p < 0.001 and ** for p < 0.01).

As inferred from the figure 5.6 A and B, there is a larger change in V_{th} of Si NW ISFETs (*** for P < 0.001) with aptamer in comparison to Si NW ISFETs without aptamer (controls) to PSA binding, thereby indicating a specific binding of the PSA molecules to the aptamers.

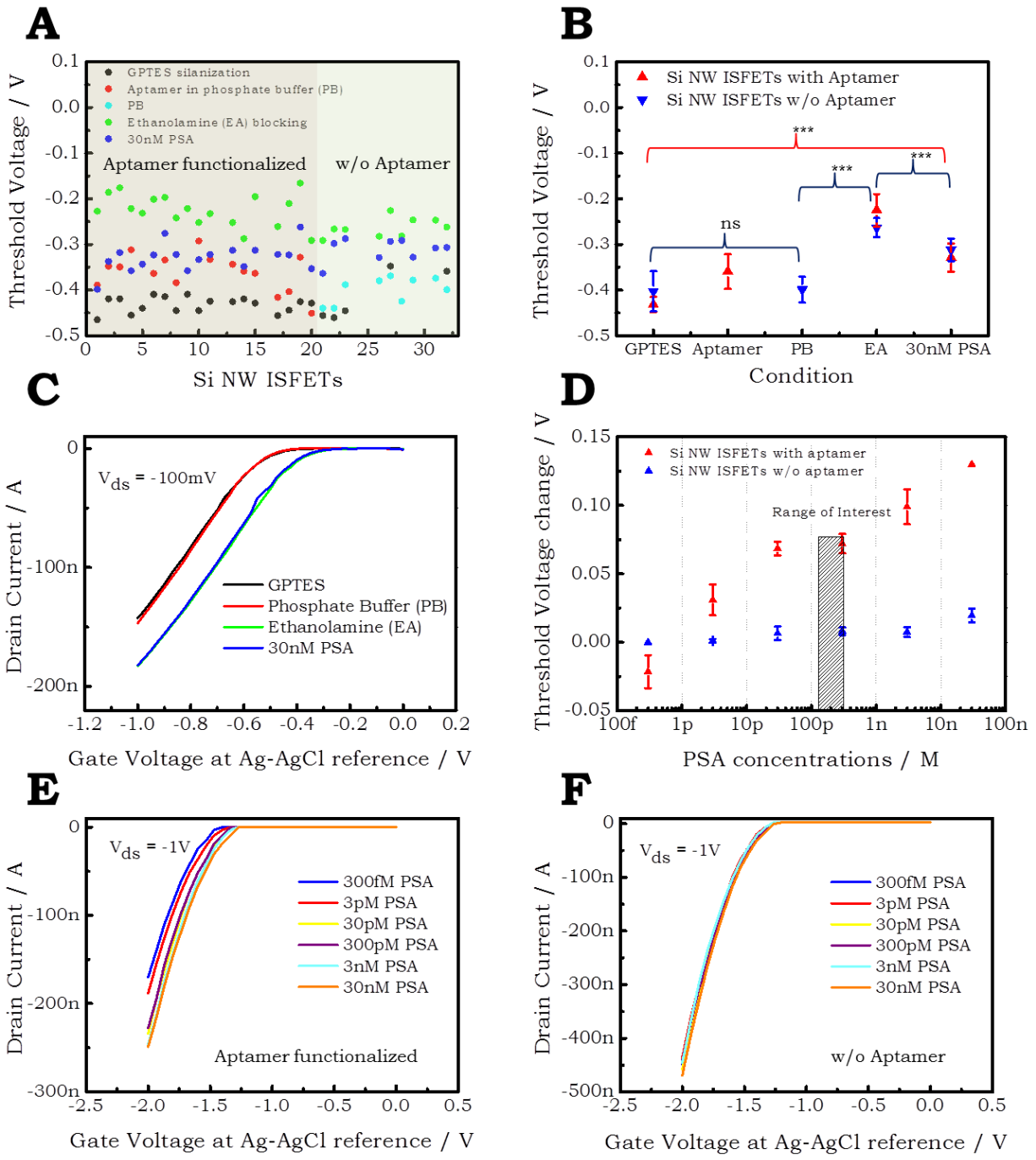

Figure 5.6 (A, B) Variation in the V_{th} of different Si NW ISFETs on an exemplary chip at different immobilization steps (i.e., GPTES, aptamer (n = 1 to 20) and PB (without aptamer) (n = 21 to 32), EA, 30 nM PSA) and the corresponding average, both shown in the scatter plot (ns for not significant and *** for $P < 0.001$); (C) A control Si NW ISFET transfer characteristic curves at the different immobilization steps; (D) The relative V_{th} change with respect to ethanolamine plotted as a function of PSA concentrations (a new stock solution) for two Si NW ISFETs with aptamer and without aptamer; and (E, F) Transfer characteristic curves at different PSA concentrations for a Si NW ISFET with aptamer and without aptamer, respectively.

For instance, the transfer characteristic curves of a Si NW ISFET used as control is shown in figure 5.6 C, where it can be seen that the change in V_{th} was clearly less for PB and PSA immobilization. Nonetheless, the change in V_{th} of some of the Si NW ISFETs upon PSA immobilization (figure 5.6 A) could be caused by non-specific binding of the relatively high concentration of PSA (30 nM). This is investigated further in the next paragraphs of this section.

Moreover, PSA concentration-dependent measurements were carried out with the Si NW ISFETs by monitoring the changes in V_{th} with increasing PSA concentrations. In figure 5.6 D, the changes in V_{th} (with respect to ethanolamine) as a function of increasing concentration of a new stock solution of PSA for two Si NW ISFETs with aptamer and without aptamer (control) are shown. For the Si NW ISFETs with aptamer, it can be seen that the V_{th} change increased with the increase in PSA concentration when tested in the range of 300 fM (1 pg/ml) to 30 nM (1µg/ml). In figure 5.6 E the transfer characteristic curves of a Si NW ISFET is shown with a new PSA stock solution and also here a clear concentration dependent shift in V_{th} was observed. However, the binding of this new PSA solution resulted in addition of negative charges onto the aptamer-functionalized Si NW surfaces and therefore, the PI of this PSA molecules should be below pH 7.4 [128, 177-178]. For the control Si NW ISFETs without aptamer (receptor) functionalization, the average change in V_{th} was negligible with increase in PSA concentrations from 300 fM to 3 nM. This can be clearly observed in the transfer characteristics curves of a control Si NW ISFET as shown in figure 5.6 F. There was a negligible shift in the curves with increase in PSA concentrations.

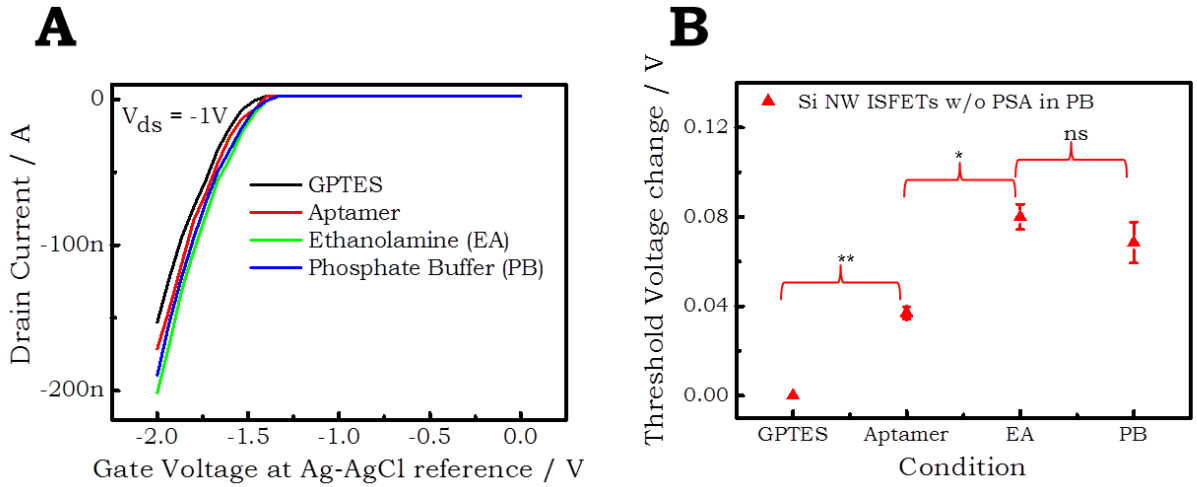

Figure 5.7 (A) Si NW ISFET transfer characteristic curves at different immobilization steps (GPTES, aptamer, EA, PB without PSA); and (B) The V_{th} change of two Si NW ISFETs at different immobilization steps shown in the scatter plot (ns for not significant, ** for $P < 0.01$ and * for $P < 0.1$).

However, at concentration levels above 3 nM a strong effect due to non-specific binding of the high PSA concentration can be seen. This non-specific binding of relatively high concentration of PSA was observed in on-chip control experiments as

well (shown in figure 5.6 A and B), however to a lesser extent. For real patient sample experiments the blocking protocol needs therefore be improved.

In another control experiment, the transfer characteristic curves of the Si NW ISFET chip were measured in the absence of PSA in order to check the stability of the sensor response in PB solution. From the transfer characteristic curves shown for an exemplary chip in figure 5.7 A it can be seen that there was no shift in the curves to pure PB solution (without PSA). In the scatter plot in figure 5.7 B summarizing all experiments the V_{th} changes at different immobilization steps (aptamer, EA, PB without PSA) with respect to GPTES are shown (ns for not significant, ** for $P < 0.01$ and * for $P < 0.1$).

For all the above cases, the calculation of V_{th} was done by implementing the transconductance (g_m) extrapolation method, where the first derivative of the drain-source current is plotted as a function of V_{gs} [32, 159].

Thus an electronic detection of PSA below the clinically-relevant range of 4 ng/ml was successful with the Si NW ISFETs.

5.3. Optical detection of PSA

A sandwich-based, optical immunoassay using the PSA-specific aptamers as receptors for PSA was done in order to confirm the electronic results of the aptamer-PSA assay. For this, the Si NW ISFET sensor chips were integrated with a microfluidic channel. Two different optical techniques namely chemiluminescence and fluorescence were used for the detection of PSA [143].

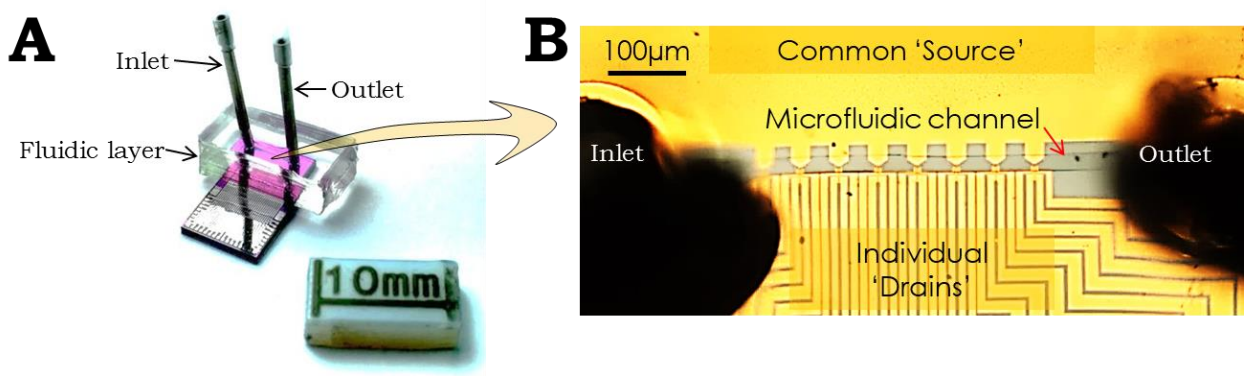

Figure 5.8 (A) A Si NW ISFET sensor chip with the straight channel (100 µm wide, 20 µm high and 4 mm long) PDMS microfluidic layer with metallic inlet, outlet and tubing; and (B) Microscopic image of the Si NW chip with the PDMS microfluidic channel.

The method of microfluidic integration of the chips and the protocol for the optical (chemiluminescence and fluorescence) detection was already described in sections 3.2.2 and 3.3.2 of chapter 3, respectively. The microfluidic channels were made out of PDMS, which were integrated on the Si NW ISFET sensor chips with metallic inlet, outlet and tubings as exemplary shown in figure 5.8 A. From the optical microscopy image shown in figure 5.8 B, it can be seen that the microfluidic channel was well

aligned along the Si NW area of the sensor chip. The schematics of the immobilization steps in the chemiluminescence assay are illustrated in figure 5.9 A and B.

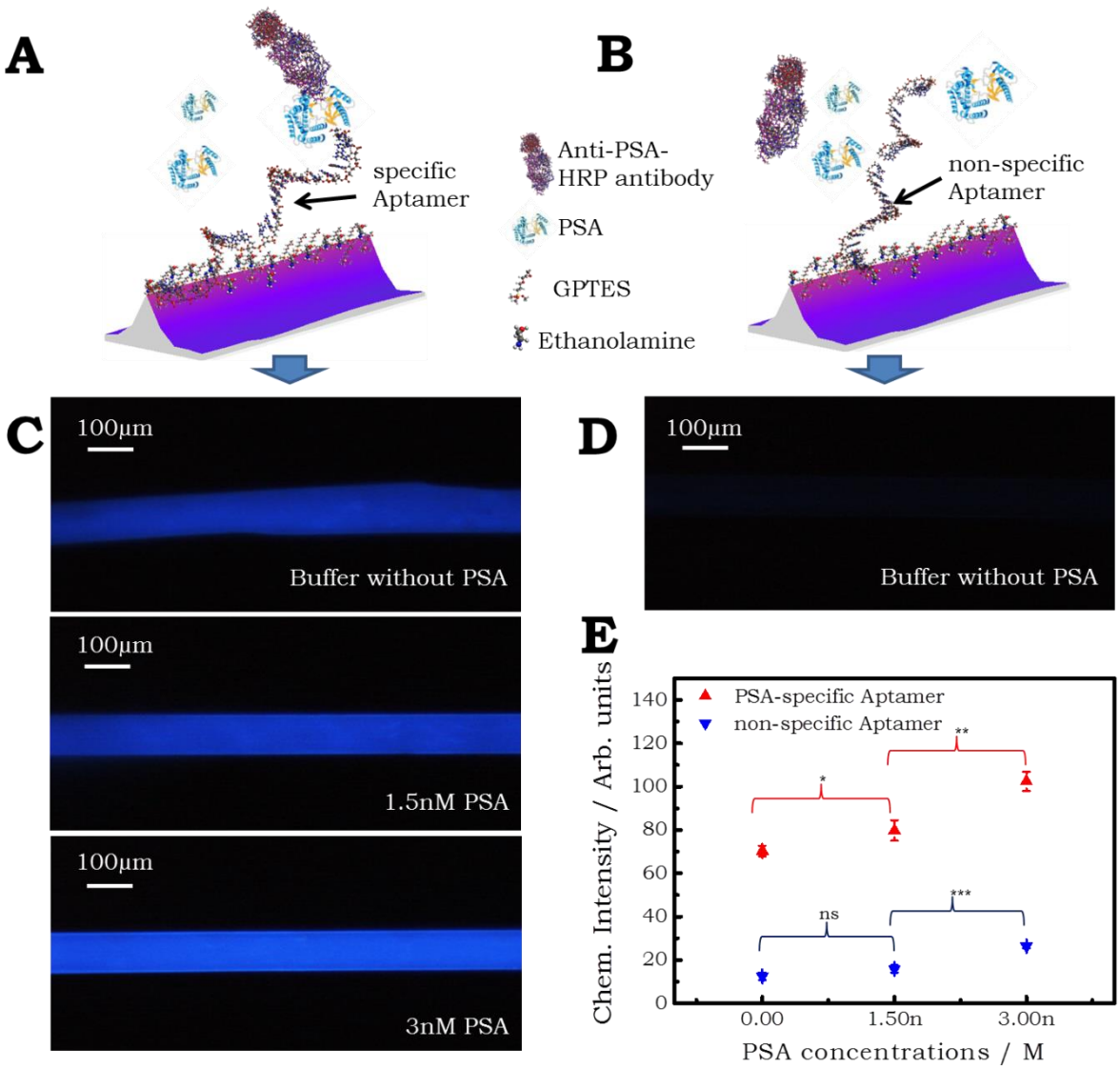

Figure 5.9 (A, B) Schematics for the functionalization of the Si NW surfaces in a chemiluminescence assay with PSA-specific and non-specific aptamers, respectively; (C) Optical microscopy image of the fluidic channels filled with luminol for different concentrations of PSA with PSA-specific aptamers as indicated in the pictures; (D) Optical microscopy image of the fluidic channel filled with luminol for buffer without PSA and with non-specific aptamers; and (E) Chemiluminescence signal intensity (arbitrary units) for the different concentrations of PSA with the non-specific aptamer (control) and PSA-specific aptamer sequence shown in the scatter plot (ns for not significant, *** for $P < 0.001$, ** for $P < 0.01$ and * for $P < 0.1$).

In the assay, the Si NW surfaces were functionalized with GPTES, PSA-specific aptamers, ethanolamine, PSA and anti-PSA-HRP antibodies as it is shown in figure 5.9 A. Thereafter, the luminol in the excited intermediate state was allowed to react with the anti-PSA-HRP antibodies bound on the Si NW surfaces. The luminol on reaction

with the HRP enzyme bound on the Si NW surfaces, returned to the ground state with an emission of a photon. This emission of a photon indirectly confirmed the presence of PSA molecules on the Si NW surfaces. In control experiments, the functionalization of PSA was carried out in the absence of PSA-specific aptamers. Instead, aptamers with a non-specific sequence were used. The immobilization steps for the control chips are illustrated in figure 5.9 B and consisted of GPTES, non-specific aptamers, ethanolamine, PSA and anti-PSA-HRP antibodies immobilization.

The optical microscopy images of the microfluidic channel for visual comparisons of the light intensities obtained upon flowing luminol for different concentrations of PSA are shown in figure 5.9 C. It can be clearly seen that the intensity of the chemiluminescence signal increases with increase in PSA concentration from 1.5 nM (50 ng/ml) to 3 nM (100 ng/ml). The signal intensity for binding of the anti-PSA HRP antibody unspecifically to the non-specific aptamer sequences was negligible as it is shown in figure 5.9 D. This indicated a negligible binding affinity of the anti-PSA HRP antibody to the non-specific aptamer sequences. In contrast to this the anti-PSA HRP antibody had a certain binding affinity to the PSA-specific aptamer sequence in the absence of PSA as an analyte. This can be deduced from the obtained chemiluminescence intensity in the microfluidic channel shown in figure 5.9 C. This could be further improved by modifying the blocking protocol. The variation in the chemiluminescence intensity as a function of different PSA concentration is shown in the scatter plot in figure 5.9 E (ns for not significant, *** for $P < 0.001$, ** for $P < 0.01$ and * for $P < 0.1$). It can be seen that the chemiluminescense intensity increases with the increase in PSA concentration. It can also be noted that the chemiluminescence intensity is much lower for the control chips with non-specific aptamer sequences in comparison with the PSA-specific aptamer. Thus, it indicates that the PSA binding to the PSA-specific aptamer is highly specific.

Furthermore, a second control experiment to check the presence of PSA on the Si NW chip surfaces was carried out using a secondary antibody labelled with a fluorescent dye. The schematics for the functionalization of the Si NW surfaces in the fluorescense assay is illustrated in figure 5.10 A. In the fluorescense assay, the Si NW surfaces were functionalized with GPTES, PSA-specific aptamers, ethanolamine, PSA and the detection was carried out using anti-PSA-FITC antibodies (i.e., a secondary antibody for PSA). The images were recorded with a fluorescence microscope. Two exemplary fluorescence microscope images of the microfluidic channels are shown in figure 5.10 A. It can be seen that the fluorescense signal intensity for the channel with 30 nM PSA concentration was higher compared to the channel without PSA. The corresponding intensities for all experiments are compared in the scatter plot shown in figure 5.10 B.

Thus, from these two optical sandwich immunoassays it can be confirmed that the PSA molecules and the amino-terminated aptamer binding is highly specific on the Si NW surfaces.

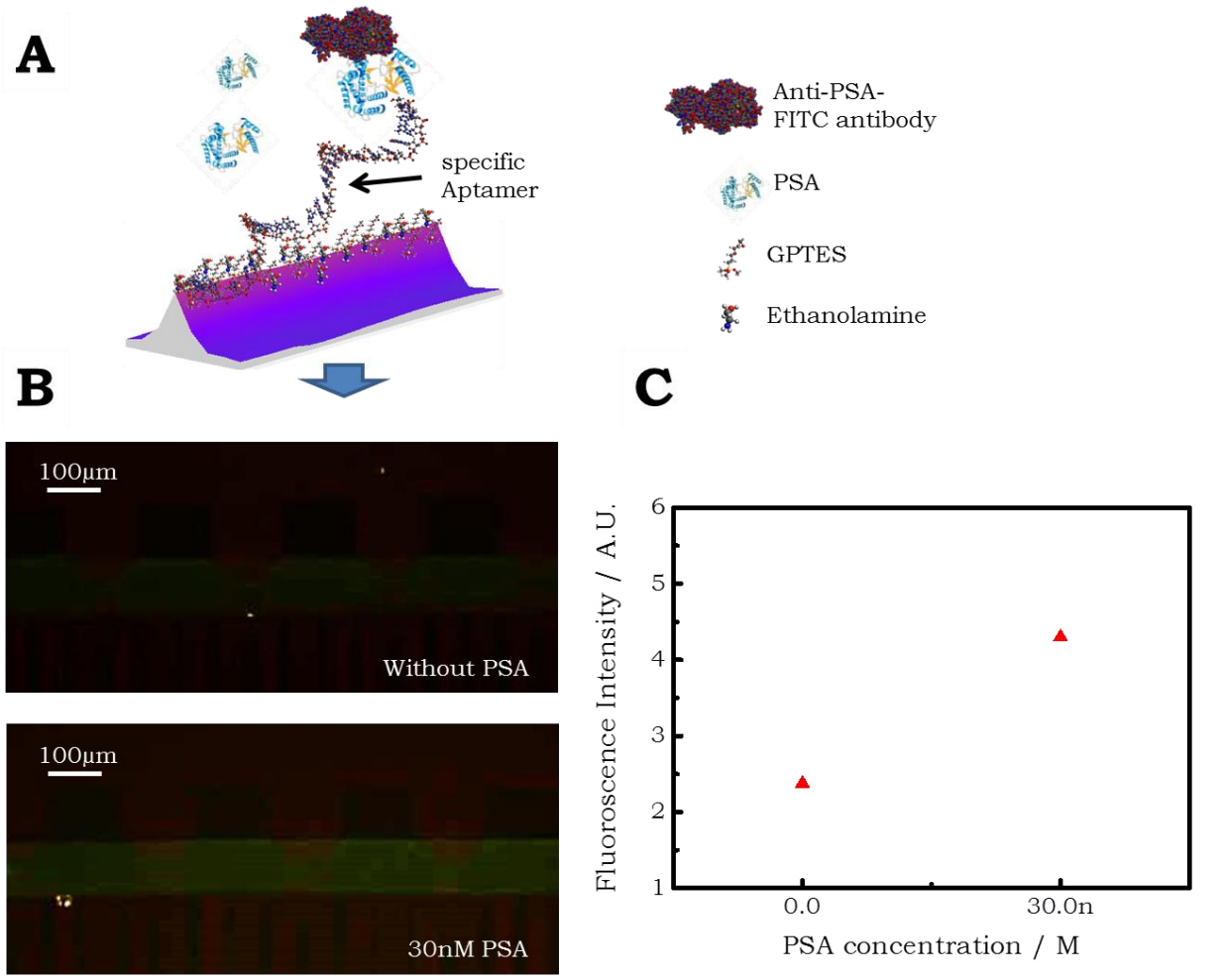

Figure 5.10 (A) Schematics for the functionalization of the Si NW surface in a fluorescence assay with the PSA-specific aptamers and an anti-PSA-FITC antibody; (B) Optical microscopy image of the microfluidic channel aligned to the Si NW ISFETs chip with 0 nM PSA and 30 nM PSA in the presence of the PSA-specific aptamers detected using a FITC labelled, anti-PSA, secondary antibody; and (B) Fluorescence signal (FITC) intensity with 0 nM PSA (control) and 30 nM PSA concentration shown in the scatter plot.

5.4. Conclusion

A very sensitive method to detect PSA molecules with Si NW ISFET sensors using site-specific, covalent immobilization of PSA-specific aptamers onto the Si NW surfaces was developed. When comparing the electronic responses of the Si µ ISFETs with the Si NW ISFETs the nano-sized transistor devices showed much higher sensitivities. Potentiometric measurements with the Si NW ISFET sensors functionalized with specific-aptamers as bio-receptor layer showed 300 fM (1 pg/ml) detection of PSA, which is clearly below the clinically-relevant range (4-10 ng/ml). In addition, the variation in the sensor response to microspotting and drop casting immobilization of the aptamers on the Si NW surfaces was compared. For our Si NW ISFET configuration both methods showed similar results. Further, the responses of the sensors to two different batches of PSA showed contrasting threshold shifts, thereby

implying variation in PI of the commercially obtained PSA. In both experimental series a clear dose-dependent electronic detection was confirmed. The two contrasting shifts show, however, that a precise control of the biomolecule source and eventually the glycosylation condition of PSA plays a major role for real clinical applications.

Moreover, the aptamer-PSA immobilization on the Si NW surfaces was successfully confirmed by optical reference methods, where classical chemiluminescence and fluorescence sandwich immunoassays were used. The transistors were integrated with PDMS-based, microfluidic channels. Additionally, the selectivity for the PSA detection was also verified using non-specific receptors for PSA.

The work presented here, could be further extended with multiple receptor immobilization on a single chip and an improved microfluidic integration to carry out time-dependent measurements of different PCa biomarkers, simultaneously. Thus, in this way, more reliable information about PCa could be obtained to render the electronic detection more reliable for practical applications.

Chapter 6: Real-time detection of cytokine IL-4 using Si NW ISFETs*

To continue further towards POC device development, real-time detection of the T cell cytokine "Interleukin-4 (IL-4)" was carried out using our Si NW ISFET sensors. In this chapter, firstly a basic introduction to cytokines and conventional methods used for their detection is given. The involvement of IL-4 in various diseases and its importance as a clinical biomarker is also discussed.

In order to apply potentiometric detection of recombinant protein IL-4 (analyte), specific receptor antibodies such as alpha (α) IL-4 were passively adsorbed onto the Si NW surfaces. The obtained shifts in threshold voltage of the Si NW ISFET sensors on immobilization of the receptor molecules and on binding of the analytes are shown and discussed. Moreover, the specificity of the detection mechanism for binding between receptor and analyte on the Si NW surfaces is also discussed.

Additionally, time-dependent measurements for the detection of the recombinant protein IL-4 using the 4-channel, portable measurement setup of our Si NW ISFETs are described. The merits of the deployed sensor platform in terms of stability for long term, continuous measurements are also discussed.

Finally, the obtained dose-response curve from real-time measurements was used to evaluate the Si NW ISFET signals for different IL-4 concentrations. The thus calibrated sensor was then used for the estimation of concentrations of IL-4 present in a cell culture medium sample from a mouse T-cell culture. By this procedure the unknown concentration of IL-4 in the cell culture medium was detected using the obtained changes in threshold voltages as a proof-of-concept bioassay.

6.1. Cytokines: Basic introduction

On invasion of external pathogens, the immune system of a living organism protects itself by complex defense mechanisms. The exact pathways in these reaction cascades are not yet fully understood in subject of current biomedical research. These pathways involve continuous functional interactions among different types of biomolecules, cells and organs over time [3, 168, 180]. In the group of biomolecules, cytokines play an important role and are responsible for the management of the host defense, tissue homeostasis, cell-cell communication and inflammatory reaction [3, 168, 180-182]. Cytokines are low molecular weight proteins secreted by immune cells such as lymphocytes and epithelial cells [181]. They are important biomarkers for immunological

* The results of this chapter are submitted for publication (September 2017): D. Rani, V. Pachauri, Y. Singh, X. T. Vu, S. Ingebrandt et. al.; Label-free detection of cytokine IL-4 using Si NW ISFETs biosensors.

studies and *in vitro* diagnostics [180]. When an infection or a tissue dysfunction or another change in the extracellular environment occurs, the cells of the immune system react by changing their functions. For instance, the systemic inflammatory response syndrome results from a pro-inflammatory phase of the immune system, in which there is an excessive production of pro-inflammatory cytokines such as interleukin-2 (IL-2), interleukin-6, interferon-gamma and the TNF-α. This phase is counteracted by an anti-inflammatory phase in which there is excessive production of anti-inflammatory cytokines, including interleukin-10, the transforming growth factor and the interleukin-4 (IL-4). Thus, these two phases counteract each other and maintain the immunological equilibrium [3, 181, 183].

Conventional imaging methods for cytokines only provide a qualitative information, in which the desired cells (isolated immune cells) are labelled to detect their physiological status. Since the response of the immune system is very dynamic, quantification of cytokine levels alone in blood, lymph nodes or tissue samples do not give enough information during the course of disease progression. Therefore, in order to monitor the cellular behaviour precisely, it is important to quantify multiple cytokines secreted by isolated immune cells or in a whole blood sample (cytokines are present in the serum as well as in the plasma, simultaneously). The thus obtained information can be used further to adjust therapies in different inflammatory disease conditions such as sepsis, cancer, lupus and graft-versus-host disease [3, 168, 182].

Conventional diagnostic methods used in laboratories such as enzyme linked immunosorbent spots, enzyme linked immunosorbent assays and real-time PCR are able to quantify the extracellular cytokine production with multiplexing ability and high sensitivity (1 pg/ml) [181]. However, these methods are not suitable for rapid and frequent measurements of complex biological fluids (blood, saliva, cell culture medium samples) to monitor the immune status, as they are all arduous, costly, multi-step methods and require long completion times (≈ 3 days) [3, 167, 181]. Therefore, in recent years, biosensor assays based on various label-free detection methods were developed. These methods have shown a high capability to simplify and accelerate the detection process of cytokines for instance in cell culture medium [3].

Over the last two decades, due to the improvement in nanofabrication technology and methods for nanomaterial synthesis, various new, label-free biosensors were developed. These include mechanical, electrochemical, optical and plasmonic biosensors [3, 166-169]. Within the group of label-free biosensors, Si NW ISFET biosensors are most common (as discussed in section 2.4 of chapter 2) due to the well-known and controllable properties of Si and the availability of low-cost, mass production facilities [6, 31-32, 58]. On miniaturization, these sensors can be easily integrated with microfluidic structures. Therefore, they have the potential for parallel detection of multiple cytokine types, which is also strongly demanded to monitor the immune balance. In several recent reports transistor-based biosensors were successfully deployed for cytokine detection. These include the detection of TNF-α, interleukin-1 beta, IL-6, IL-8 using

FETs based on MoS_2, CNT and Si NWs [43, 80-81, 184-187]. Besides these, optical ring resonator and plasmonic biosensors were also reported for real-time detection of IL-4. However, most of these methods need expensive instrumentation and thus are not suitable for on-chip integration [3, 167]. Nonetheless, recently Chen and co-workers reported multiplexed, real-time detection of six cytokines IL-2, IL-4, IL-6, IL-10, TNF-α and IFN-γ in a complex serum matrix using a label-free, multi-arrayed, LSPR, optical biosensor device [168].

IL-4 is a cytokine that has multiple functions. It regulates proliferation, differentiation and apoptosis in cells of haematopoietic and non-haematopoietic origin. It plays an important role in naïve CD_4^+ T cells or T helper (Th)0 cell differentiation by promoting Th2 cell differentiation and inhibiting Th1 cell differentiation [188]. The influence of IL-4 and its signalling machinery is diverse on different diseases. For instance, IL-4 mediated Th2 cell differentiation acts against parasitic infections and rheumatoid arthritis, but on the other hand it also promotes diseases like allergic asthma [181, 188-189]. Therefore, it is crucial to quantify IL-4 levels secreted by cells because of its involvement in promotion or inhibition of various diseases.

In the following sections, details of the electronic detection of cytokine IL-4 using Si NW ISFET sensors *via* passive adsorption of IL-4 specific receptor antibodies on the Si NW surfaces are given. Two sets of experiments were carried out for detection of IL-4. Initially, real-time detection of recombinant protein IL-4 was carried out using Si NW ISFETs and a calibration curve was generated. Thereafter, this calibration curve was used to evaluate the unknown concentration of IL-4 in a cell culture medium sample of mouse T-cells.

6.2. Recombinant protein IL-4 detection

The fabrication and operation mechanism of the Si NW ISFET sensors used for IL-4 detection were described in chapter 3 and 4, respectively [32]. The Si NW ISFETs were utilized for the detection of recombinant protein IL-4. The various steps in the immobilization protocol for the cytokine IL-4 assay were described in section 3.3.3 of chapter 3 and are also illustrated in figure 6.1. The Si NWs were firstly cleaned with piranha solution. Thereafter, passive adsorption of cytokine receptor antibodies (alpha (α) IL-4) on the Si NW surfaces was allowed. Subsequently, the binding of the analyte cytokine (IL-4) antibodies to the α IL-4 functionalized Si NWs was detected. As illustrated in figure 6.1 A, the specific binding of analytes IL-4 onto the α IL-4 functionalized Si NW surface resulted in a complex formation between IL-4 and α IL-4. This complex formation on the Si NW surface resulted in a change in charge density on the Si NW surface and this can be detected as a change in V_{th} of the Si NW ISFETs. In order to check if the observed changes in V_{th} were specific to the IL-4 binding, separate control experiments were carried out as illustrated in figure 6.1 B and C. Binding of non-conjugate antibodies such as IL-2 to the α IL-4 functionalized Si NW surfaces is illustrated in figure 6.1 B. Additionally, the direct binding of the IL-4 to the

Si NW surfaces in the absence of the specific receptor α IL-4 was tested as it is shown in figure 6.1 C. After each of the immobilization steps, transfer characteristic measurements of the Si NW ISFETs were carried out in 10 mM PB at pH 7.4.

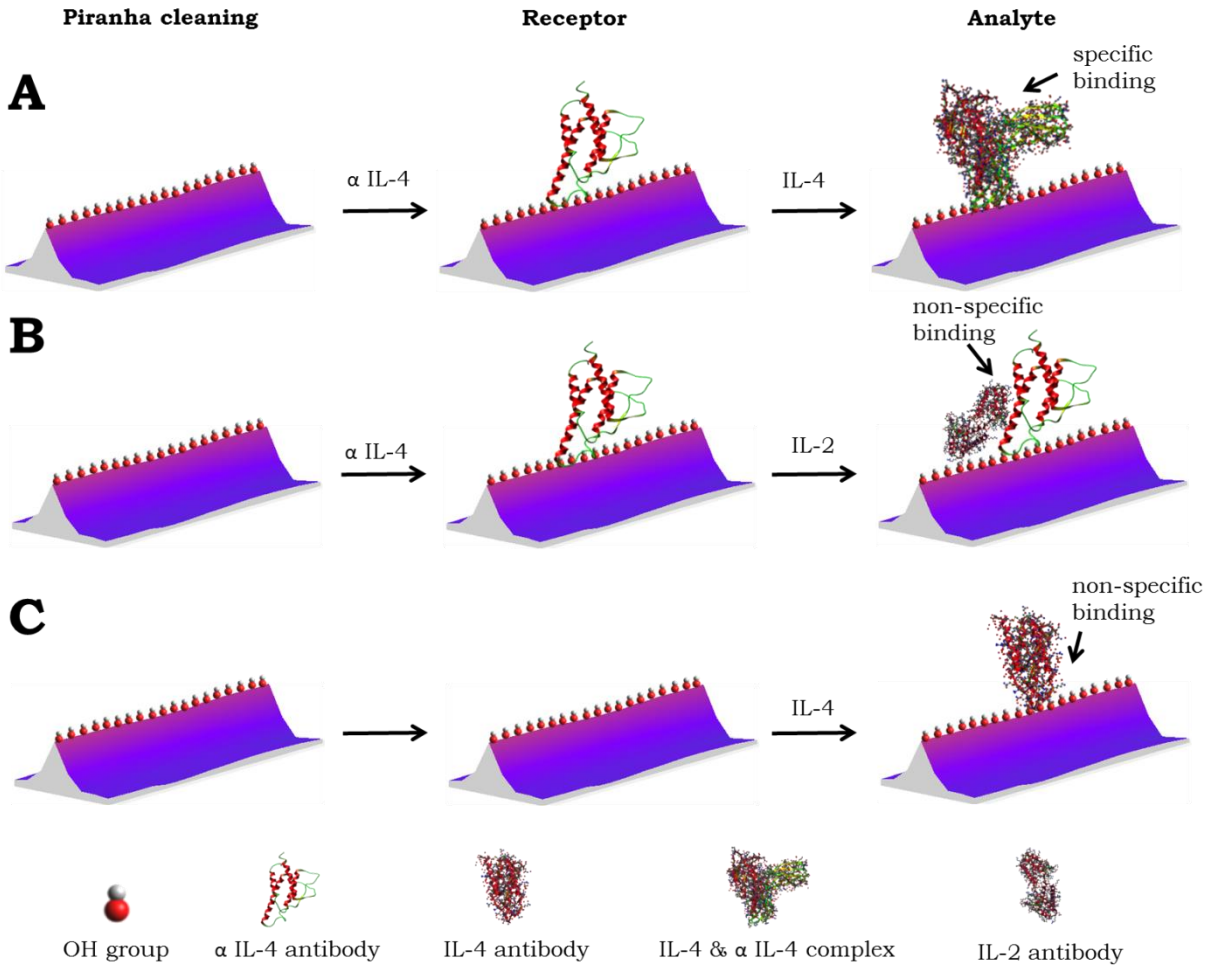

Figure 6.1 Schematics for the surface functionalization of the Si NW surface after piranha cleaning: (A) Cytokine IL-4 assay, where IL-4 antibody was allowed to react with the α IL-4 receptor functionalized Si NW surface and thereby a complex between IL-4 and α IL-4 over the Si NW surface was formed; (B) Control experiment where non-conjugate antibody, IL-2 was allowed to react with the α IL-4 receptor functionalized Si NW surface, that resulted in non-specific binding of IL-2 over the Si NW surface; and (C) Another control experiment, where IL-4 was allowed to react with the Si NW surface without α IL-4 receptor and thus IL-4 was bound non-specifically over the Si NW surface.

In figure 6.2 A, the transfer characteristic curves of a Si NW ISFET at the different immobilization steps during the cytokine IL-4 assay are shown. From the transfer characteristic curves shown in figure 6.2 A it can be deduced that the V_{th} of the p-type Si NW ISFET decreased with α IL-4 (1 µg/ml) antibody immobilization. Alpha (α) IL-4 is the alpha chain of the interleukin-4 receptor and can regulate the immunoglobulin E production among B cells by binding to IL-4 and IL-13. It is a 25 kDa transmembrane protein with a PI of 6 [190].

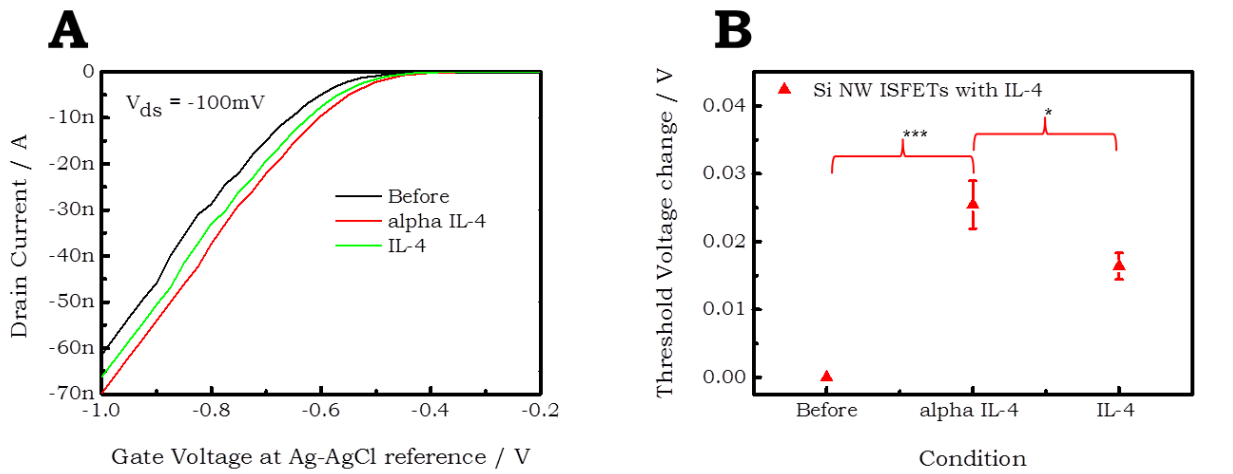

Figure 6.2 (A) Si NW ISFET transfer characteristic curves at the different assay steps for the cytokine IL-4 assay, that included piranha cleaning (before), α IL-4 (1 µg/ml) immobilization and IL-4 (250 µg/ml) binding; and (B) Change in the V_{th} of Si NW ISFETs (n = 4) with respect to before at different immobilization steps for the cytokine IL-4 assay shown in the scatter plot (*** for P < 0.001 and * for P < 0.1).

Therefore, the decrease in V_{th} (as shown in figure 6.2 A) upon binding of the α IL-4 antibodies in the measurement buffer (10 mM PB) of pH (7.4) was due to an addition of negative charges to the Si NW surfaces. Nonetheless, the exact configuration of the antibodies on the Si NW surfaces and their position within or outside the Debye length, is difficult to assess [32].

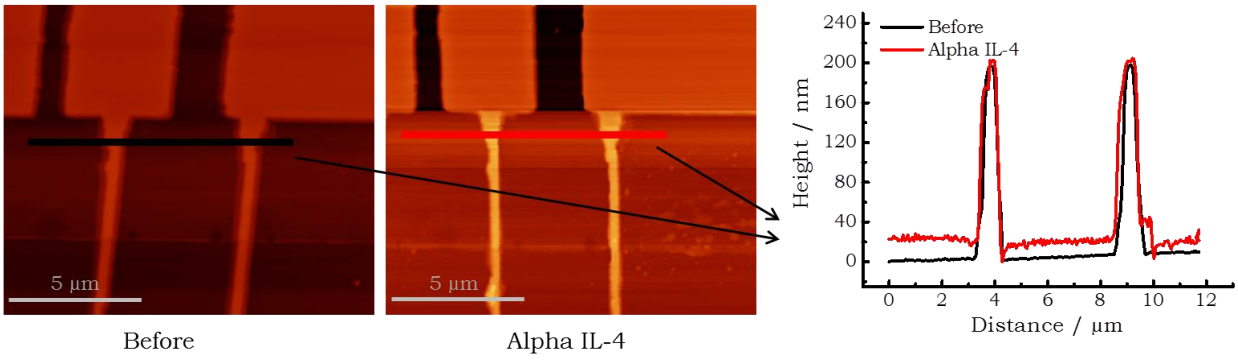

Figure 6.3 AFM image of an area of a Si NW set before and after the α IL-4 immobilization with the corresponding line plot for height analysis shown on the right side.

The binding of antibodies onto the Si NW surface was therefore also confirmed by AFM characterization of the Si NWs before and after the antibody immobilization as it is shown in figure 6.3. From the line plot for height analysis shown in figure 6.3 (right side) it can be observed that after the receptor α IL-4 antibody immobilization the height of the Si NWs increased. In addition also an increased roughness can be seen which indicated the antibody binding as well. This confirmed the presence of

antibodies on the Si NW surfaces and thus it can be expected that the observed changes in V_{th} of sensors during the bioassay were caused by the bound antibodies.

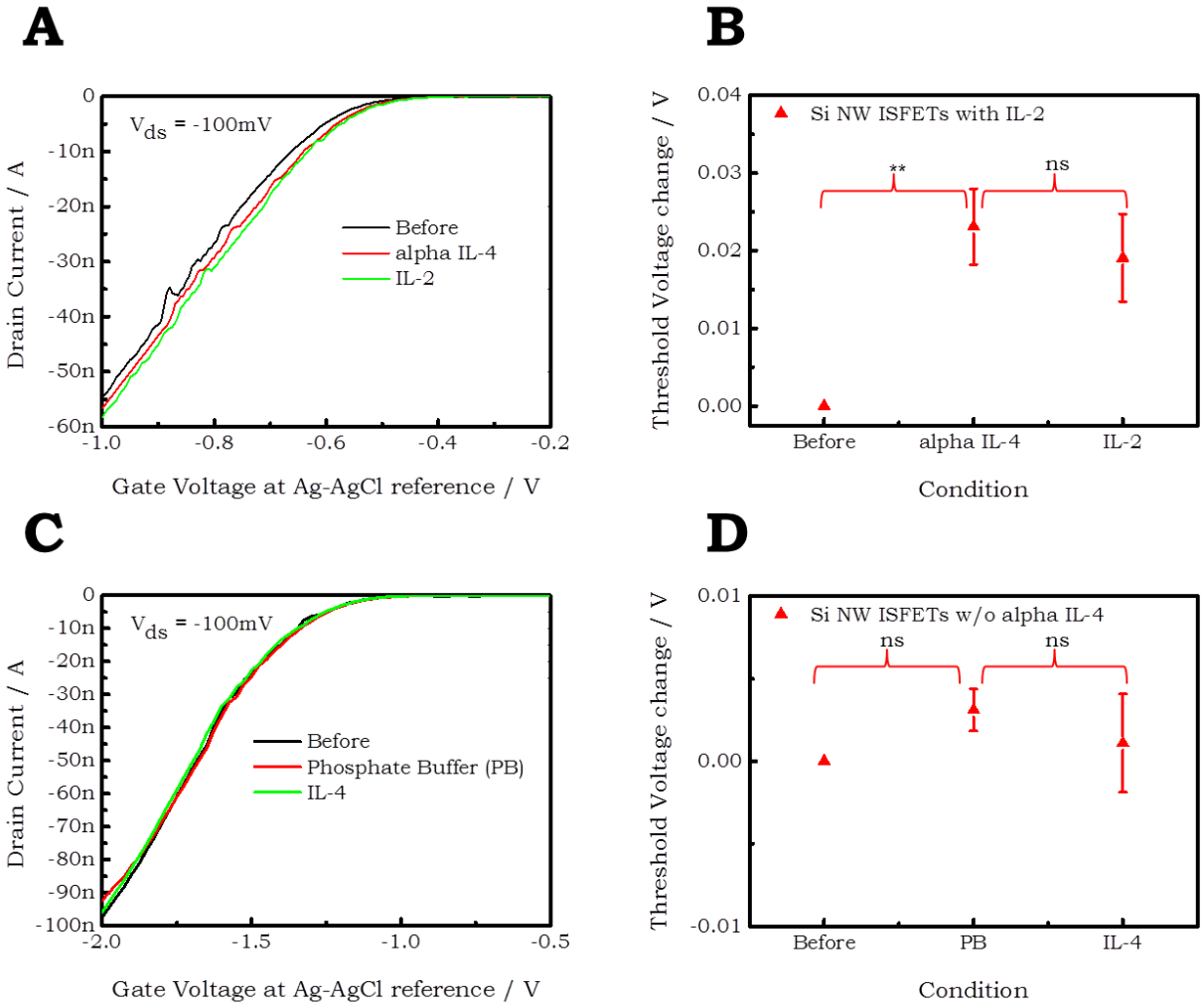

Figure 6.4 Si NW ISFET transfer characteristic curves at different assay steps for (A) Control of cytokine IL-4 assay without IL-4 that included piranha cleaning (before), α IL-4 (1 µg/ml) immobilization and reaction with IL-2 (100 µg/ml); (C) Control of the cytokine IL-4 assay without α IL-4 that includes piranha cleaning (before), PB (without α IL-4) and IL-4 (250 µg/ml) immobilization. Change in the V_{th} of the Si NW ISFETs at different assay steps shown in the scatter plot for (B) Control of cytokine IL-4 assay without IL-4 (n = 4); and (D) Control of the cytokine IL-4 assay without α IL-4 (n = 2) (ns for not significant and ** for $P < 0.01$).

After the passive adsorption of the α IL-4 receptor antibodies on the Si NWs, the respective conjugate antibodies (recombinant IL-4 protein) were allowed to react with the surface. The receptor-analyte binding at the Si NW surfaces resulted in an increase in V_{th} of the Si NW ISFETs as it can be seen in figure 6.2 A. This increase in V_{th} could be related to the isoelectric point (i.e., 8.18) of the conjugate IL-4 (i.e., 16 kDa protein) [191]. Thus, the antibody binding in the measurement buffer resulted in an addition of positive charges to the Si NW surfaces. The change in V_{th} of the Si NW

ISFETs upon binding of IL-4 is shown in the scatter plot in figure 6.2 B and a statistical analysis was done using a paired t-test. It can be seen that the V_{th} decreased when the α IL-4 antibodies were immobilized and it increased again with IL-4 detection as expected from theory. In both cases the V_{th} changes are in accordance with the respective isoelectric points of the biomolecules and are statistically significant (*** for P < 0.001 and * for P < 0.1).

For the cytokine assays two control experiments were done. In the first control experiment, recombinant interleukin-2 (IL-2) antibody was used instead of IL-4 as an analyte in order to check the non-specific binding of IL-2 to the α IL-4 functionalized Si NW surfaces (illustrated in figure 6.1 B). From the transfer characteristic curves shown in figure 6.4 A, it can be seen that the V_{th} shifts of the Si NW ISFETs decreased slightly with α IL-4 and IL-2 binding. The V_{th} decrease with the α IL-4 binding was in accordance with its PI (** for P < 0.01), but the V_{th} decrease with IL-2 binding was not statistically significant. The decrease in the V_{th} of the Si NW ISFETs on reaction with IL-2 can be attributed to a non-specific binding of the IL-2 proteins, which results in addition of negative charges (isoelectric point = 4.88) to the Si NW surfaces [192]. From the corresponding scatter plot of the V_{th} changes of all Si NW ISFETs used in these experiments (figure 6.4 B), it can be seen that the shifts in V_{th} upon IL-2 binding were not significant (ns for not significant).

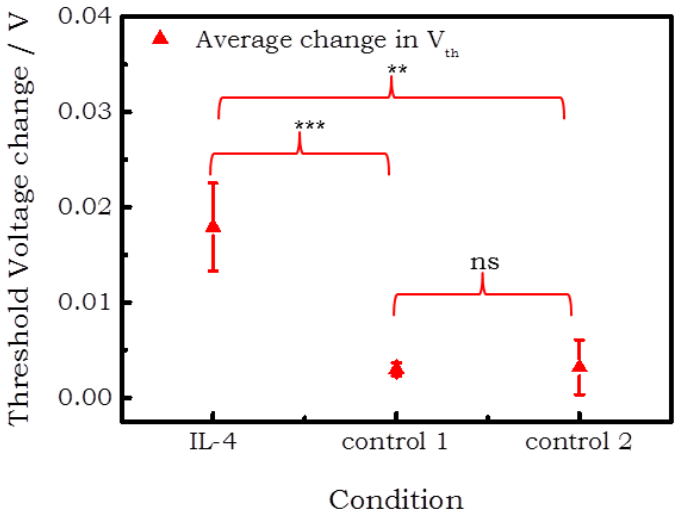

Figure 6.5 Scatter plot showing the average change in V_{th} of Si NW ISFETs (n = 4) on IL-4 binding with respect to the α IL-4 immobilization for the cytokine IL-4 immunoassay and the two control experiments - control 1 and control 2 (ns for not significant, *** for P < 0.001 and ** for P < 0.01).

In the second control experiment, the non-specific binding of IL-4 to the Si NW surfaces in the absence of the α IL-4 receptors was tested. In figure 6.4 C, the transfer characteristic curves of an exemplary Si NW ISFET at different assay steps are shown. The assay steps included piranha cleaning (labelled as before), PB (without α IL-4) and

IL-4 immobilization (figure 6.1 C). From the figure 6.4 C, it can be seen that the shifts upon binding of IL-4 without the α IL-4 receptors were not significant as well. From the corresponding scatter plot shown in figure 6.4 D, the deduced changes in threshold voltage on PB washing and on IL-4 binding were both not significant (ns for not significant). Therefore it can be concluded that the V_{th} changes on binding of IL-4 to the α IL-4 functionalized Si NW surfaces (figure 6.2) were specific to a complex formation between IL-4 and α IL-4. The average change in V_{th} of the Si NW ISFETs on IL-4 binding with respect to the α IL-4 immobilization for the cytokine IL-4 assay and the two control experiments (described above) is illustrated in the scatter plot in figure 6.5. It can be deduced from the figure, that the change in V_{th} for the two control experiments was negligible in comparison to the V_{th} change in the specific cytokine IL-4 assay (ns for not significant, *** for $P < 0.001$ and ** for $P < 0.01$). Thus, the binding of IL-4 was highly specific to the α IL-4 functionalized Si NW surfaces and the sensor concept can be used for further tests.

6.3. Time-dependent detection of IL-4

After the confirmation of the specific response of the Si NW ISFET sensors to the cytokine IL-4 binding using the transfer characteristic measurements, quantitative, time-dependent measurements were carried out using the portable, 4 channel measurement system (details were discussed in section 4.4 of chapter 4). For this, the transistors were operated at a fixed gate-source voltage (V_{gs} = -1.5 V) and drain-source voltage (V_{ds} = -1 V). The corresponding drain-source current was then measured as a function of time with a step wise increase in concentrations of the recombinant protein IL-4.

In figure 6.6 A, the drain-source current as a function of time at different concentration steps is shown. It can be seen that the drain-source current increases with binding of the receptor α IL-4 antibodies, while it decreases with increasing IL-4 concentrations. The observed changes in drain-source current can be correlated with the PI of the receptor α IL-4 antibodies and that of the IL-4 proteins. The observed drain current at each IL-4 concentration was then converted into gate voltage using the following formula (equation 2.25 from chapter 2):

$$V_{gs} = I_{ds}/g_m$$

-where g_m represents the transconductance. For the Si NW ISFET shown in figure 6.6, it is in the range of 1 μS and was calculated from the first derivative of transfer characteristic curves at V_{gs} = -1.5 V, V_{ds} = -1 V.

From the concentration-dependent measurements of IL-4 shown in figure 6.6 B, it can be deduced that the gate voltage decreases with the increase in IL-4 concentration. To extract a dose response curve for this sensor, concentrations of IL-4 between 192 fM (2.5 pg/ml) and 192 nM (2.5 μg/ml) were used.

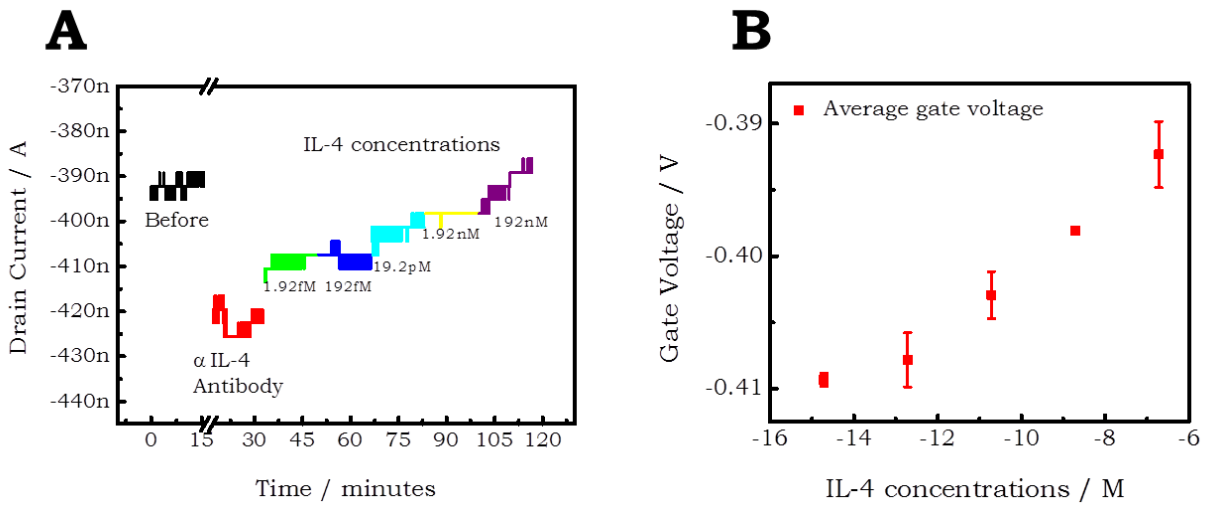

Figure 6.6 Real-time measurements for IL-4 detection using a Si NW ISFET sensor: (A) Drain-source current measured as a function of time at different steps that include α IL-4 immobilization (overnight: shown as a break in the graph), different concentrations of IL-4 (1.92 fM to 192 nM) detection (original time is longer than what is shown); and (B) Gate voltage plotted as a function of IL-4 concentration, where a decrease in the voltage with the increase in IL-4 concentration can be seen.

Further, during real-time measurements, the stability of the Si NW ISFETs was also analysed. The drain-source current signals remained stable over durations of more than 60 minutes, when the IL-4 concentration was unchanged. This indicates that the changes in drain-source current on addition of a new concentration of IL-4 after the specific reaction time are a result of changes in the biomolecular charge density on the Si NW surfaces.

6.4. IL-4 detection in a cell culture medium sample

After the concentration-dependent measurements of the recombinant protein IL-4, the obtained dose-response curve was used to evaluate an unknown concentration of IL-4 present in the cell-culture medium of mouse T-cells.

For this, the Si NW ISFETs surface was functionalized with α IL-4 receptor antibodies and then the Si NW surface was allowed to react with the cell culture medium containing IL-4 protein. Cell culture medium labelled as Th 2, which contained an unknown concentration of IL-4 was diluted in 1:10 (Th 2:PB) ratio for the assays. The transfer characteristic measurements of Si NW ISFETs at different immobilization steps are shown in figure 6.7. From the transfer characteristics measurements shown in figure 6.7 A and C, it can be deduced that the V_{th} of Si NW ISFETs decreased on immobilization of α IL-4 receptor antibodies and this was in accordance with the theory. On reaction of the Si NW ISFET surface with the cell culture medium containing IL-4, it can be seen that the V_{th} of Si NW ISFETs increased (shown in figure 6.7 A). This is also in accordance with the PI of IL-4 as was described in the previous sections. The corresponding scatter plot is illustrated in figure 6.7 B.

The obtained changes in V_{th} were in accordance with the theory and statistically significant (*** for P < 0.001 and * for P < 0.1).

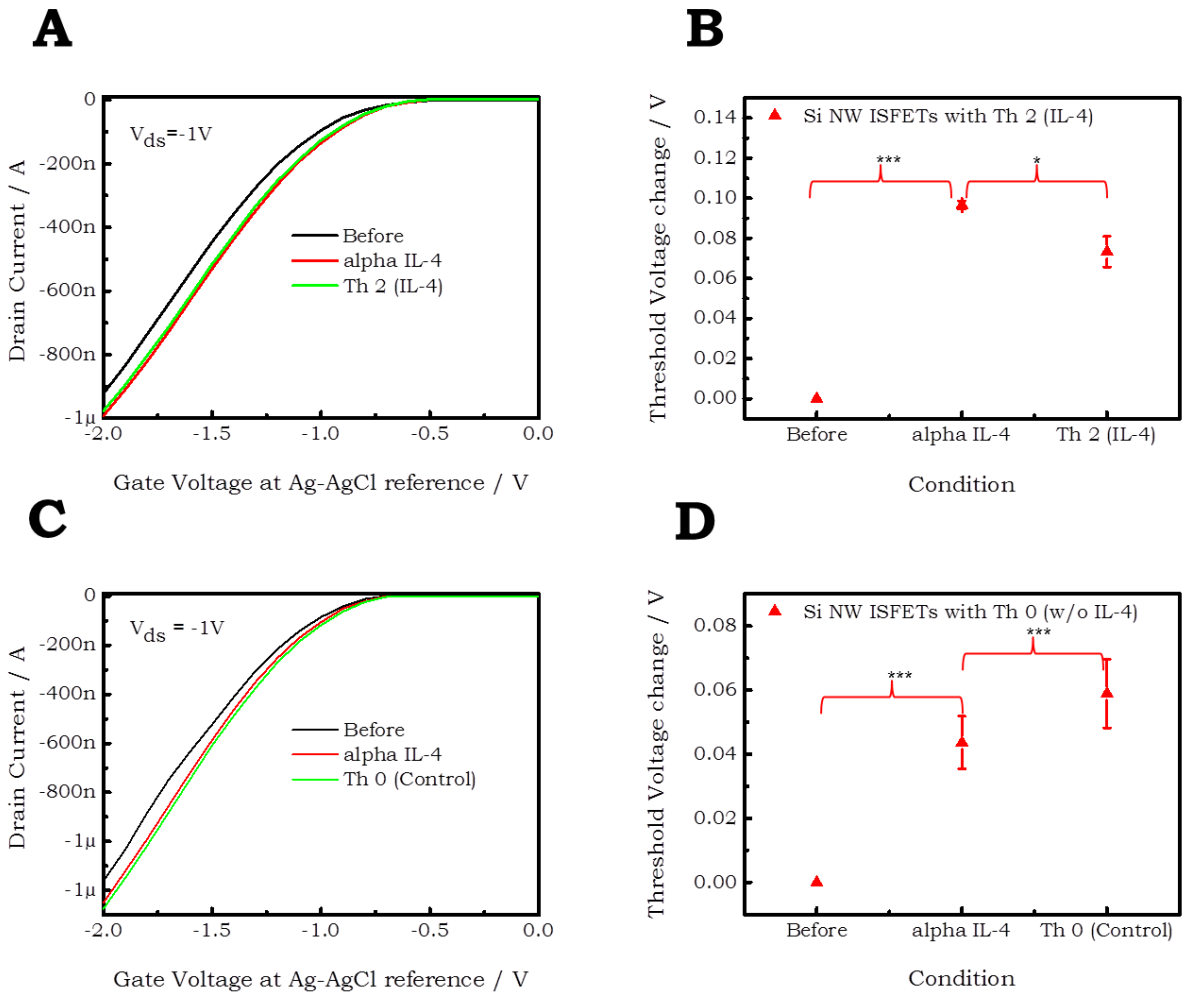

Figure 6.7 Si NW ISFET transfer characteristic curves at different immobilization steps for (A) Cytokine IL-4 assay that includes piranha cleaning (before), α IL-4 receptor (1 µg/ml) immobilization and Th 2 (IL-4) reaction; and (C) Control for the cytokine IL-4 assay that includes piranha cleaning (before), α IL-4 receptor (1 µg/ml) immobilization, Th 0 (without IL-4) reaction; The V_{th} changes (with respect to before) after the different immobilization steps are shown in the scatter plot for (B) Cytokine IL-4 assay (n = 3); and (D) Control for cytokine IL-4 assay (n = 8) (*** for P < 0.001 and * for P < 0.1).

A separate control experiment was also carried out in order to check the stability of the sensors in the absence of the conjugate antibodies (IL-4). For this, the cell culture medium without the conjugate antibody (i.e., Th 0 in 1:10 ratio) was allowed to react with the Si NW surfaces after the receptor antibody binding (1 µg/ml of α IL-4). As it can be seen in figure 6.7 C and D, the V_{th} decreased with Th 0 immobilization (*** for P < 0.001). This could be due to a non-specific binding of components present in the cell

culture medium and needs to be further improved by using specific blocking agents in future experiments.

Moreover, the unknown concentration of IL-4 antibodies in the cell culture medium was estimated using the dose-response curve obtained from the real-time measurements. The change in equivalent gate voltage on IL-4 reaction with respect to the α IL-4 immobilization (figure 6.8 B) on the Si NW surfaces was evaluated from the dose-response curve shown in figure 6.6 B.

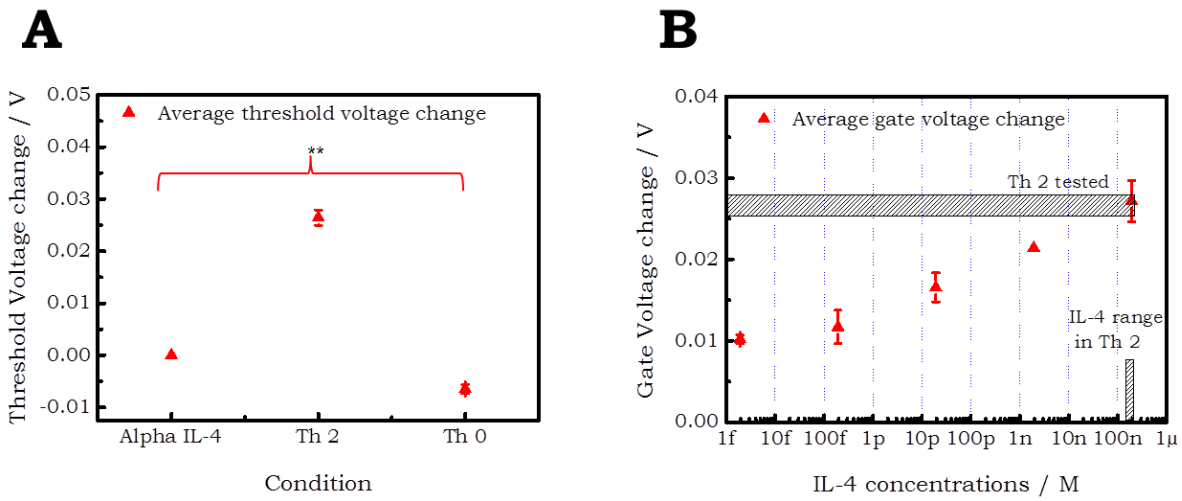

Figure 6.8 (A) Scatter plot showing the average change in V_{th} of Si NW ISFETs (n = 2) on Th 2 and Th 0 binding with respect to the α IL-4 immobilization (** for P < 0.01); and (B) Calibration curve obtained from the real-time measurements of recombinant protein IL-4, where the changes in the gate voltage (with respect to the α IL-4 immobilization) are shown as a function of increasing IL-4 concentrations.

Additionally, the change in V_{th} on Th 2 and Th 0 reaction with respect to the α IL-4 immobilization (figure 6.8 A) was calculated from the transfer characteristics shown in figure 6.7 A and C, respectively. From the scatter plot shown in figure 6.8 A, it can be deduced that the average change in V_{th} of the Si NW ISFETs with both Th 2 and Th 0 reaction on the α IL-4 immobilized Si NW surfaces was very statistically significant (** for P < 0.01). Further, the average change in V_{th} with Th 0 reaction was in opposite direction in comparison to Th 2 reaction (due to the non-specific binding of components of the cell culture medium), as was explained earlier in the previous paragraph. The obtained average change in V_{th} on Th 2 reaction (≈ 26 ± 1 mV) was then correlated with the calibration curve (figure 6.8 B) obtained from the dose-response curve. The IL-4 concentration corresponding to the change in V_{th} was in the range of 192 nM (2.5 µg/ml) as can be observed from the calibration curve shown in figure 6.8 B. Thus, the Si NW ISFETs were successfully deployed to estimate concentration of IL-4 in the cell culture medium of mouse T-cells.

6.5. Conclusion

In conclusion, a new method for the real-time detection of the recombinant protein IL-4 using Si NW ISFET sensors was developed. Already by passive adsorption of the α IL-4 receptor antibodies onto the Si NW ISFET sensors and by potentiometric detection of the IL-4 proteins, a specific response was obtained. The specificity of the V_{th} shift for the IL-4 receptor-analyte binding on the Si NW surfaces was confirmed using non-conjugate antibodies as a control. Further, time-dependent measurements using a portable measurement setup showed a sensitive detection of the recombinant IL-4 proteins in a wide concentration range from 192 fM to 192 nM. Additionally, the stability of the Si NW ISFET sensors for longer operation periods was verified by long term measurements for the detection of IL-4. In the end, the calibration curve obtained from the real-time measurements was used to evaluate an unknown IL-4 concentration present in the cell culture medium of mouse T cells. Unfortunately, the real concentration was not known since we were lacking for a standard reference method. Therefore this experimental procedure can be regarded as a proof-of-concept for possible future application of our sensitive and selective biosensor platform.

The work presented in this chapter could be improved further by a covalent immobilization of the antibodies to the Si NW surfaces in order to increase the density of specific binding sites. Additionally, specific blocking agents should be used to prevent the non-specific binding of biomolecules, while measuring the cytokine concentration in complex cell culture mediums. In future, the multichannel Si NW ISFET sensors could be functionalized with multiple cytokine receptor antibodies and integrated with a closed microfluidic system. With such a microfluidic Si NW sensor platform continuous, real-time detection of multiple cytokines could be realized for regular monitoring of the immune system status.

Chapter 7: Conclusion and Outlook

Conclusion

In this thesis work a new protocol for a high-throughput fabrication of Si NW ISFET sensors using a combination of top-down approaches based on NIL, UV lithography and wet etching methods was developed. The fabricated transistors were deployed for various chemical and biomolecule sensing applications, where the reliability and stability of the responses was demonstrated.

For the fabrication of the nano-scale transistors, firstly the specific layout of the Si NW ISFET chips was designed and realized using the Clewin software. A single chip consisted of individually addressable Si NW ISFETs arranged in eight sets of four NWs each, with a common source electrode and individual drain electrodes. Si NW ISFET sensor chips with different NW dimensions were arranged on a wafer. To carry out the fabrication of the Si NW ISFET sensors *via* NIL, a new mould with the designed chip configuration was obtained from the Institute of Microelectronics Stuttgart, Germany. The mould was fabricated on a SiO_2/Si wafer using EBL and RIE. The SiO_2/Si wafer was patterned to have trenches in the designed transistor area. The aspect ratio of the pattern structures in the mould was also kept low in order to realize well-optimized structures after the nanoimprint process.

The fabrication of the Si NW ISFET sensors was done with commercially available, *prime* quality SOI wafers. The NIL parameters were optimized for the specific chip configuration, which consisted of nano- and micro-structures to overcome the proximity effect and to achieve an uniform filling of the micro structures with a suitable NIL resist. The dry etching process of the residual layer and the SiO_2 *via* RIE was optimized to prevent an over-etching of the structures and a damage of the desired nano-pattern. The etching time and the etchant solution temperature for the wet anisotropic etching of Si using TMAH needed to be optimized as well. The source and drain contact lines were highly doped with boron ions at Ion Beam Services, France, to increase their conductivity. On the other hand, the Si NWs were left undoped to achieve a high sensitivity of the devices. A thin layer of dry oxide SiO_2, grown *via* a dry thermal oxidation process, was used as the gate dielectric for liquid gating measurements as well as for passivation of the contact lines. In the end of the process, metal was deposited over the doped Si contact pads in order to realize an ohmic contact and thus, enhance the performance of the devices.

The fabricated Si NW transistors were characterized by structural characterization methods such as SEM and AFM. It was observed that the surface of the TMAH-etched Si NWs was very smooth with an uniform topography of all the Si NWs. The structural uniformity of the transistors was confirmed over the whole wafer. On operation in liquid gate configuration using an external Ag/AgCl reference electrode, the Si NW

ISFET sensors showed a p-type, enhancement-mode transistor characteristics with nearly-identical characteristics for all the transistors on wafer-scale.

In order to deploy the Si NW ISFET sensors for chemical and biological sensing applications, basic proof-of-principle experiments such as pH measurements were carried out. A linear response to buffer pH changes was obtained. Additionally, the sensors were utilized for real-time pH measurements using a portable, hand-held measurement system. The reproducibility of the sensor characteristics and the stability of the sensor signal for long-term, continuous measurements was verified in these experiments.

The Si NW ISFET sensors were further deployed for the label-free detection of prostate cancer biomarkers such as PSA using a new receptor-analyte combination. For the PSA detection, PSA-specific DNA aptamers were site-specifically immobilized on the Si NW surfaces using a microspotter system. A potentiometric detection of PSA using the Si NW ISFET sensors was then carried out and the devices showed detection far below the clinically relevant range. An experimental comparison of conventional Si micro ISFET sensors and the Si NW ISFET sensors was done for PSA detection. Here the nanoscale devices showed higher sensitivities. Moreover in these PSA experiments, the aptamer-PSA binding on to the Si NW surfaces was also confirmed using optical detection methods as a reference. To perform stable optical assays, the Si NW ISFET sensors were integrated with microfluidic channels realized in PDMS. For optical detection, a chemiluminescence and a fluorescence method with specific, secondary antibodies were utilized to indirectly determine the presence of PSA on the sensor surfaces.

Besides that, detection of other biomolecules such as IL-4, which is a T cell cytokine, was also carried out. The sensors were utilized for quantitative, time-dependent measurements of the recombinant protein IL-4 using a portable measurement setup. The Si NW surfaces were functionalized with α IL-4 (receptor) antibodies *via* passive adsorption and IL-4 concentrations in wide range were successfully tested. Further, the stability of our Si NW ISFET sensors for long-term measurements was also confirmed in these measurements. Moreover, the potentiometric detection of IL-4 in cell culture medium of mouse T cells was also implemented and an unknown concentration of IL-4 was evaluated using the obtained calibration curve from the real-time measurements.

Outlook

In this thesis work our newly fabricated Si NW ISFET sensors showed very reproducible characteristics on wafer-scale. They were then successfully deployed for sensitive and selective detection of various chemicals and biomolecules. However, the stability and sensitivity of these devices for multiple usage applications and also for biomolecule sensing could still be improved further. Modifications could be done in

our fabrication protocol and also in the biomolecule sensing protocols to enhance the performance of the sensors towards real bio/chemical sensing applications.

The stability of the transistors could be further improved by using other gate oxide materials such as Al_2O_3 or HfO_2 and by using a thicker buried oxide layer in order to enable multiple usages of the devices. A thicker passivation layer on the contact lines, a layer stack of oxide, nitride and oxide stack could also be used to minimize the capacitive signal, reduce noise level and improve the stability of the devices.

Besides that, the serial resistance of the contact lines could be reduced by silicidation of the contact lines, for instance by using Co or Ti silicide. Additionally, the chip configuration could be modified to have a more uniform distribution of structures during the NIL process to improve the yield of good chips per wafer.

Moreover, the usage of fully-depleted SOI for the Si NW ISFET sensors, where the Si device layer should even be thinner than in the process of this thesis work, could improve the sensitivity of the devices and also eliminate the body effect. Transistor chips with smaller Si NW dimensions and suspended Si NWs for a full wrapped-around gate configuration could further enhance the sensitivity of the Si NW devices. Furthermore, the fabrication protocol could be modified in order to realize Si NW tunnel field-effect transistors to enhance the sensitivity of the devices beyond the typical subthreshold swing limitation of conventional Si NW transistors. Finally, for a miniaturized system integration of an on-chip reference electrode would be helpful for system integration towards POC applications.

In this thesis work, the nanoscale transistors were deployed for pH sensing and could in a similar approach as well be used for other ions to study chemical reactions at the Si NW surfaces. Further, the transistors could be operated in a back-gate configuration and then be utilized for sensing of gas molecules. For instance, they could even be applied to detect analytes in exhaled breath of humans for non-invasive detection of clinically relevant biomarkers.

The Si NW ISFET sensors in this thesis were used for PSA detection using DNA aptamers as highly specific receptors molecules. This approach could be extended by immobilization of different receptors on Si NW surfaces. In this way, simultaneous, multiple biomarker detection could be realized on these multichannel devices in order to achieve a more reliable information about the status of prostate cancer. Different kinds of receptors such as antibodies, DNA aptamers and peptide nucleic acids could be immobilized on the individual sets of our Si NWs. Thereafter a comparison of the binding affinity of analytes such as PSA could be implemented *via* real-time measurements by studying the attachment and detachment process of the analyte molecules.

Also the cytokine detection assay could be further improved by covalent immobilization of the antibodies on the Si NW surfaces. In this way, the stability and

reliability of the binding events would be enhanced. The interfering non-specific binding of other biomolecules could also be minimized by using blocking agents. Further, the detection of multiple cytokines in complex body fluids could be done by immobilizing different receptors on individual Si NW sets and by carrying out time-dependent measurements of different cytokines. With such POC devices the stability of the immune system could be assessed.

The work reported in this dissertation thesis was very elementary and of basic science character. The developed, reliable sensor platform for label-free detection of chemicals and biomolecules has the potential in near future, after intensive optimization, to be used as a POC device for many different chemical and biomedical applications.

Appendix

Table 1: Softwares used

Clewin version 3.1.11:	WieWeb software, Netherlands
EAGLE version 7.3.0:	Autodesk, USA
OriginPro 9.0:	OriginLab Corporation, Germany
ImageJ:	National Institutes of Health, USA

Table 2: Equipments used

NIL Eitre 6 version 3.2.6:	OBDUCAT, Sweden
MA6 UV lithography:	Karl Suss, Germany
SEN850 ellipsometer:	SENTECH GmbH, Germany
Dimension 3100 AFM:	Digital Instruments Veeco Metrology, USA
SEM Supra 40:	Carl Zeiss AG, Germany
Dektak XT:	Bruker, USA
RIE:	SENTECH instruments GmbH, Germany
LPCVD:	INOTHERM München, Germany
F20-UV thin film analyzer:	Filmetrics, USA
Keithley 4200 semiconductor parameter analyzer:	Tektronix GmbH, Germany
sciFLEXARRAYER S3 microspotter:	Scienion AG, Germany
Wedge-wedge wire bonding machine:	West Bond Inc., USA
Contact angle instrument OCA 15 Plus:	Data Physics, Germany
Fluorescence microscope:	Leica DMLM, Germany
DAD-2H/6TM automatic dicing saw:	Disco, Japan

Table 3: Chemicals used for fabrication

Acetone:	ChemSolute, Germany
Isopropanol:	Merck, Germany
H_2SO_4:	AppliChem GmbH, Germany
H_2O_2:	MicroChemicals GmbH, Germany
1% HF:	MicroChemicals GmbH, Germany

TMAH:	MicroChemicals GmbH, Germany
mr-I 9000M Series Imprint Polymer:	Micro resist technology GmbH, Germany
Image Reversal Resist Series AR-U 4000:	Allresist GmbH-Germany

Table 4: Materials used for sensing

For PSA assay

PSA-specific aptamer ([AmC6T]TTTTT AATTAAAGCTCGCCATCAAATAGCTTT):	Sigma Aldrich, Germany
Non-specific aptamer (5'-H3N-(CH2)6-AAAAA TTAATTTCGAGCGGTAGTTTATCGAAA-3'):	Sigma Aldrich, Germany
Ethanolamine:	Sigma Aldrich, Germany
APTES:	Sigma Aldrich, Germany
GPTES:	Sigma Aldrich, Germany
PSA:	Merck Chemicals Ltd (Beeston, UK)
Anti-PSA Ab [5A6]-HRP (Catalogue no. Ab2446 used as a detector Ab for chemiluminescence-based PSA assays):	Abcam, United Kingdom
Anti-PSA FITC (Catalogue no. Ab178776 used as a detector Ab for fluorescence-based PSA assays):	Abcam, United Kingdom
Metallic plug adapters for the microchannel and capillary tubing (BTPE-90):	Instech Solomon (PA, USA)
Luminol, Pierce (SuperSignal® West Femto Substrate Trial Kit 34094 and SuperSignal West Pico 35065):	Thermo Scientific, Portugal
1 ml syringes:	CODAN, Germany

For cytokine assay

Th 2 (IL-4) and Th 0 cell culture medium:	Eberhard Karls University, Tübingen
Mouse α IL-4 antibody:	eBioscience, Germany
Recombinant IL-4 protein (Catalog Number: 14-8041):	eBioscience, Germany
Recombinant IL-2 protein (Catalog Number: 14-8021):	eBioscience, Germany

Phosphate buffer solution components

Monohydrate phosphate ($H_2NaO_4P.H_2O$): Carl ROTH GmbH, Germany

Dinatrium hydrogen phosphate (Na_2HPO_4): Carl ROTH GmbH, Germany

Table 5: Si NW FETs fabrication process flow

Step	Process	Parameter	Comments
1	SOI wafer cleaning:	Standard RCA cleaning	Table 6
2	Dry thermal oxidation:	1000 °C for 1 hour	50 nm approx.
3	**NIL**		
	Spin-coating:	mr9030 700 nm thick resist, post bake at 100 °C for 2 minutes	
	Imprint parameters:	95 °C imprint T, 50 Bar pressure, 900 seconds time, demoulding at T = 40 °C	
4	**RIE**		
	Residual layer etching:	100 W, 20 sccm O_2 plasma, 2 Pa, 4 minutes approx.	
	SiO_2 etching:	200 W, 30 sccm ChF_3 plasma, 3 Pa, 100 seconds	
	Resist etching from structures:	100 W, 20 sccm O_2 plasma, 2 Pa, 3 minutes	
5	Piranha cleaning:	10 minutes;	
	1% HF dip:	90+30 seconds;	
	25% TMAH at 90 °C:	1 minute	
6	Hard mask removal:	1% HF dip, 9 minutes	
7	Piranha cleaning:	10 minutes	
8	1st UV lithography step (Ion implantation Bright field mask):	2 μm thick resist AZ5214, prebaked at 110 °C for 55 seconds, exposure 40 seconds, hard contact, alignment gap 40, developed (AZ326 MIF) for 75 seconds	2 μm thick resist used as the mask for ion implantation
9	Ion implantation:	10 keV, 10^15 B at/cm^2, tilt 7 degrees	2 μm thick resist used for protecting NW region with implantation energy 10 keV for projection range of ~40 nm. Implantation dose for degenerate semiconductor (with dopant conc. ~10^20 atoms/cm^3) is 10^15 atoms/cm^2
10	Cleaning:	Acetone+isopropanol; RCA cleaning	Until resist is removed
11	Annealing:	850 °C for 30 minutes under N_2 atmosphere	
12	Gate dielectric	820 °C for 45 minutes	6-8 nm SiO_2 growth on NW

	growth:		surface
13	UV lithography step 2 (bright field mask for removal of gate oxide from metallic contact lines & back gate contact pads):	2 μm thick resist AZ5214, prebaked at 110 °C for 50 seconds, exposure 9 seconds hard contact, post baked at 120 °C for 2 minutes, flood exposure 30 seconds, developed for 60 seconds	Open metallic contact lines & back gate contact pads
14	SiO_2 etching	1% HF, 2 minutes approx.	
15	Metal deposition (200 nm Al, 20 nm Ti, 150 nm Au) and lift off (resist):		A rapid thermal annealing step (vacuum, 350 °C, 10 minutes) was performed to form *ohmic* contacts

Table 6: RCA cleaning parameters

Step	Process	Parameters
1	SC-0	H_2O_2:H_2SO_4 = 1:3, 60 °C, 10 minutes
2	1% HF	1% (v/v) HF, room temperature, 60 seconds
3	SC-1	H_2O:H_2O_2:NH_4OH = 20:4:1, 60 °C, 10 minutes
4	1% HF	1% (v/v) HF, room temperature, 60 seconds
5	SC-2	H_2O:H_2O_2:HCl = 20:1:1, 60 °C, 10 minutes

References

1. Eicher D, Merten CA (2011) Microfluidic devices for diagnostic applications. Expert Review of Molecular Diagnostics 11:505-519

2. Lu N, Dai P, Gao A et al. (2014) Label-Free and Rapid Electrical Detection of hTSH with CMOS-Compatible Silicon Nanowire Transistor Arrays. ACS Applied Materials & Interfaces 6: 20378-20384

3. Chen P, Huang N-T, Chung M-T et al. (2015) Label-free cytokine micro- and nano-biosensing towards personalized medicine of systemic inflammatory disorders. Advanced Drug Delivery Reviews 95:90-103

4. Vu XT (2011) Silicon nanowire transistor arrays for biomolecular detection. In: Dissertation, RWTH Aachen University

5. Shehada N, Cancilla JC, Torrecilla JS et al. (2016) Silicon Nanowire Sensors Enable Diagnosis of Patients via Exhaled Breath. ACS Nano 10:7047-7057

6. Zhang A, Lieber CM (2016) Nano-Bioelectronics. Chemical Reviews 116:215-257

7. Lee K-N, Seo Y-T, Kim Y-K et al. (2016) Detecting ions in air using a nanofield-effect transistor (nanoFET). Microelectronic Engineering 158:75-79

8. Mahdiar G, Razali I, Bahareh N et al. (2015) A new approach to model sensitivity of graphene-based gas sensors. Semiconductor Science and Technology 30:045012

9. Kim A, Ah CS, Yu HY et al. (2007) Ultrasensitive, label-free, and real-time immunodetection using silicon field-effect transistors. Applied Physics Letters 91:103901

10. Noor MO, Krull UJ (2014) Silicon nanowires as field-effect transducers for biosensor development: A review. Analytica Chimica Acta 825:1-25

11. Stern AG (2010) Design of a silicon avalanche photodiode pixel with integrated laser diode using back-illuminated crystallographically etched silicon-on-sapphire with monolithically integrated microlens for dual-mode passive and active imaging arrays. SPIE Proceedings, Detectors and Imaging Devices: Infrared, Focal Plane, Single Photon 7780:778011

12. Ma L-H, Han W-H, Wang H et al. (2016) Electronic transport properties of silicon junctionless nanowire transistors fabricated by femtosecond laser direct writing. Chinese Physics B 25:068103

13. Zhao Y, Yao J, Xu L et al. (2016) Shape-Controlled Deterministic Assembly of Nanowires. Nano Letters 16:2644-2650

14. Jariwala D, Sangwan VK, Lauhon LJ et al. (2014) Emerging Device Applications for Semiconducting Two Dimensional Transition Metal Dichalcogenides. ACS Nano 8:1102-1120

15. Balasubramanian K, Kern K (2014) 25th Anniversary Article: Label-Free Electrical Biodetection Using Carbon Nanostructures. Advanced Materials 26:1154-1175

16. Liu B, Lu L, Hua E et al. (2012) Detection of the human prostate-specific antigen using an aptasensor with gold nanoparticles encapsulated by graphitized mesoporous carbon. Microchim Acta 178:163-170

17. Liu H, Neal AT, Ye PD et al. (2012) Channel length scaling of MoS_2 MOSFETs. ACS Nano 6:8563-8569

18. Wang X, Zhu Y, Olsen TR et al. (2016) An aptameric graphene nanosensor for analyte detection in serum. In: 2016 IEEE 29th International Conference on Micro Electro Mechanical Systems (MEMS). p 286-289

19. Zhang C, Liang L, Ding L et al. (2016) Label-free measurements on cell apoptosis using a terahertz metamaterial-based biosensor. Applied Physics Letters 108:241105

20. Bogue R (2016) Lab-on-a-chip and other miniaturised analytical instruments. Sensor Review 36:109-114

21. Bhat N (2012) Chip and Dare Saga. RESONANCE 1035-1047 (http://www.ias.ac.in/article/fulltext/reso/017/11/1035-1047)

22. Carter SB (1967) Haptotactic islands: a method of confining single cells to study individual cell reactions and clone formation. Experimental Cell Research 48:189-193

23. Wise KD, Weissman RH (1971) Thin films of glass and their application to biomedical sensors. Medical and biological engineering 9:339-350

24. Manz A, Graber N, Widmer HM (1990) Miniaturized total chemical analysis systems: A novel concept for chemical sensing. Sensors and Actuators B: Chemical 1:244-248

25. Fodor SP, Read JL, Pirrung MC et al. (1991) Light-directed, spatially addressable parallel chemical synthesis. Science 251:767-773

26. Kumar A, Whitesides GM (1993) Features of gold having micrometer to centimeter dimensions can be formed through a combination of stamping with an elastomeric stamp and an alkanethiol “ink” followed by chemical etching. Applied Physics Letters 63:2002-2004

27. Kopp MU, Mello AJ, Manz A (1998) Chemical Amplification: Continuous-Flow PCR on a Chip. Science 280:1046-1048

28. Namdari P, Daraee H, Eatemadi A (2016) Recent Advances in Silicon Nanowire Biosensors: Synthesis Methods, Properties, and Applications. Nanoscale Research Letters 11:406

29. Abdul Rashid JI, Abdullah J, Yusof NA et al. (2013) The Development of Silicon Nanowire as Sensing Material and Its Applications. Journal of Nanomaterials 2013:16

30. Zhou W, Dai X, Lieber CM (2017) Advances in nanowire bioelectronics. Reports on Progress in Physics 80: 016701

31. Salhi B, Hossain MK, Mukhaimer AW et al. (2016) Nanowires: a new pathway to nanotechnology-based applications. Journal of Electroceramics 37:34-49

32. Rani D, Pachauri V, Mueller A et al. (2016) On the Use of Scalable NanoISFET Arrays of Silicon with Highly Reproducible Sensor Performance for Biosensor Applications. ACS Omega 1:84-92

33. Stoop RL, Wipf M, Müller S et al. (2015) Competing surface reactions limiting the performance of ion-sensitive field-effect transistors. Sensors and Actuators B: Chemical 220:500-507

34. Schasfoort RBM, Streekstra GJ, Bergveld P et al. (1989) Influence of an immunological precipitate on D.C. and A.C. behaviour of an isfet. Sensors and Actuators 18:119-129

35. Sze SM, Lee MK (2012) Semiconductor devices : physics and technology. 3rd ed. Wiley, New York

36. Bergveld P (2003) Thirty years of ISFETOLOGY: What happened in the past 30 years and what may happen in the next 30 years. Sensors and Actuators B: Chemical 88:1-20

37. Skoog D.A., West D.M, Holler F.J, Crouch S.R (2013) Fundamentals of analytical chemistry, 9e. Mary Finch

38. Chen S (2013) Electronic Sensors Based on Nanostructured Field-Effect Devices. In: Dissertation, Uppsala University

39. Afrasiabi R (2016) Silicon Nanoribbon FET Sensors: Fabrication, Surface Modification and Microfluidic Integration. In: Dissertation, KTH Royal Institute of Technology

40. van Hal REG, Eijkel JCT, Bergveld P (1996) A general model to describe the electrostatic potential at electrolyte oxide interfaces. Advances in Colloid and Interface Science 69:31-62

41. Schasfoort RBM, Bergveld P, Kooyman RPH, Greve J (1990) Possibilities and limitations of direct detection of protein charges by means of an immunological field-effect transistor. Analytica Chimica Acta 238:323-329

42. De Vico L, Iversen L, Sorensen MH et al. (2011) Predicting and rationalizing the effect of surface charge distribution and orientation on nano-wire based FET bio-sensors. Nanoscale 3:3635-3640

43. Hakim MMA, Lombardini M, Sun K et al. (2012) Thin Film Polycrystalline Silicon Nanowire Biosensors. Nano Letters 12:1868-1872

44. Schöning MJ, Poghossian A (2002) Recent advances in biologically sensitive field-effect transistors (BioFETs). Analyst 127:1137-1151

45. Li B-R, Chen C-C, Kumar UR et al. (2014) Advances in nanowire transistors for biological analysis and cellular investigation. The Analyst 139:1589-1608

46. Taiuk R, Meyyappan M, Chang-Ki B (2014) Optimized operation of silicon nanowire field effect transistor sensors. Nanotechnology 25:505501

47. Lin S-P, Pan C-Y, Tseng K-C et al. (2009) A reversible surface functionalized nanowire transistor to study protein–protein interactions. Nano Today 4:235-243

48. Patolsky F, Timko BP, Yu G et al. (2006) Detection, Stimulation, and Inhibition of Neuronal Signals with High Density Nanowire Transistor Arrays. Science 313:1100-1104

49. Maedler C, Kim D, Spanjaard RA et al. (2016) Sensing of the Melanoma Biomarker TROY Using Silicon Nanowire Field-Effect Transistors. ACS Sensors 1:696-701

50. Antonisse MMG, Snellink-Ruël BHM, Lugtenberg RJW et al. (2000) Membrane Characterization of Anion Selective CHEMFETs by Impedance Spectroscopy. Analytical Chemistry 72:343-348

51. Ingebrandt S, Han Y, Nakamura F et al. (2007) Label-free detection of single nucleotide polymorphisms utilizing the differential transfer function of field-effect transistors. Biosensors and Bioelectronics 22:2834-2840

52. Susloparova A, Koppenhöfer D, Vu XT et al. (2013) Impedance spectroscopy with field-effect transistor arrays for the analysis of anti-cancer drug action on individual cells. Biosensors and Bioelectronics 40:50-56

53. Susloparova A, Koppenhofer D, Law JKY et al. (2015) Electrical cell-substrate impedance sensing with field-effect transistors is able to unravel cellular adhesion and detachment processes on a single cell level. Lab on a Chip 15:668-679

54. Kharitonov AB, Wasserman J, Katz E et al. (2001) The Use of Impedance Spectroscopy for the Characterization of Protein-Modified ISFET Devices: Application of the Method for the Analysis of Biorecognition Processes. The Journal of Physical Chemistry B 105:4205-4213

55. Labordec, Pittinof, Verhoeven HA et al. (2015) Real-time imaging of microparticles and living cells with CMOS nanocapacitor arrays. Nature Nanotechnology 10:791-795

56. Ingebrandt S (2015) Bioelectronics: Sensing beyond the limit. Nature Nanotechnology 10:734-735

57. Presnova G, Presnov D, Krupenin V et al. (2017) Biosensor based on a silicon nanowire field-effect transistor functionalized by gold nanoparticles for the highly sensitive determination of prostate specific antigen. Biosensors and Bioelectronics 88:283-289

58. Luye M, Ye C, Sawtelle SD et al. (2015) Silicon Nanowire Field-Effect Transistors - A Versatile Class of Potentiometric Nanobiosensors. IEEE Access 3:287-302

59. Kuan D-H, Wang IS, Lin J-R et al. (2016) A microfluidic device integrating dual CMOS polysilicon nanowire sensors for on-chip whole blood processing and simultaneous detection of multiple analytes. Lab on a Chip 16:3105-3113

60. Gao A, Lu N, Wang Y et al. (2016) Robust ultrasensitive tunneling-FET biosensor for point-of-care diagnostics. Scientific Reports 6:22554

61. Cui Y, Wei Q, Park H et al. (2001) Nanowire nanosensors for highly sensitive and selective detection of biological and chemical species. Science 293:1289-1292

62. Cheng-Chih H, Chia Yu Y, Chiu-Jung L et al. (2014) Optimization of reusable polysilicon nanowire sensor for salt concentration measurement. Japanese Journal of Applied Physics 53:06JE04

63. Krivitsky V, Zverzhinetsky M, Patolsky F (2016) Antigen-Dissociation from Antibody Modified Nanotransistor Sensor Arrays as a Direct Biomarker Detection Method in Unprocessed Biosamples. Nano Letters 16:6272-6281

64. Trivedi K, Yuk H, Floresca HC et al. (2011) Quantum Confinement Induced Performance Enhancement in Sub-5-nm Lithographic Si Nanowire Transistors. Nano Letters 11:1412-1417

65. Zeimpekis I, Sun K, Hu C et al. (2015) Study of parasitic resistance effects in nanowire and nanoribbon biosensors. Nanoscale Research Letters 10:79

66. Nair PR, Alam MA (2007) Design considerations of silicon nanowire biosensors. IEEE Transactions on Electron Devices 54:3400-3408

67. Pui T-S, Agarwal A, Ye F et al. (2009) Ultra-sensitive detection of adipocytokines with CMOS-compatible silicon nanowire arrays. Nanoscale 1:159-163

68. Qing Q, Jiang Z, Xu L et al. (2014) Free-standing kinked nanowire transistor probes for targeted intracellular recording in three dimensions. Nature Nanotechnology 9:142-147

69. Cohen-Karni T, Timko BP, Weiss, LE et al. (2009) Flexible electrical recording from cells using nanowire transistor arrays. Proceedings of the National cademy of Sciences 106:7309-7313

70. Cohen-Karni T, Casanova D, Cahoon JF et al. (2012) Synthetically encoded ultrashort-channel nanowire transistors for fast, pointlike cellular signal detection. Nano Letters 12:2639-2644

71. Duan X, Gao R, Xie P et al. (2011) Intracellular recordings of action potentials by an extracellular nanoscale field-effect transistor. Nature Nanotechnology 7:174-179

72. Fu T-M, Duan X, Jiang Z et al. (2014) Sub-10-nm intracellular bioelectronic probes from nanowire–nanotube heterostructures. Proceedings of the National Academy of Sciences 111:1259-1264

73. Lin S-P, Vinzons LU, Kang Y-S et al. (2015) Non-Faradaic Electrical Impedimetric Investigation of the Interfacial Effects of Neuronal Cell Growth and Differentiation on Silicon Nanowire Transistors. ACS Applied Materials & Interfaces 7:9866-9878

74. Kim A, Ah CS, Park CW et al. (2010) Direct label-free electrical immunodetection in human serum using a flow-through-apparatus approach with integrated field-effect transistors. Biosensors and Bioelectronics 25:1767-1773

75. Poghossian A, Schöning MJ (2014) Label-Free Sensing of Biomolecules with Field-Effect Devices for Clinical Applications. Electroanalysis 26:1197-1213

76. Huang Y-W, Wu C-S, Chuang C-K et al. (2013) Real-Time and Label-Free Detection of the Prostate-Specific Antigen in Human Serum by a Polycrystalline Silicon Nanowire Field-Effect Transistor Biosensor. Analytical Chemistry 85:7912-7918

77. Shobha BN, Muniraj NJR (2014) Design, Modeling and Simulation of Prostate Cancer Biosensor with ssDNA biomarker and DGFET Biosensor. International Journal of Computer Science and Information Technologies 5:2612-2620

78. Mohd Azmi MA, Tehrani Z, Lewis RP et al. (2014) Highly sensitive covalently functionalised integrated silicon nanowire biosensor devices for detection of cancer risk biomarker. Biosensors and Bioelectronics 52:216-224

79. Tran DP, Wolfrum B, Stockmann R et al. (2015) Complementary Metal Oxide Semiconductor Compatible Silicon Nanowires-on-a-Chip: Fabrication and Preclinical Validation for the Detection of a Cancer Prognostic Protein Marker in Serum. Analytical Chemistry 87:1662-1668

80. Pui T-S, Agarwal A, Ye F et al. (2011) Nanoelectronic detection of triggered secretion of pro-inflammatory cytokines using CMOS compatible silicon nanowires. Biosensors and Bioelectronics 26:2746-2750

81. Zhang Y, Chen R, Xu L et al. (2015) Silicon Nanowire Biosensor for Highly Sensitive and Multiplexed Detection of Oral Squamous Cell Carcinoma Biomarkers in Saliva. Analytical Sciences 31:73-78

82. Li Z, Chen Y, Li X et al. (2004) Sequence-Specific Label-Free DNA Sensors Based on Silicon Nanowires. Nano Letters 4:245-247

83. Xie P, Xiong Q, Fang Y et al. (2011) Local electrical potential detection of DNA by nanowire–nanopore sensors. Nature Nanotechnology 7:119-125

84. Timko BP, Cohen-Karni T, Yu G et al. (2009) Electrical Recording from Hearts with Flexible Nanowire Device Arrays. Nano Letters 9:914-918

85. Patolsky F, Zheng G, Hayden O et al. (2004) Electrical detection of single viruses. Proceedings of the National Academy of Sciences of the United States of America 101:14017-14022

86. Lee K-N, Seo Y-T, Yoon S et al. (2016) Chemical gating experiment of a nano-field-effect transistor sensor using the detection of negative ions in air. Sensors and Actuators B: Chemical 236:654-658

87. Hwang S-W, Lee CH, Cheng H et al. (2015) Biodegradable Elastomers and Silicon Nanomembranes/Nanoribbons for Stretchable, Transient Electronics, and Biosensors. Nano Letters 15:2801-2808

88. Carmignani C, Rozeau O, Scheiblin P et al. (2016) Fine charge sensing using a silicon nanowire for biodetection. In: Abstract of the 2016 International Symposium on VLSI Technology, Systems and Application (VLSI-TSA). p 1-2

89. Li B-R, Hsieh Y-J, Chen Y-X et al. (2013) An Ultrasensitive Nanowire-Transistor Biosensor for Detecting Dopamine Release from Living PC12 Cells under Hypoxic Stimulation. Journal of the American Chemical Society 135:16034-16037

90. Shen S-H, Cheng H, Kao T-Y et al. (2014) Silicon-based Multi-nanowire Biosensor with High-k Dielectric and Stacked Oxide Sensing Membrane for Cardiac Troponin I Detection. Procedia Engineering 87:648-651

91. Xiaofeng G, Rui Z, Xiaomei Y (2015) High sensitive detections of Norovirus DNA and IgG by using multi-SiNWFET biosensors. In: Solid-State Sensors, Actuators and Microsystems (TRANSDUCERS), 2015 Transducers - 2015 18th International Conference on. p 1537-1540

92. Prostate Cancer Chapter 5 NANOWIRE SENSOR ARRAY FOR PROSTATE.119-150

93. Regonda S, Tian R, Gao J et al. (2013) Silicon multi-nanochannel FETs to improve device uniformity/stability and femtomolar detection of insulin in serum. Biosensors and Bioelectronics 45:245-251

94. Adam T, Hashim U (2015) Highly sensitive silicon nanowire biosensor with novel liquid gate control for detection of specific single-stranded DNA molecules. Biosensors and Bioelectronics 67:656-661

95. Kim S, Rim T, Kim K et al. (2011) Silicon nanowire ion sensitive field effect transistor with integrated Ag/AgCl electrode: pH sensing and noise characteristics. Analyst 136:5012-5016

96. Tong HD, Chen S, Van Der Wiel WG et al. (2009) Novel Top-Down Wafer-Scale Fabrication of Single Crystal Silicon Nanowires. Nano Letters 9:1015-1022

97. Zheng G, Patolsky F, Cui Y et al. (2005) Multiplexed electrical detection of cancer markers with nanowire sensor arrays. Nature Biotechnology 23:1294-1301

98. Li B-R, Chen C-W, Yang W-L et al. (2013) Biomolecular recognition with a sensitivity-enhanced nanowire transistor biosensor. Biosensors and Bioelectronics 45:252-259

99. Yang Y-H, Wu S-J, Chiu H-S et al. (2003) Catalytic Growth of Silicon Nanowires Assisted by Laser Ablation. The Journal of Physical Chemistry B 108:846-852

100. Wu Y, Cui Y, Huynh L et al. (2004) Controlled growth and structures of molecular-scale silicon nanowires. Nano Letters 4:433-436

101. Dehzangi A, Larki F, Naseri MG et al. (2015) Fabrication and simulation of single crystal p-type Si nanowire using SOI technology. Applied Surface Science 334:87-93

102. Nuzaihan MMN, Hashim U, Ruslinda AR et al. (2015) Fabrication of Silicon Nanowires Array Using E-beam Lithography Integrated with Microfluidic Channel for pH Sensing. Current Nanoscience 11:239-244

103. McAlpine MC, Friedman RS, Jin S et al. (2003) High-Performance Nanowire Electronics and Photonics on Glass and Plastic Substrates. Nano Letters 3:1531-1535

104. McAlpine MC, Friedman RS, Lieber CM (2003) Nanoimprint lithography for hybrid plastic electronics. Nano Letters 3:443-445

105. Zulfiqar A, Patou F, Pfreundt A et al. (2017) In-situ doped junctionless polysilicon nanowires field effect transistors for low-cost biosensors. Sensing and Bio-Sensing Research 13:88-95

106. Gao A, Lu N, Dai P et al. (2011) Silicon nanowire-based CMOS-compatible field-effect transistor nanosensors for ultrasensitive electrical detection of nucleic acids. Nano letters 11:3974-3978

107. Balla T, Spearing SM, Monk A (2008) An assessment of the process capabilities of nanoimprint lithography. Journal of Physics D: Applied Physics 41:174001

108. Cheng X, Li D, Guo LJ (2006) A hybrid mask–mould lithography scheme and its application in nanoscale organic thin film transistors. Nanotechnology 17:927-932

109. Chou SY, Krauss PR, Renstrom PJ (1995) Imprint of sub-25 nm vias and trenches in polymers. Applied Physics Letters 67:3114-3116

110. Cattoni A, Chen J, Decanini D et al. (2011) Soft UV Nanoimprint Lithography : a Versatile Tool for Nanostructuration at the 20nm Scale. In: Cui B. (ed) Recent Advances in Nanofabrication Techniques and Applications, p 1-17

111. Guo LJ (2004) Recent progress in nanoimprint technology and its applications. Journal of Physics D: Applied Physics 37:R123-R141

112. Vu XT, Eschermann JF, Stockmann R et al. (2009) Top-down processed silicon nanowire transistor arrays for biosensing. physica status solidi (a) 206:426-434

113. Misra D, Heasell EL (1990) Electrical damage to silicon devices due to reactive ion etching. Semiconductor Science and Technology 5:229-229

114. Chen S, Bomer JG, van der Wiel WG et al. (2009) Top-Down Fabrication of Sub-30 nm Monocrystalline Silicon Nanowires Using Conventional Microfabrication. ACS Nano 3:3485-3492

115. Si dangling bonds. http://www.iue.tuwien.ac.at/phd/entner/node14.html. Accessed October 2016

116. Stern E, Klemic JF, Routenberg DA et al. (2007) Label-free immunodetection with CMOS-compatible semiconducting nanowires. Nature 445:519-522

117. Thong JTL, Choi WK, Chong CW (1997) TMAH etching of silicon and the interaction of etching parameters. Sensors and Actuators A: Physical 63:243-249

118. Tran DP, Wolfrum B, Stockmann R et al. (2014) Fabrication of locally thinned down silicon nanowires. Journal of Materials Chemistry C 2:5229-5234

119. Saiful Islam M, Coyle ED, Kouzani AZ et al. (2016) Performance Analysis of a Field-Effect-Transistor Based Aptasensor. In: Satapathy CS et al. (Ed) Microelectronics, Electromagnetics and Telecommunications: Proceedings of ICMEET, Springer, New Delhi, pp767-775

120. Li J, Pud S, Petrychuk M et al. (2014) Sensitivity enhancement of Si nanowire field effect transistor biosensors using single trap phenomena. Nano Letters 14:3504-3509

121. Gao XPA, Zheng G, Lieber CM (2010) Subthreshold Regime has the Optimal Sensitivity for Nanowire FET Biosensors. Nano Letters 10:547-552

122. Vu XT, Stockmann R, Wolfrum B et al. (2010) Fabrication and application of a microfluidic-embedded silicon nanowire biosensor chip. physica status solidi (a) 207:850-857

123. Freitas PP, Cardoso FA, Martins VC et al. (2012) Spintronic platforms for biomedical applications. Lab on a Chip 12:546-557

124. Cui Y, Duan X, Hu J et al. (2000) Doping and Electrical Transport in Silicon Nanowires. The Journal of Physical Chemistry B 104:5213-5216

125. Stern E, Vacic A, Rajan NK et al. (2010) Label-free biomarker detection from whole blood. Nature Nanotechnology 5:138-142

126. Cheng S, Hotani K, Hideshima S et al. (2014) Field Effect Transistor Biosensor Using Antigen Binding Fragment for Detecting Tumor Marker in Human Serum. Materials 7:2490

127. Kim KS, Lee H-S, Yang J-A et al. (2009) The fabrication, characterization and application of aptamer-functionalized Si-nanowire FET biosensors. Nanotechnology 20:235501

128. Gao N, Zhou W, Jiang X et al. (2015) General Strategy for Biodetection in High Ionic Strength Solutions Using Transistor-Based Nanoelectronic Sensors. Nano Letters 15:2143-2148

129. Elnathan R, Kwiat M, Pevzner A et al. (2012) Biorecognition Layer Engineering: Overcoming Screening Limitations of Nanowire-Based FET Devices. Nano Letters 12:5245-5254

130. Bunimovich YL, Shin YS, Yeo W-S et al. (2006) Quantitative Real-Time Measurements of DNA Hybridization with Alkylated Nonoxidized Silicon Nanowires in Electrolyte Solution. Journal of the American Chemical Society 128:16323-16331

131. Lu N, Gao A, Zhou H et al. (2016) Progress in Silicon Nanowire-Based Field-Effect Transistor Biosensors for Label-Free Detection of DNA. Chinese Journal of Chemistry 34:308-316

132. Pandya HJ, Kim HT, Roy R et al. (2014) Towards an automated MEMS-based characterization of benign and cancerous breast tissue using bioimpedance measurements. Sensors and Actuators B: Chemical 199:259-268

133. Shoorideh K, Chui CO (2014) On the origin of enhanced sensitivity in nanoscale FET-based biosensors. Proceedings of the National Academy of Sciences 111:5111-5116

134. Zhou W, Dai X, Fu TM et al. (2014) Long term stability of nanowire nanoelectronics in physiological environments. Nano Letters 14:1614-1619

135. Qian F, Li Y, Gradecak S et al. (2008) Multi-quantum-well nanowire heterostructures for wavelength-controlled lasers. Nature Materials 7:701-706

136. Liu J, Xie C, Dai X et al. (2013) Multifunctional three-dimensional macroporous nanoelectronic networks for smart materials. Proceedings of the National Academy of Sciences 110:6694-6699

137. Li J, He G, Ueno H et al. (2016) Direct real-time detection of single proteins using silicon nanowire-based electrical circuits. Nanoscale 8:16172-16176

138. Chu CJ, Yeh CS, Liao CK et al. (2013) Improving nanowire sensing capability by electrical field alignment of surface probing molecules. Nano Letters 13:2564-2569

139. Morton KJ, Nieberg G, Bai S et al. (2008) Wafer-scale patterning of sub-40 nm diameter and high aspect ratio (>50:1) silicon pillar arrays by nanoimprint and etching. Nanotechnology 19:345301-345301

140. Cui Z (2008) Nanofabrication. Springer US

141. Ziegler JF, Ziegler MD, Biersack JP (2010) SRIM – The stopping and range of ions in matter. Nuclear Instruments and Methods in Physics Research Section B: Beam Interactions with Materials and Atoms 268:1818-1823

142. Nguyen TC, Schwartz M, Vu XT et al. (2015) Handheld readout system for field-effect transistor biosensor arrays for label-free detection of biomolecules. physica status solidi (a) 212:1313-1319

143. Jolly P, Damborsky P, Madaboosi N et al. (2016) DNA aptamer-based sandwich microfluidic assays for dual quantification and multi-glycan profiling of cancer biomarkers. Biosensors and Bioelectronics 79:313-319

144. Madaboosi N, Soares RRG, Chu V et al. (2015) A microfluidic immunoassay platform for the detection of free prostate specific antigen: a systematic and quantitative approach. Analyst 140:4423-4433

145. Masood MN (2011) Surface modification of silicon nanowire field-effect devices with Si-C and Si-N bonded monolayers. In: Dissertation, University of Twente

146. Beebe DJ, Mensing GA, Walker GM (2002) Physics and Applications of Microfluidics in Biology. Annual Review of Biomedical Engineering 4:261-286

147. Capretto L, Cheng W, Hill M et al. (2011) Micromixing Within Microfluidic Devices. In Lin B (Ed.) Microfluidics: Technologies and Applications, Springer Berlin Heidelberg: Berlin, Heidelberg, pp 27-68

148. Young ME, Carroad PA, Bell RL (1980) Estimation of diffusion coefficients of proteins. Biotechnology and Bioengineering 22:947-955

149. Stone HA, Stroock AD, Ajdari A (2004) ENGINEERING FLOWS IN SMALL DEVICES. Annual Review of Fluid Mechanics 36:381-411

150. Yang Z, Matsumoto S, Goto H et al. (2001) Ultrasonic micromixer for microfluidic systems. Sensors and Actuators A: Physical 93:266-272

151. Oddy MH, Santiago JG, Mikkelsen JC (2001) Electrokinetic Instability Micromixing. Analytical Chemistry 73:5822-5832

152. Lee C-T, Lee C-C (2012) A capillary-driven micromixer: idea and fabrication. Journal of Micromechanics and Microengineering 22:105034

153. Fan C, Lopinski GP (2010) STM and HREELS investigation of gas phase silanization on hydroxylated Si(100). Surface Science 604:996-1001

154. Jolly P, Formisano N, Tkáč J et al. (2015) Label-free impedimetric aptasensor with antifouling surface chemistry: A prostate specific antigen case study. Sensors and Actuators B: Chemical 209:306-312

155. Savory N, Abe K, Sode K et al. (2010) Selection of DNA aptamer against prostate specific antigen using a genetic algorithm and application to sensing. Biosensors and Bioelectronics 26:1386-1391

156. elisa-chemiluminescent-assay. http://www.elisa-antibody.com/ELISA-Introduction/elisa-detection-strategies/elisa-chemiluminescent-assay. Accessed December 2016

157. Hage T, Sebald W, Reinemer P et al. (1999) Crystal structure of the interleukin-4/receptor alpha chain complex reveals a mosaic binding interface. Cell 97:271-281

158. Kraich M, Klein M, Patino E et al. (2006) A modular interface of IL-4 allows for scalable affinity without affecting specificity for the IL-4 receptor. BMC biology 4:13

159. Ortiz-Conde A, García Sánchez FJ, Liou JJ et al. (2002) A review of recent MOSFET threshold voltage extraction methods. Microelectronics Reliability 42:583-596

160. Nordqvist C (2017) Prostate Cancer: Causes, Symptoms and Treatments. http://www.medicalnewstoday.com/articles/150086.php.

161. https://www.cancer.gov/types/prostate. Accessed December 2015

162. Kang BJ, Jeun M, Jang GH et al. (2015) Diagnosis of prostate cancer via nanotechnological approach. Dove Press: International Journal of Nanomedicine 10:6555-6569

163. Madu CO, Lu Y (2010) Novel diagnostic biomarkers for prostate cancer. Journal of Cancer 1:150-177

164. Makarov DV, Loeb S, Getzenberg RH et al. (2009) Biomarkers for Prostate Cancer. Annual Review of Medicine 60:139-151

165. Prostate Cancer. http://sburology.com/14-prostate-cancer.html. Accessed December 2016

166. Wu JY-S, Lin C-H, Feng M-H et al. (2016) Preparation of Silicon Nanowire Field-effect Transistor for Chemical and Biosensing Applications. Journal of Visualized Experiments e53660

167. Pui TS, Kongsuphol P, Arya SK et al. (2013) Detection of tumor necrosis factor (TNF-α) in cell culture medium with label free electrochemical impedance spectroscopy. Sensors and Actuators B: Chemical 181:494-500

168. Chen P, Chung MT, McHugh W et al. (2015) Multiplex Serum Cytokine Immunoassay Using Nanoplasmonic Biosensor Microarrays. ACS Nano 9:4173-4181

169. Baraket A, Lee M, Zine N et al. (2017) A fully integrated electrochemical biosensor platform fabrication process for cytokines detection. Biosensors and Bioelectronics 93:170-175

170. Lu N, Gao A, Dai P et al. (2015) Ultrasensitive Detection of Dual Cancer Biomarkers with Integrated CMOS-Compatible Nanowire Arrays. Analytical Chemistry 87:11203-11208

171. Tzouvadaki I, Jolly P, Lu X et al. (2016) Label-Free Ultrasensitive Memristive Aptasensor. Nano Letters 16:4472-4476

172. Ingebrandt S (2001) Characterisation of the Cell-Transistor Coupling. In: Dissertation, Johannes Gutenberg University of Mainz

173. Han Y, Offenhäusser A, Ingebrandt S (2006) Detection of DNA hybridization by a field-effect transistor with covalently attached catcher molecules. Surface and Interface Analysis 38:176-181

174. Lee J-O, So H-M, Jeon E-K et al. (2008) Aptamers as molecular recognition elements for electrical nanobiosensors. Analytical and Bioanalytical Chemistry 390:1023-1032

175. Das BK, Tlili C, Badhulika S (2011) Single-walled carbon nanotubes chemiresistor aptasensors for small molecules: picomolar level detection of adenosine triphosphate. Chemical Communications 47:3793-3795

176. Dickson IR, Perkins DJ (1971) Studies on the interactions between purified bovine caseins and alkaline-earth-metal ions. Biochemical Journal 124:235-240

177. Peracaula R, Tabarés G, Royle L et al. (2003) Altered glycosylation pattern allows the distinction between prostate-specific antigen (PSA) from normal and tumor origins. Glycobiology 13:457-470

178. Zhang WM, Leinonen J, Kalkkinen N et al. (1995) Purification and characterization of different molecular forms of prostate-specific antigen in human seminal fluid. Clinical Chemistry 41:1567-1573

179. Schwartz M, Nguyen TC, Vu XT et al. (2016) DNA detection with top–down fabricated silicon nanowire transistor arrays in linear operation regime. physica status solidi (a) 213:1510-1519

180. Luchansky MS, Bailey RC (2011) Rapid, Multiparameter Profiling of Cellular Secretion Using Silicon Photonic Microring Resonator Arrays. Journal of the American Chemical Society 133:20500-20506

181. Hall SA, Stucke D, Morrone B et al. (2015) Simultaneous detection and quantification of six equine cytokines in plasma using a fluorescent microsphere immunoassay (FMIA). MethodsX 2:241-248

182. Usuba R, Yokokawa M, Ackermann TN (2016) Photonic Lab-on-a-Chip for Rapid Cytokine Detection. ACS Sensors 1:979-986

183. Lau UY, Saxer SS, Lee J et al. (2016) Direct Write Protein Patterns for Multiplexed Cytokine Detection from Live Cells Using Electron Beam Lithography. ACS Nano 10:723-729

184. Chen H, Choo TK, Huang J et al. (2016) Label-free electronic detection of interleukin-6 using horizontally aligned carbon nanotubes. Materials & Design 90:852-857

185. Nam H, Oh B-R, Chen P et al. (2015) Multiple MoS_2 Transistors for Sensing Molecule Interaction Kinetics. Scientific Reports 5:10546

186. Mao Y, Shin K-S, Wang X et al. (2016) Semiconductor Electronic Label-Free Assay for Predictive Toxicology. Scientific Reports 6:24982

187. Wu J-Y, Tseng C-L, Wang Y-K et al. (2013) Detecting Interleukin-1β Genes Using a N_2O Plasma Modified Silicon Nanowire Biosensor. Journal of Experimental & Clinical Medicine 5:12-16

188. Zamorano J, Rivas MD, Pérez-G M (2003) Interleukin-4: A multifunctional cytokine. Immunologia 22:215-224

189. Zhang J-M, An J (2007) Cytokines, Inflammation and Pain. International anesthesiology clinics 45:27-37

190. alpha interleukin-4 receptor. http://www.nlbiochemex.com/immunology/proteins/rat/p92031ra01.html. Accessed September 2016

191. Interleukin-4. http://www.phosphosite.org/simpleSearchSubmitAction.action?queryId=-1&from=0&searchStr=interleukin%204. Accessed September 2016

192. Interleukin-2. http://www.phosphosite.org/simpleSearchSubmitAction.action?queryId=-1&from=0&searchStr=interleukin-2. Accessed September 2016

List of figures

residual layer of the resist using RIE process; and (B) Temperature and pressure profile of the different steps (i), (ii) and (iii) in the T-NIL process.

Figure 2.7 Schematic representation for anisotropic etching of Si with a SiO_2 hard mask: (A) A patterned SiO_2/Si wafer before TMAH etching; and (B) A SiO_2/Si wafer after TMAH etching.

Figure 3.1 Layout of the Si NW FETs chips on a 4" mask in the Clewin program with a single Si NW FET chip (with dimensions 7 mm × 10 mm) shown in the inset.

Figure 3.2 Schematic of the NIL mould fabrication on a 6" SiO_2/Si wafer: (i) PMMA resist coated on a SiO_2/Si wafer; (ii) Exposure of the resist coated wafer with electron-beam; (iii) Development of the resist that results in trenches in the resist; and (iv) RIE of the exposed SiO_2 layer and removal of the leftover resist to have the final SiO_2/Si mould.

Figure 3.3 (A) Layout of the Si NW FETs structures on the SiO_2/Si mould; SEM images showing (B) Width of a NW structure; and (C) Depth profile in the fabricated SiO_2/Si mould.

Figure 3.4 Plots showing boron (A) Implantation energy obtained from the SRIM simulation software; and (B) Dose obtained from the TRIM simulation software. Based on these simulations the energy and dose were fixed for the service implantation.

Figure 3.5 Schematics of the process flow for the fabrication of Si NW FETs (clockwise): (i) SOI wafer after the thermal oxidation process to grow a SiO_2 layer on top; (ii) SOI wafer coated with patterned thermoresist after the NIL process; (iii) Thermoresist coated SOI after the RIE of the residual layer; (iv) Structured SiO_2 layer (mask) over the SOI wafer after the dry etching process for SiO_2 and for removal of the leftover thermoresist; (v) Wet anisotropic etching of the Si layer; (vi) Si NW and contact line regions structured in the Si layer after boron implantation of the contact lines using one photolithography step for the NW passivation; (vii) Evaporation of Al/Ti/Au over the implanted Si contact lines using a second photolithography process and a lift-off process; and (viii) Final 4" SOI wafer with the 32 Si NW FETs layout on 7 mm × 10 mm chips (a photograph of a single chip shown in the inset).

Figure 3.6 Microscopic characterizations of the Si NW FETs: (A) A zoomed out optical microscopy image of the sensor chip after the imprint process; (B) A microscopy image after the photolithography step for passivation of the NWs; (C) SEM image of one Si NW FET set after the TMAH etching process with (D) Zoomed in view of one NW; and (E) A detailed 3D view of one Si NW FET set characterized using AFM with a height profile of four individual NWs shown on the right side.

Figure 3.7 SEM characterization results showing the intrinsic problems in Si NW FETs fabrication, when combining the NIL and RIE processes: (A, B, C) SEM images of the NW sets with different NW widths after the RIE process.

Figure 3.8 Microscopic characterization results showing examples of intrinsic problems in the Si NW FETs fabrication, when combining the NIL and UV lithography processes: (A, B) SEM images at different positions on the wafer after the TMAH etching step; and (C, D) Optical microscopy images of one NW set after the UV lithography step for ion implantation with perfectly aligned (C) and misaligned (D) passivation mask.

Figure 3.9 Left: A snapshot of the PCB designed using the EAGLE software for the Si NW FET chip for (A) a 4-channel setup with which only 4 FETs can be measured; (B) a 32 channel setup with which 32 FETs can be measured simultaneously. Right: A picture of the Si NW FET chip wire bonded and encapsulated on a (A) PCB for the 4-channel setup; (B) PCB for the 32-channel setup.

Figure 3.10 Schematic of the process flow of SU-8 mould fabrication for the straight microfluidic channel design (counter clockwise): (i) Al (200 nm) on glass wafer; (ii) Resist coating on Al/glass wafer; (iii) Direct laser writing with the desired microfluidic layout; (iv) Trenches in the resist layer after the development; (v) Etching of the Al layer resulting in trenches in the Al layer and this patterned Al/glass wafer acted as a mask for the patterning of SU-8 resist on the Si wafer; (vi) A Si wafer spin coated with SU-8 (20 μm thick) resist aligned below the structured side of the Al mask and then UV exposure; (vii) After the development process, SU-8 protrusions on Si wafer at the channel region and this patterned SU-8/Si wafer acted as a mould for curing the PDMS; and (viii) Curing of PDMS using the SU-8 mould and then peeling off to have the straight microfluidic channels in the PDMS layer.

Figure 3.11 Layout of the Si NW FET chip with a mixer channel, which includes two inlets and one outlet. The baffles (black bars shown on the right side top) are created within the channel walls in order to mix the fluids through the two inlets.

Figure 3.12 Schematic for the gas phase silanization process of the Si NW FET chips: (A) Piranha cleaning of the Si NW FETs to have a high density of -OH groups at the Si NW surfaces; and (B) APTES silanization in gas phase to uniformly assemble APTES molecules on the Si NW surfaces.

Figure 3.13 Schematic of different steps in the surface functionalization of Si NW FET chips for electronic and optical detection of PSA (clockwise): (A) Piranha cleaning for activation of the Si NWs to have high density of -OH groups; (B) Silanization of the Si NWs with GPTES in gas phase; (C) Amine-terminated, PSA-specific aptamer immobilization on the Si NWs; (D) Blocking using ethanolamine for the leftover GPTES sites on the Si NWs; (E) PSA binding to the aptamer-functionalized Si NW surfaces; and (F) Anti-PSA-HRP antibody binding to the PSA-aptamer complex on the Si NW surfaces. As indicated by the central inset, step E is typically the event for the electronic detection of PSA using Si NW FETs.

Figure 3.14 Schematic of the surface functionalization of Si NW FETs for electronic detection of cytokine IL-4: (A) High density of -OH groups after the activation of Si NWs using piranha cleaning; (B) α IL-4 adsorption over the Si NW surfaces; (C) IL-2 immobilization on the α IL-4 functionalized Si NW surfaces to check non-specific binding of IL-2; and (D) IL-4 and α IL-4 complex formation after IL-4 immobilization over α IL-4 functionalized Si NW surfaces (3D structure of proteins adapted from Pdb: 1IAR, 2B8U) [157-158].

Figure 4.1 (A) Schematic of the Si NW ISFET chip with liquid gate configuration shown in the inset; and (B) Equivalent electronic circuit for the Si NW FET operation in liquid gate configuration.

Figure 4.2 Electrical characterization of a Si NW ISFET: (A) Transfer characteristic where the drain-source current (I_{ds}) was measured as a function of the gate-source voltage (V_{gs}) with the drain-source voltage varying from 0 to -1 V in steps of 0.25 V; (B) Output characteristics where the drain-source current was measured as a function of the drain-source voltage (V_{ds}) with gate-source voltage varying from 0 to -1 V in steps of 0.25 V; (C) Transconductance as a function of gate-source voltage for a drain-source voltage of -1 V; and (D) Current between the two source electrode contacts of the chip showing that the contact between the metal contacts and the doped Si contact lines is perfectly ohmic.

Figure 4.3 Extracted threshold voltage of 54 Si NW ISFETs chosen from three different chips on a wafer before (black) and after the GPTES silanization process (red) shown on the left side; and the corresponding average threshold voltage before and after the silanization process for three different chips shown in the table on the right side. The statistical analysis was done using a paired t-test (*** for $P < 0.001$, ** for $P < 0.01$ and * for $P < 0.1$).

Figure 4.4 (A) Transfer characteristic curves of a Si NW ISFET with increase in pH (of 10 mM PB) from 5 to 9 at V_{ds} = -100 mV; (B) Change in threshold voltage plotted as a function of pH of the buffer solution with an average change of ΔV_{th} = 43 ± 3 mV/pH; (C) Transfer characteristic curves of a Si NW ISFET with increase and decrease in pH of the buffer from 5 to 9 and 9 to 5 at V_{ds} = -100 mV; and (D) Change in threshold voltage of a Si NW ISFET (from a different chip) plotted as a function of pH of the buffer solution with an average change of ΔV_{th} = 48 ± 19 mV/pH.

Figure 4.5 (A) Picture of a portable Si NW ISFET measurement system with a sensor chip and an external reference electrode immersed in the buffer solution over the Si NW; (B, D) Real-time pH measurements with two different Si NW ISFET chips, where the drain-source current was measured as a function of time and the pH of the buffer solution was changed from 4 to 10 in multiple cycles; and (C, E) Average change in the drain-source current as a function of the buffer solution pH for two different Si NW ISFET chips.

Figure 5.1 (A) A picture of an encapsulated Si μ ISFETs chip; and (B) Optical microscopy image of one μ ISFET consisting of a common source electrode, one drain electrode and a gate area.

Figure 5.2 Schematics of the surface functionalization of Si NW ISFETs for PSA detection: (A) A 3D AFM image of one set of Si NW ISFETs with the height profile shown on the left top side; and (B) The Si NW surface was silanized with GPTES and immobilized with PSA-specific aptamers. The leftover GPTES sites were then blocked with ethanolamine. The binding of PSA onto the aptamer-functionalized Si NW surfaces resulted in a change in the conformation of the aptamers and thus the electronic detection was carried out.

Figure 5.3 (A) Si μ ISFET transfer characteristic curves after the different immobilization steps (GPTES, aptamer, EA, 30 nM PSA); (B) Si NW ISFET transfer characteristic curves after the different immobilization steps; (C) Change in the V_{th} (with respect to GPTES) after each immobilization step for Si μ ISFETs (n = 2) and Si NW ISFETs (n = 18) shown as a scatter plot. The data was analysed using a paired t-test (ns for not significant, *** for P < 0.001, ** for P < 0.01 and * for P < 0.1); and (D, E) Variation in the V_{th} for different sets (composed of 4 Si NWs each) of Si NW ISFETs on a single chip after the different immobilization steps and the corresponding average V_{th}, both shown as a scatter plot. (note: n indicates the number of ISFETs)

Figure 5.4 (A) Exemplary AFM image of one Si NW before and after the aptamer immobilization and the corresponding line plot for Si NW height analysis (right side); (B) AFM image of one Si NW after the aptamer and 30 nM PSA immobilization and the corresponding line plot for height analysis; and (C) Microspotting nozzle image with a DNA aptamer droplet and the Si NW ISFET chip image with microspotted aptamer droplets on the Si NW sets (right side).

Figure 5.5 (A, B) Variation in V_{th} for different sets (n = 9) of Si NW ISFETs on two chips after GPTES silanization and after the aptamer microspotting process shown as a scatter plot. Average V_{th} of the Si NW ISFETs sets with GPTES and microspotted aptamer shown in the scatter plot (** for p < 0.01 and * for p < 0.1); and (C, D) Variation in the V_{th} for different sets (n = 10) of Si NW ISFETs on two chips after GPTES and aptamer drop casting (without microspotting) process shown as a scatter plot. Average V_{th} of the Si NW ISFETs sets with GPTES and drop casted aptamer shown in the scatter plot (*** for p < 0.001 and ** for p < 0.01).

Figure 5.6 (A, B) Variation in the V_{th} of different Si NW ISFETs on an exemplary chip at different immobilization steps (i.e., GPTES, aptamer (n = 1 to 20) and PB (without aptamer) (n = 21 to 32), EA, 30 nM PSA) and the corresponding average, both shown in the scatter plot (ns for not significant and *** for P < 0.001); (C) A control Si NW ISFET transfer characteristic curves at the different immobilization steps; (D) The relative V_{th} change with respect to ethanolamine plotted as a function of PSA concentrations (a new stock solution) for two Si NW

ISFETs with aptamer and without aptamer; and (E, F) Transfer characteristic curves at different PSA concentrations for a Si NW ISFET with aptamer and without aptamer, respectively.

Figure 5.7 (A) Si NW ISFET transfer characteristic curves at different immobilization steps (GPTES, aptamer, EA, PB without PSA); and (B) The V_{th} change of two Si NW ISFETs at different immobilization steps shown in the scatter plot (ns for not significant, ** for $P < 0.01$ and * for $P < 0.1$).

Figure 5.8 (A) A Si NW ISFET sensor chip with the straight channel (100 μm wide, 20 μm high and 4 mm long) PDMS microfluidic layer with metallic inlet, outlet and tubing; and (B) Microscopic image of the Si NW chip with the PDMS microfluidic channel.

Figure 5.9 (A, B) Schematics for the functionalization of the Si NW surfaces in a chemiluminescence assay with PSA-specific and non-specific aptamers, respectively; (C) Optical microscopy image of the fluidic channels filled with luminol for different concentrations of PSA with PSA-specific aptamers as indicated in the pictures; (D) Optical microscopy image of the fluidic channel filled with luminol for buffer without PSA and with non-specific aptamers; and (E) Chemiluminescence signal intensity (arbitrary units) for the different concentrations of PSA with the non-specific aptamer (control) and PSA-specific aptamer sequence shown in the scatter plot (ns for not significant, *** for $P < 0.001$, ** for $P < 0.01$ and * for $P < 0.1$).

Figure 5.10 (A) Schematics for the functionalization of the Si NW surface in a fluorescence assay with the PSA-specific aptamers and an anti-PSA-FITC antibody; (B) Optical microscopy image of the microfluidic channel aligned to the Si NW ISFETs chip with 0 nM PSA and 30 nM PSA in the presence of the PSA-specific aptamers detected using a FITC labelled, anti-PSA, secondary antibody; and (B) Fluorescence signal (FITC) intensity with 0 nM PSA (control) and 30 nM PSA concentration shown in the scatter plot.

Figure 6.1 Schematics for the surface functionalization of the Si NW surface after piranha cleaning: (A) Cytokine IL-4 assay, where IL-4 antibody was allowed to react with the α IL-4 receptor functionalized Si NW surface and thereby a complex between IL-4 and α IL-4 over the Si NW surface was formed; (B) Control experiment where non-conjugate antibody, IL-2 was allowed to react with the α IL-4 receptor functionalized Si NW surface, that resulted in non-specific binding of IL-2 over the Si NW surface; and (C) Another control experiment, where IL-4 was allowed to react with the Si NW surface without α IL-4 receptor and thus IL-4 was bound non-specifically over the Si NW surface.

Figure 6.2 (A) Si NW ISFET transfer characteristic curves at the different assay steps for the cytokine IL-4 assay, that included piranha cleaning (before), α IL-4 (1 μg/ml) immobilization and IL-4 (250 μg/ml) binding; and (B) Change in the V_{th} of Si NW ISFETs ($n = 4$) with respect to before at different immobilization steps for the cytokine IL-4 assay shown in the scatter plot (*** for $P < 0.001$ and * for $P < 0.1$).

Figure 6.3 AFM image of an area of a Si NW set before and after the α IL-4 immobilization with the corresponding line plot for height analysis shown on the right side.

Figure 6.4 Si NW ISFET transfer characteristic curves at different assay steps for (A) Control of cytokine IL-4 assay without IL-4 that included piranha cleaning (before), α IL-4 (1 μg/ml) immobilization and reaction with IL-2 (100 μg/ml); (C) Control of the cytokine IL-4 assay without α IL-4 that includes piranha cleaning (before), PB (without α IL-4) and IL-4 (250 μg/ml) immobilization. Change in the V_{th} of the Si NW ISFETs at different assay steps shown in the scatter plot for (B) Control of cytokine IL-4 assay without IL-4 ($n = 4$); and (D) Control of the cytokine IL-4 assay without α IL-4 ($n = 2$) (ns for not significant and ** for $P < 0.01$).

List of Tables

Publications

1. D. Rani, V. Pachauri, N. M. Srinivasan, P. Estrela, V. Chu, J. P. Conde, S. Ingebrandt; Silicon nanowire ion-sensitive field-effect transistor-based biosensor towards electronic and optical detection of prostate specific antigen; Submitted
2. D. Rani, V. Pachauri, Y. Singh, S. Ingebrandt; Label free detection of Cytokine IL-4 using Si NW ISFETs based biosensors; Submitted
3. D. Rani, V. Pachauri, S. Ingebrandt; Silicon nanowire field-effect biosensors; book chapter submitted (31.08.2017) in Springer Nature.
4. D. Rani, V. Pachauri, A. Mueller, X. T. Vu, T. C. Nguyen, S. Ingebrandt; On the use of scalable NanoISFETs of silicon with highly reproducible sensor performance for assaybased applications; ACS Omega 2016, doi:10.1021/acsomega.6b00014.
5. N. Bhalla, Z. Yang, S. Sivaraya, D. Rani, V. Pachauri, S. Ingebrandt, A. Gorbach, P. Estrela; Silicon nitride thickness and composition dependent localized surface plasmon and exciton coupling on pH sensitive nanofilms; submitted in Material Letters.

Conferences/summer schools/workshops

6. D. Rani, V. Pachauri, X. T. Vu, S. Ingebrandt; Label-free detection of biomolecules using highly reproducible silicon nanowire transistors; EMN meeting on Nanowires, 3rd-7th May 2017, Dubrovnik, Croatia (oral presentation).
7. D. Rani, V. Pachauri, A. Mueller, X. T. Vu, S. Ingebrandt; Label-free detection of PSA using highly reproducible silicon nanowire arrays; Engineering of Functional Interfaces (EnFI), 3rd-5th July 2016, Berlin, Germany (oral and poster presentation).
8. D. Rani, V. Pachauri, S. Ingebrandt; Label-free detection of PSA using highly reproducible Si nanoISFETs; EMN meeting on Nanowires, 16th-19th May 2016, Amsterdam, Netherlands (oral presentation).
9. D. Rani, V. Pachauri, S. Ingebrandt; silicon nanowire field-effect transistors for early screening of prostate cancer; PROSENSE spring school on “Label-free techniques for electronic sensing of biomolecules” 27th-30th April 2016, Zweibruecken, Germany (oral and poster presentation).
10. D. Rani, V. Pachauri, S. Ingebrandt; silicon nanowire field-effect transistors for early screening of prostate cancer; PROSENSE winter school on “New nano-bio-sensing tools for theragnostics” 1st-5th February 2016, Lausanne, Switzerland (oral and poster presentation).
11. D. Rani, V. Pachauri, S. Ingebrandt; silicon nanowire field-effect transistors for early screening of prostate cancer; PROSENSE workshop on “Integration of biosensing in multiplex lab-on-a-chip devices” 14th-19th July 2015, Lisbon, Portugal (oral and poster presentation).
12. D. Rani, V. Pachauri, X. T. Vu, A. Mueller, S. Ingebrandt; Label free detection of prostate-specific antigens using Si-NW FETs; Engineering of Functional Interfaces (EnFI), 6th-7th July 2015, Hannover, Germany (oral and poster presentation).
13. D. Rani, V. Pachauri, S. Ingebrandt; silicon nanowire field-effect transistors for early screening of prostate cancer; PROSENSE workshop on “Biosensor construction” 13th-17th January 2015, Cardiff, United Kingdom (oral and poster presentation).
14. D. Rani, V. Pachauri, A. Mueller, X.L. Lu, M. Schwartz, L.E. Delle, X.T. Vu, S. Ingebrandt; Opto-electronic biosensors based on silicon nanowire field-effect transistors

for early screening of prostate cancer; 22nd Meeting of the EAU Section of Urological Research (ESUR), 9th-11th October 2014, Glasgow, United Kingdom (poster presentation).

15. D. Rani, V. Pachauri, S. Ingebrandt; silicon nanowire field-effect transistors for early screening of prostate cancer; PROSENSE workshop on "Clinical perspectives and commercial forces on biosensor devices" 15th-19th September 2014, Bath, United Kingdom (oral and poster presentation).
16. D. Rani, V. Pachauri, A. Mueller, X.T. Vu, S. Ingebrandt; Bi-functional Si-NW FETs as opto-electronic biosensors for prostate cancer pre-screening; Engineering of Functional Interfaces (EnFI), 14th-15th July 2014, Jülich, Germany (oral and poster presentation).
17. D. Rani, V. Pachauri, S. Ingebrandt; silicon nanowire field-effect transistors for early screening of prostate cancer; PROSENSE workshop on "Application of lectins in various format of analysis for glycoprofiling" 23rd-24th January 2014, Bratislava, Slovakia (oral and poster presentation).
18. D. Rani, X.T. Vu, V. Pachauri, S. Ingebrandt; Field-effect transistors as label-free biosensors for prostate cancer biomarker detection; International Conference on Advanced Manufacturing for Multifunctional Miniaturised Devices (M6), 15th-16th July 2013, Zweibrücken, Germany (oral and poster presentation).
19. D. Rani, X.T. Vu, V. Pachauri, S. Ingebrandt; Field-effect transistors as label-free biosensors for prostate cancer biomarker detection; Engineering of Functional Interfaces (EnFI), 8th-9th July 2013, Hasselt, Belgium (oral and poster presentation).
20. D. Rani, V. Pachauri, S. Ingebrandt; silicon nanowire field-effect transistors for early screening of prostate cancer; PROSENSE workshop on "The production and application of antibodies and their use in biosensors and arrays." 1st-4th July 2013, Dublin, Ireland (oral and poster presentation).

Acknowledgements

I would like to acknowledge many people who made this thesis possible both professionally and personally. First of all, I am grateful to Prof. Sven Ingebrandt for giving me an opportunity to work in the Biomedical signalling group of University of Applied Sciences Kaiserslautern, campus Zweibruecken, Germany. I am thankful to him for his guidance, scientific discussions and corrections of the thesis. I am also grateful to Prof. Martin Eickhoff for agreeing to supervise my work in Justus Liebig University in Giessen.

Among the many people who helped me to accomplish this thesis, I am especially thankful to Dr. Vivek Pachauri for the scientific discussions. I am also thankful to him for his guidance during writing of the publications, thesis and in preparation of the conference presentations. It was also very helpful to work with Dr. Xuan Thang Vu, who gave me an introduction to the clean room fabrication and electronic characterization techniques. In particular, I am thankful to Achim Müller for discussions related to the clean room work. I am grateful to other members of the biomedical signalling group - Dr. Jessica Ka-Yan Law, Dr. Maryam Weil, Dr. Anette Britz, Xiaoling Lu, Ruben Lanche, Lotta Emilia Delle, Felix Hempel, Walid Munief, Thanh Chien Nguyen, Miriam Schwartz, Dr. Anna Susloparova, Dr. Dieter Koppenhöfer, Nina Stock, Luis Centeno, Tina Welsch, Julia Schmitz and Sabrina Dunger for their collaboration and the good time spent together.

Within the technical support at University of Applied Sciences Kaiserslautern, I am thankful to Rainer Lilischkis, Detlev Cassel and Erik Engelmann for their help with various equipments in the clean room and outside of it.

Being part of the Marie Curie International training network - Parallel Sensing Of Prostate Cancer Biomarkers (PROSENSE) project (grant no. 317420, 2012-2016), gave me an opportunity to interact with researchers working in different fields. I am very thankful to Dr. Pedro Estrela and all the members of the PROSENSE team for the fruitful discussions and the jolly time spent together.

On a personal side, I am thankful to Abhishek Kumar for his great support throughout my PhD time. I am also grateful to Stefanie Wiedemann, Greetje Minke, Susann Streller for the great time spent together in Germany.

In the end I am grateful to my beloved family - brother, uncles, cousins, parents and grandparents for their constant support in all situations.

DECLARATION

I declare that I have completed this dissertation without the unauthorized help of a second party and only with the assistance acknowledged therein. I have appropriately acknowledged and referenced all text passages that are derived literally from or are based on the content of published or unpublished work of others, and all information that relates to verbal communications. I have abided by the principles of good scientific conduct laid down in the charter of the Justus Liebig University of Giessen in carrying out the investigations described in the dissertation.

_____ _____

Place, Date Signature